Electronic and Optical Properties of Quantum Dots: Metal-Insulator Transitions and Ultrafast Spectroscopy

A THESIS
SUBMITTED TO THE FACULTY OF THE GRADUATE SCHOOL
OF THE UNIVERSITY OF MINNESOTA
BY

Zachary Loren Robinson

IN PARTIAL FULFILLMENT OF THE REQUIREMENTS
FOR THE DEGREE OF
Doctor of Philosophy

Dr. Uwe Kortshagen, Advisor

May, 2020

Acknowledgements

First and foremost I would like to thank my thesis advisor Uwe Kortshagen for his advice and encouragement throughout my time in graduate school. I would also like to thank my Los Alamos advisor Victor Klimov for welcoming me into his lab and for the career opportunities that has given me. Lastly my 'third' advisor Boris Shklovskii was vitally important for all of my early work in graduate school, without him none of this would have been possible. I am extremely fortunate to have been supervised by three world leaders in their respective fields.

I would never have made it to graduate school if it were not for the assistance of classmates and teachers at my undergraduate institution, Colorado State University. My academic and research advisors there, Martin Gelfand and Stuart Field, played a huge role in my early development as a physicist. I would not have survived the undergraduate physics curriculum if not for continuous help from classmates Trey Butkovich, Dan Zavitz, Andrea Shacklock, Ian Rajala, Colton Fruhling, Ryan Whitcolm, Christian Meyer, Ian Hamilton, Karen Ford, Amanda Townsend, Matt Smith, and more.

At the University of Minnesota I would like to thank my physics classmates Nick Mast, Harison Weismann, Mike Crumrine, Mike Sammon, Scotty Dossa, Yilikal Ayino, David Harrison, James Delles, Ezra Day-Roberts, Tim Peterson and Xuzhe Ying for the help and encouragement with classes and research. Professors Eray Aydil, Jorge Vinals, Andrey Chubukov, Jim Kakalios, Vlad Pribiag, Loraine Francis, K. Andre Mkhoyan, Rafael Fernandes and Russell Holmes. From my research group first I would like to thank Ben Greenberg individually, whom I worked under for 2 years and learned a lot from. Others include Samanatha Ehrenberg Hill, Katharine Hunter, Katelyn Schramke, Kelsey Mork, Chad Beaudette, Bryan Voigt, Toshi Ono, Zhaohan Li and Ali Eslamisaray.

Dedication

To the memory of Jihua Yang and Sergey Guts, rest in peace.

Contents

List of Tables

List of Figures

Chapter 1

Introduction

Any given solid-state material may be classified based on its electronic properties as an insulator, semiconductor or metal [1,2]. In a metal the Fermi level E_F lies within a band of high density electronic states, leading to delocalized electrons and a correspondingly large conductivity. In insulators and semiconductors E_F lies inside an energy gap, E_g, which leads to a small or negligible current at zero temperature. In an insulator this gap is large ($> \sim 4$ eV) while in a semiconductor E_g is between 0 eV and ~ 4 eV. Electrons may cross this bandgap by being excited thermally, optically (by absorbing photons of energy $E > E_g$), with an external electric field, and so on. To better control the conductivity of a semiconductor, electron or hole doping can be used to increase the carrier concentration, or the semiconductor may be gated with an external electric field [3].

The attempt to understand the electronic behavior of materials dates back centuries, but the work in the 19th century on electromagnetism together with the development of quantum mechanics in the 1920s led to a serious breakthrough in the 1930s which continues to the present day. The semiconductor transistor was developed in 1948 [4], revolutionizing the world, and enhanced crystal growth and doping methods led to very pure semiconductors enabling large-scale manufacturing and a continuous decrease in device size. The search for new materials and heterostructures, smaller/faster devices and cheap manufacturing has fueled a continuous development in the semiconductor industry.

1.1 Foundations

In a bulk semiconductor E_g is a fixed value but as the size of a semiconductor is decreased below ~20 nm the bandgap increases with decreasing particle size. This effect, first discovered nearly 40 years ago [5] in doped glasses, drastically increases the utility of semiconductors by making an individual materials optical properties tunable to a demanded application. This 'quantum confinement' or 'quantum size effect' may exist along 1 (2D materials or nanoplatelets [6, 7]), 2 (nanowires or nanorods [8, 9]) or 3 (nanocrystals or quantum dots [10]) dimensions of the given material. The most intensely studied of these, and the one to be focused on in this thesis, is that of a uniformally confined spherical nanocrystal (NC), or quantum dot (QD).[1] These structures consist of 100-100,000 atoms, and behave in-between that of a molecule and bulk semiconductor. At smaller sizes the crystal structure breaks down, and at larger sizes the energy spacing between levels becomes smaller than kT, rendering the material ' bulk-like'.

The arise of quantum confinement can be simply understood by considering the time-independent Shrödinger equation,

$$-\frac{\hbar^2}{2m}\nabla^2\psi(r,\theta,\phi) + V(r,\theta,\phi)\psi(r,\theta,\phi) = E\psi(r,\theta,\phi), \tag{1.1}$$

in an infinite spherical well of radius R with potential

$$V(r) = \begin{cases} 0 & r < R \\ \infty & r > R \end{cases}.$$

This has well known solutions in expansions of spherical harmonics and Bessel functions, and leads to a size dependent correction to the bandgap [11],

$$E_g = E_{g0} + \frac{\hbar^2\pi^2}{2\mu_{eh}R^2}. \tag{1.2}$$

Here E_{g0} is the bulk bandgap, μ_{eh} is the effective mass of the electron-hole pair, or exciton (Coulombically bound hydrogen-esque state formed through interaction between

---

[1] Nominally used interchangeably, QDs are a subset of NCs which have strong confinement in all 3 spatial dimensions leading to quantization of electronic states. In this thesis 'QD' will be used for general purposes and with regards to optical phenomena while 'NC' reserved for charge transport studies.

electron and hole in a material [12]), and R the radius of the quantum dot. The $1/R^2$ dependence on E_G is a signature of quantum confinement wherein the electrons *feel* the surface barrier and correspondingly adjust their energy spectra. Hence, a QD of radius 5 nm will have a different bandgap than one of the same material but with a radius of 2.5 or 10 nm as shown in figure 1.1B.
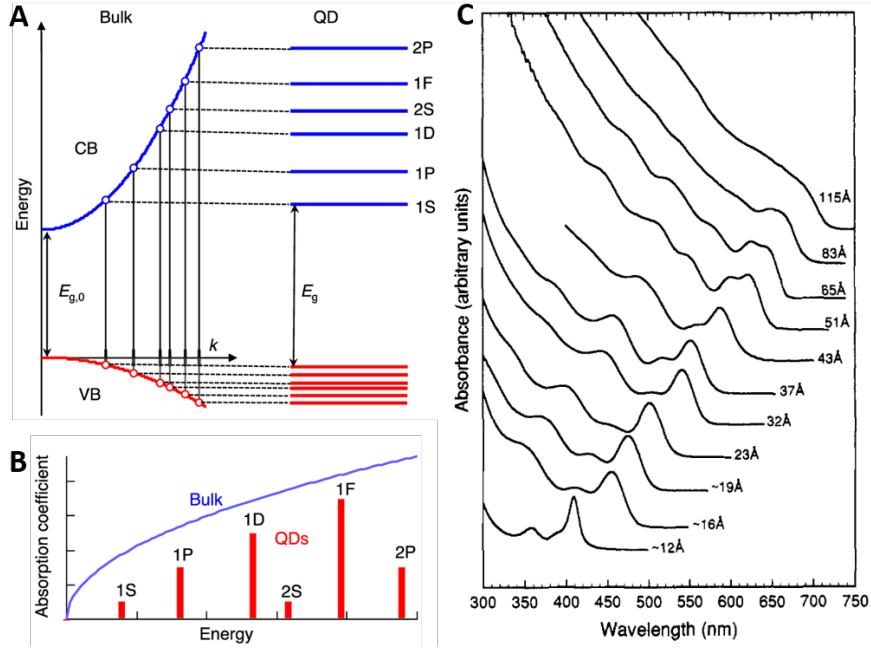
Figure 1.1: A) Schematic showing conduction/valence band in direct gap semiconductor with energy gap $E_{g,0}$. As the size of the QD is decreased below the Bohr radius of electrons/holes, the continuous energy levels split into discrete, atomic-like states. B) Absorption in a bulk semiconductor (blue) and QD (red), again showing the transition to discrete energy levels. (A) and (B) reused with permission from ref [13]. C) Absorption spectra of CdSe QDs (Bohr exciton radius is 6 nm) of varying sizes. The blue-shift of the 1S absorption feature is easily visible, as are higher order absorption peaks. Reused with permission from ref [14].

Additionally, in the strong confinement the continuum of electronic and hole states available in a bulk semiconductor transitions into discrete, atomic-like energy levels (figure 1.1A). This leads to easily discernible features in the absorption spectrum [15], akin to that of an atom or molecule, shown schematically in figure 1.1B and in experiments on CdSe QDs of different sizes [14] (figure 1.1C). For spherical QDs the states

are hydrogen-like and characterized by the quantum numbers $n = \{1,2,3,..\}$ and $L = \{s,p,d,..\}$, with the 2 lowest energy levels being 1S and 1P.

While assuming an electron in a QD behaves as if in an infinite spherical well is a rough approximation, it turns out that by using the effective mass approximation (EMA) the assumption is justified [16]. Through Bloch's theorem [17] the electronic wavefunction on a periodic lattice can be expressed via that of a plane wave multiplied by some function with the same periodicity as the underlying crystal lattice. In the effective mass approximation we limit ourselves only to band extrema (where the interesting electron/hole states lie) and expand the E($\mathbf{k}$) phase space into quadratic terms only, allowing us to describe electrons, holes and excitons as free carriers with an effective mass μ_x, where x would denote electron, hole or exciton. Hence the complicated physics of the atoms in the crystal lattice may be ignored and the electrons/holes are treated as free particles but with an altered mass. See chapter 3 for detailed use of the EMA approximation in the electronic states of CdSe/HgS/CdS QDs.

The above simple model does not take into account the Coulomb interaction; doing so introduces a 1/R term into equation 1.2. The effect of the Coulomb interaction on the optical properties of QDs depends on the type of confinement in the system. The size of the electron or hole is defined by the Bohr radius to be

$$a_B = \epsilon \frac{m}{m^*} \frac{\hbar}{mc\alpha}, \tag{1.3}$$

where ϵ is the dielectric constant of the material, m is the electron rest mass, m* is the mass of the atom, c is the speed of light and α is the fine structure constant. The latter term is the Bohr radius of the hydrogen atom, which here is written out explicitly. There are different Bohr radii for the electron (a$_e$), hole (a$_h$), and exciton (a$_e$x), each of which can be calculated from equation 1.3 by using their respective mass (for the exciton we use the reduced mass μ as mentioned above). The size of the QD with respect to the Bohr radii determine the degree of confinement present in the system.

If $R <$ a$_e$, a$_h$, a$_{ex}$ then the system is in the strong confinement regime [11]. In this situation the electrons/holes are strongly confined inside the QD. Because the Coulomb interaction scales as 1/R and the quantum confinement as 1/R^2 the Coulomb interaction is negligible in this case and the electrons and holes may be treated independently. In this regime the effective mass approximation is valid. The weak confinement regime

is when a_e, $a_h < R < a_{ex}$, and in this situation the Coulomb interaction cannot be neglected so readily. Lastly, intermediate confinement regime is when $a_{e,h} < R < a_{h,e}$, a_{ex}, in which case only one of the electron/hole is strongly confined. This regime occurs often in heterostructures when the bandgap profile separates the electron and hole [18].

Advances in synthetic techniques have rendered remarkable QDs of a variety of materials. Growth of QDs can be controlled to within ± 1 lattice constant yielding size dispersions of $< 5\%$ and ensemble emission spectra as narrow as 40 meV [19], close to the thermal energy of 25 meV. To date QDs of a huge variety of semiconductors have been made, with emission wavelengths spanning the UV to IR spectrum [13].

Of great importance is the synthesis of core/shell QDs, where the 'core' QD is over-coated by a different semiconductor, the 'shell' [20]. The shell layer serves to protect the core QD leading to great enhancement in the emission quantum yield (QY, the probability of getting a photon out per photon absorbed) to nearly 100% [21]. The shell may have a higher(lower) conduction(valence) band than the core, allowing for the electron and hole to be independently controlled spatially.
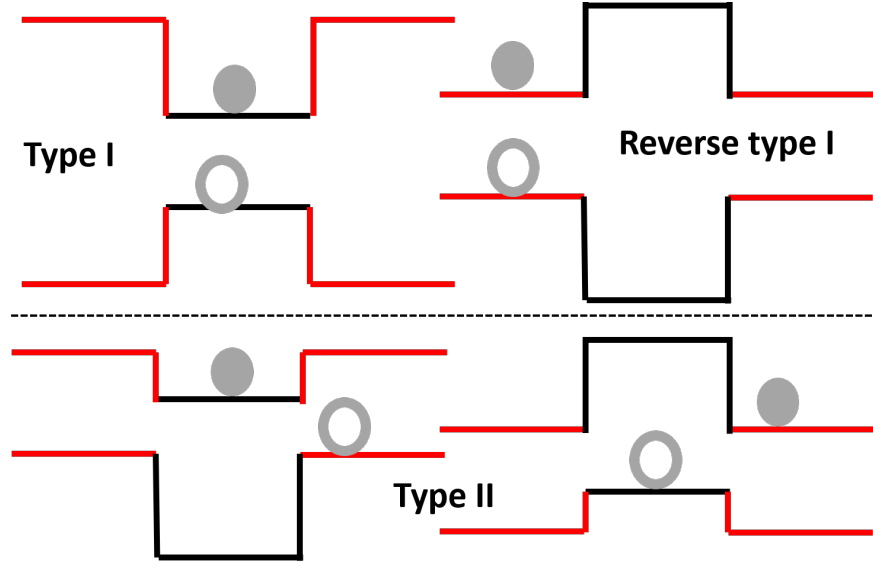
Figure 1.2: Different core/shell band alignments. Solid circle is an electron, open circle hole. A) Type I structure where both electron and hole reside in the core. B) Both electron and hole reside in the shell. C) Type II structures where one charge resides in core and other charge in the shell.

In a type I system, both the electron and hole reside in the core 1.2top. The shell serves to protect the core while also enhancing the electron/hole overlap for enhanced emission rate. The most famous example of a type I core/shell QD is CdSe/CdS, which has been studied extensively for the past 25 years and is the current state-of-the-art QD for LEDs [19] and lasing [22]. Other examples are CdSe/ZnSe, InAs/CdS, etc. A reverse type I system has both the electron and hole residing in the shell, which could be useful for efficient electron/hole extraction among other things. However, the shell typically has a much lower QY than the core. To remedy this, an additional shell may be grown, such as CdS/CdSe/CdS, but this would make extraction of the charge carriers less efficient.

A type II system has one charge carrier located in the core while the other is in the shell 1.2bottom, leading to a reduced electron/hole overlap and therefore a slowing down in the relaxation dynamics. This has important applications for carrier multiplication [23], solar cells and a wide variety of other applications. Common type II structures are PbSe/CdSe, CdS/ZnSe and CdTe/CdSe, among others.

1.2   Synthesis of Quantum Dots

The synthesis of QDs is an extremely active field, with work currently being done to make QDs with higher QY, more stable, new materials, new heterostructures, and much more.

Parallel to the development of epitaxial quantum wells/dots [24] and the development of molecular beam epitaxy [25], the first quantum dots were grown in glasses [5]. These were limited to sizes of ∼20 nm and had to be cooled in order for efficient light emission to be available from the system. However, the past 30 years has been dominated by colloidal chemical synthesis of QDs [26], which consist of inorganic cores coated with a layer of organic ligand molecules [27]. For covalently bonded semiconductors, an aerosol-based plasma synthesis is ideal for reaching the required elevated temperatures for nanoparticle formation to occur [28, 29].

1.2.1 Colloidal Synthesis

By far the most common form of making high-quality freestanding QDs is colloidal synthesis. There, a coordinating solvent stabilizer is heated to several $100°C$ wherein metal-organic precursors are injected. The elevated temperatures lead to the decomposition of the precursor reagents fueling nucleation of nanoparticles [10]. Growth then occurs by the addition of the precursor monomers in the solvent onto the QD. Once the monomer concentrations are depleted growth proceeds by Oswalt ripening in which the smaller QDs dissolve and then get absorbed by the larger QDs, decreasing the total number of QDs but increasing the size of the larger ones.

QD size is controlled by reaction time (larger times equals larger QDs), reaction temperature (higher temperatures lead to faster reactions), precursor concentration and nucleation temperature of the monomer [30]. In the coordinating solvent are organic ligands whose polar head group binds to the surface of the QD, with the ligand tail exposed to the solvent and prevents aggregation of the QDs in the solution. The ligand-QD attachment is dynamic, with the ligands popping on and off at the elevated synthesis temperatures. This allows QD growth to still occur while preventing agglomeration in the solution.

Of particular interest is size dispersion of the solutions; if the size dispersion is too large the discrete features in the absorption spectra will be smoothed out due to variances in the $1/R^2$ term in equation 1.2. It is the Oswalt ripening stage which leads to larger size dispersion in solutions as the initial fast growth is uniform and results in small size dispersions of merely $\sim 5\%$. To remedy this, often times rather than allowing the reaction to reach the Oswalt ripening the precursor monomer is either continuously injected or injected multiple times throughout the synthesis process [31].

1.2.2 Plasma Synthesis

While colloidal synthesis is ideal for the synthesis of II-VI, IV-VI, I-III-VI, and III-V semiconductor nanomaterials, the synthesis of group IV materials requires much higher synthesis temperatures to break apart the covalent bonds. To this end the plasma, or gas-phase, synthesis of QDs has become a viable alternative to colloidal synthesis [34] for group IV materials in particular but also for QDs accessible via chemical synthesis

Colloidal Synthesis   **Plasma Synthesis**
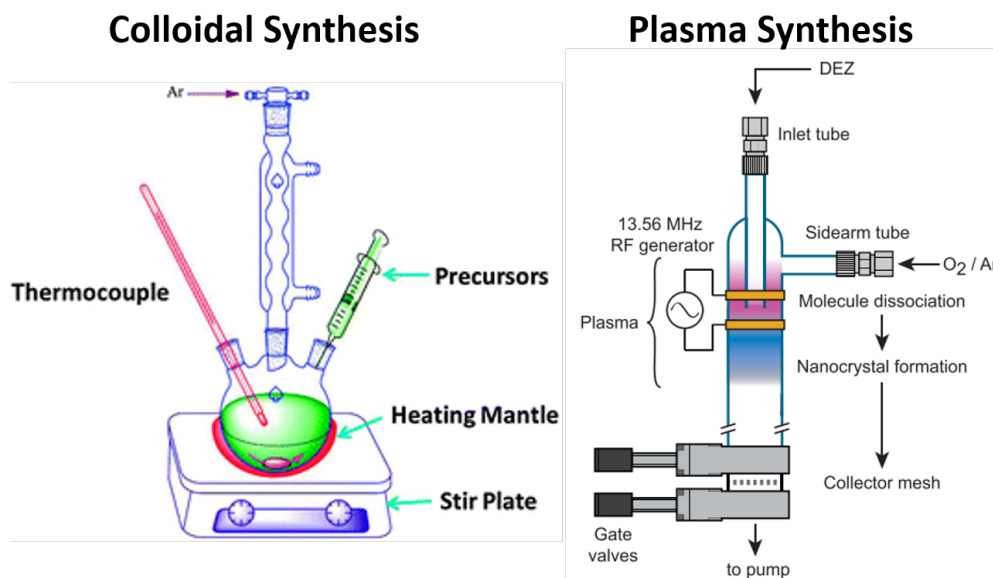
Figure 1.3: Colloidal synthesis is done in a heated flask on a Schlenk line, with precursors injected from a vial into a precursor. Plasma synthesis is done in a plasma, typically Ar, with precursors mixed with the Ar prior to being injected into the plasma. The precursors here indicate the synthesis of ZnO. Left figure reproduced with permission from ref [32] and right figure reproduced with permission from ref [33].

(for instance ZnO, see chapter 2).

Plasma synthesis does not require organic solvents or ligands necessary as in chemical synthesis, allowing for elevated reaction temperatures. Of particular interest is the non-thermal plasma synthesis, in which the atoms and precursors are near room temperature while the plasma electrons can reach temperatures as high as 50,000 K [29]. The free electrons disassociate the gaseous precursors which results in highly reactive ions and radicals which then form nanoparticles. The nanoparticles are negatively charged in the plasma preventing agglomeration without the need for organic ligands.

Silicon is the most famous example of a plasma-synthesized QD [35]; in its bulk form it is ubiquitous in the electrons industry and the efficient production of high-quality Si QDs is of great interest for industrial applications. Here it will be treated as a model system to describe plasma synthesis. Si QDs are formed in an argon plasma, with power applied via a RF power supply coupled to copper ring electrodes [36]. The silicon precursor is silane (SiH_4), which is diluted in the Ar flow (ratio $\sim$1:100) prior to

reaching the electrodes. In more recent developments, an H2 injection downstream is also introduced into the system to assist in surface passivation of the QDs [37, 38].

Analogous to synthesis time determining size in colloidal synthesis, in the plasma synthesis the particle size is controlled by the residence time in the plasma. This is in turn controlled by the flow rates of the precursors, with typical residence times being on the order of tens of milliseconds. The QDs are collected onto a mesh under the plasma, where they may be functionalized with organic ligands to passivate the surface and increase quantum yield. Alternatively, they may be deposited directly into films [39] by moving a substrate back and forth beneath the plasma, with QDs being deposited supersonically due to an orifice between the plasma and the collection chamber with a larger pressure difference. This is of great interest for devices utilizing charge transport, where insulating ligands would severely impede inter-QD electron hopping [40].

Dopants to the QDs can be added in situ via an additional precursor for the dopant, for instance phosphine (PH_3) or diborane (B_2H_4) to dope Si with phosphorous (n type) or boron (p type) [41–43]. The question is whether the dopants are incorporated to the QDs throughout their synthesis so there is uniform distribution, or the dopants aggregate onto the surface of intrinsic QDs [44]. Both situations have their own cons and benefits and much work is being done on controlling dopant locations during in situ doped QD plasma synthesis.

Over the past 15 years plasma synthesis has undergone a rapid growth around the world. To date, Group IV QDs have intensively studied (silicon, germanium and carbon), but also oxides, nitrides, phosphides, and sulfides have been synthesized in the non-thermal plasma. Additionally, the plasma synthesis can be used to grow metallic nanoparticles such as Ni, Fe, W, Au and Cu [29].

1.3 Applications of Quantum Dots

The ability to tune narrow emission spectra across the visible and IR spectrum opens the door for a wide variety of potential applications. The most obvious is in optoelectronic displays, such as televisions (figure 1.4A). Here, QDs may replace organic or bulk semiconductors to produce bright, high contrast displays due to their narrow emission lines compared to that seen in other emitting materials. Additionally, they require less

power to operate than traditional sources, of great importance in the world-wide transition to cleaner energies. The first QD TVs hit the market around 2015 and were 50-100 times brighter than liquid crystal displays.

The use of QDs in LEDs (termed QLED, in contrast to organic LEDs being OLED) are attracting heavy interest due to the above reasons. Recent advances have shown a reduction of 'droop', the saturation in emission intensity at higher voltages [45], and QLEDs with 100% internal quantum efficiency [46]. Both of these bode very well for efficient, practical devices in the near future. Auger recombination, the process in which the energy released by a recombining electron and hole is transferred to a third particle instead of a photon, inhibited practical QLED development for many years [47]. However, recent advances in synthesis engineering have led to the near complete suppression of Auger recombination [48] in QLED devices. Similarly, lasing in QD films has been of interest since their initial development; their wide range of tunability and cheap manufacturing cost would greatly exceed the standard commercial lasers using bulk semiconductors. One application of QLED or QD lasers is the use in micro-laser arrays or flexible electronics (figures 1.4B,D). The transition to electrically driven lasers is the next step, which should be reached within the next ~ 5 years.

QD solar cells have been investigated thoroughly over the past 15 years [49,50]. The most important part of any solar cell is the light absorber layer, which attempts to capture as much of the solar spectrum as possible. QDs, with their tunable absorption spectras, can be used to maximize collection efficiency. Often QDs are used in multi-junction solar cells where different QD compositions are used to catch different parts of the solar spectrum. Additionally, QDs have been found to be excellent materials for multiple exciton generation (MEG) [51]. In MEG a high energy photon is absorbed in a QD and generates more than one exciton, leading to an enhanced collection efficiency. In bulk materials this excess energy is quickly dissipated as heat but in QDs the separation of energy levels leads to this excess energy being utilized for work rather than dissipated.
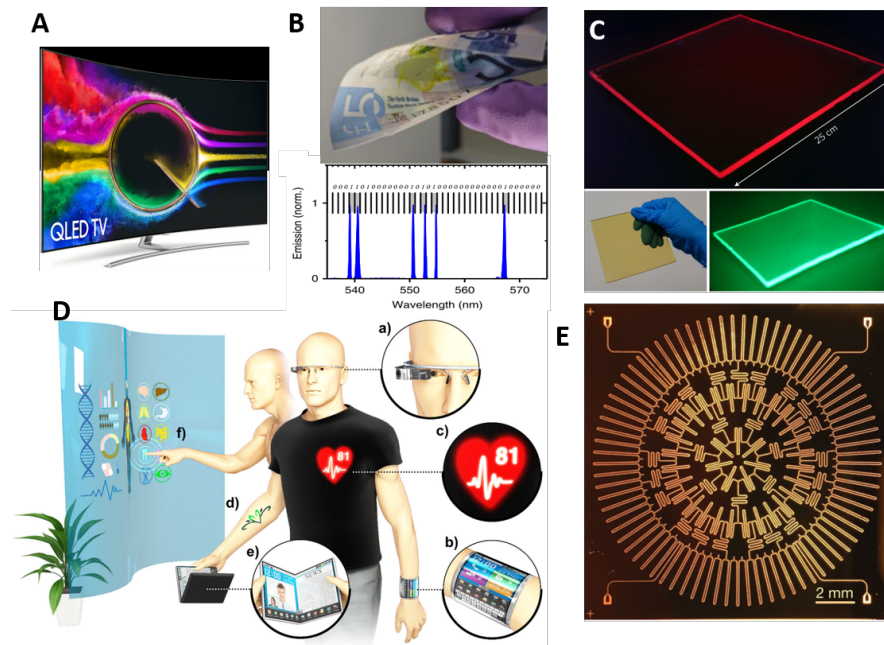
Figure 1.4: Selected applications of quantum dots: A) A Samsung QLED TV, image from Samsung website, B) 'Proof of concept' security bar-code using micro-laser array, from ref [52]. QDs could be used due to their narrow bandwidth and stability. C) A Si QD LSC shown under UV excitation with visible emission (top) and NIR emission (bottom right). The bottom left figure is the LSC under room light. Reused with permission from ref [53]. D) Wearable electronics in a variety of conditions: a) Smart glasses, b) smart watch with linked biosensors for in situ diagnostics, c) a display on a t-shirt, d) an electronic tattoo, e) bendable/foldable newspaper or tablet, and f) transparent window functioning as a working touch screen. Figure from ref [54]. E) A photonic circuit, reproduced with permission from ref [55]. In the future, the emitters may be QDs.

Luminescent solar concentrators (LSC) are devices for concentrating solar light to a small area, where a solar cell converts the concentrated light into electricity [56]. An LSC consists of a large surface area thin film, typically a polymer, which is partially infilled with a disperse collection of light absorbers, for instance quantum dots, which then re-emit the collected solar light and by total internal reflection is concentrated to

the edges of the LSC (figure 1.4C). Of vital importance is a separation between the absorption edge and emission spectrum of QDs, as significant overlap would lead to heavy re-absorption of the emitted light. To circumvent this, QDs with large stokes shift are used, such as Si or CISe [53, 57], so that re-absorption is minimized (see figure 1.4C).

The use of nanoscale QDs in devices also allows for the potential of flexible devices, capable of being worn or rolled up such as a newspaper would. Figure 1.4D shows a variety of potential applications of flexible/wearable electronics, of which QDs will play a vital role. In situ health monitoring, foldable smart tablets, and smart windows are just a few of the vast number of possibilities once flexible electronics hits the mass market [54]. Highly efficient QLEDs are a prerequisite for efficient wearable electronics, and the massive advances in that field indicate QD uses in wearable electronics is in the near future.

QDs are excellent sources of single photon emitters (SPEs), even at room temperature due to the separation of electronic states into discrete levels due to quantum confinement. The transition to quantum technologies is happening quickly [58, 59], and QDs are well positioned to play an important role in this process. QDs in cavities may be used to generate photonic qubit states, as shown in figure 1.4E. Generation, entanglement, transduction and collection of QD generated photonic states are all being heavily studied, with vast applications in quantum computing, metrology and information technologies [60–62].

These are just a few of the potential applications of QDs, emphasizing the broad applications relevant for next-generation devices. The near future looks very bright for QD applications as advances continue to be made at an astounding rate. More than 30 years old, the field is still continuously advancing as new materials with new properties are being developed and practical devices are being made.

1.4 Arrangement of topics

- Chapter 2 discusses the metal-insulator transition (MIT) in networks of ZnO NCs. After an introduction to MITs, in bulk materials and then in NC networks, we dive into a discussion of crossing the MIT through the use of photonic post-synthetic

sintering and doping and the use of atomic layer deposition (ALD) to protect the NC surfaces.

- Chapter 3 studies the synthesis, optical properties and electronic states of novel CdSe/HgS/CdS quantum dots in which we have monolayer control over the growth of the HgS layer. The band-alignment in this heterostructure results in electrons being localized in the HgS layer while holes are delocalized across the CdSe/HgS system, leading to interesting properties.

- Chapter 4 examines the multi-exciton dynamics of CdSe/HgS/CdS QDs. Through the use of high powered excitation many excitons can be pumped into each QD and analysis of the resulting PL decay provides insight into the electron and hole dynamics.

- Chapter 5 looks at CdSe/HgS/CdS QDs as potential single photon emitters (SPE). Thicker CdS shell growth is found to lead to superior quality SPEs, just as found in CdSe/CdS QDs. Such analogous behavior makes understanding of the single CdSe/HgS/CdS QD straightforward.

Chapter 2

Metal-Insulator Transition in a Semiconductor Nanocrystal Network

In this chapter we will explore the metal-insulator transition (MIT) in a semiconductor nanocrystal network. After an introduction to MITs, we will discuss the unique system of transport in faceted NC networks where the individual NCs themselves may be metallic but the network itself is insulating. Using an intense pulse light (IPL) flash annealing method, in addition to atomic layer deposition (ALD), we will explore independent control over the electron density n and inter-NC facet radius ρ. Then, through maximizing ρ and tuning n, we will provide unambiguous evidence for an MIT in an NC network. We will compare our results to theory, and use critical scaling analysis to study the critical exponents. At the transition we observe an unusual critical conductivity of the form $\sigma \propto T^{1/5}$.

2.1 Introduction to Metal-Insulator Transitions

The metal-insulator transition (MIT) is one of the oldest problems in condensed matter physics yet is still not thoroughly understood [63–65]. In contrast to a textbook metal or insulator, in semiconductor systems near the MIT the physical properties of the

system change drastically with minute changes of some physical tuning parameter such as charge density n, temperature T, pressure P or magnetic field H. Extreme changes in macroscopic variables due to small changes in the tuning parameter is usual in phase transitions, but in an MIT these changes are only evident near $T = 0$ because insulators carry a finite current at $T \neq 0$. Hence an MIT can only take place at zero temperature, i.e, the MIT occurs at a quantum critical point (QCP) [66]. Just as in the semi-classical phase transitions *a la* Landau's theory [67], at the MIT systems of different material or tuning parameter display a universality near the QCP. Near the MIT, the temperature dependence of the conductivity σ can be described by a phenomenological scaling law of the form

$$\sigma = \sigma_c f(\Delta t / T^y) \tag{2.1}$$

where $\sigma_c \propto T^x$ is the critical conductivity, x the critical conductivity exponent, t is the tuning parameter, $\Delta t = t\text{-}t_c$ denotes the distance from the critical value, f a scaling function with branches on the metallic and insulating side of the transition (depending on whether Δt is positive or negative), and $y = 1/\nu z$. Here ν is the critical exponent of the diverging length scales or localization length, $(\xi \propto \Delta \text{t}^{-\nu})$, and z that of diverging time scales $(\tau \propto \xi^z)$, describing the slowing down of relaxation near a QCP . Lastly, the conductivity as temperature goes to zero varies as $\sigma(T \rightarrow 0) \propto \Delta t^\mu$, and $x = \mu/\nu z$ [68]. The above formalism illustrates the remarkable nature of phase transitions, with all the material dependent parameters contained inside universal parameters [69].

The attempt for a quantitative quantum description of the MIT dates back to immediately after the development of quantum mechanics with Bethe, Sommerfeld and Bloch each separately showing that the the location of the Fermi level with respect to the energy levels governs whether a crystalline material is an insulator or metal [17, 70, 71]. Then Wilson distinguished metals and insulators via a model of non-interacting electrons [72] which gave rise to semiconductors as a distinct class of material different from insulators due to their small energy gap allowing thermal excitation of electrons into unpopulated band. This was followed by pioneering work by Wigner who introduced the electron-electron interaction into the understanding of metallic conduction [73, 74]. Mott then gave the first theoretical description of the MIT building off of the work by Wigner and Wilson [75, 76]. In Mott's simple model, he considered a cubic lattice of

odd-electron atoms (expected to be metallic due to Fermi statistics) with lattice constant d, and showed that at large d the system must be insulating while at short d the system metallic. This implies there must be some critical value d_c at which the transition from metal to insulator occurs. Alternatively, instead of changing d one could instead change the number of electrons, which Mott used to define the MIT criterion in terms of the electron density n and Bohr radius of the donor a_B,

$$na_B^3 \simeq 0.02. \tag{2.2}$$

Assuming a Bohr radius of 5 nm, this leads to a critical electron density $n_c \sim 5 \times 10^{17}$ cm^{-3}, easily reachable with doping techniques of the 1950s and 1960s [77].

2.1.1 Charge transport in nanocrystal networks

In disordered systems imperfections (such as lattice defects, fractures, dopants, surface effects, etc.) make utilization of Bloch's theory obsolete due to the scattering of Bloch electrons on these imperfections [78, 79]. Intuitively one might expect disorder to be more of a nuisance than a blessing but it turns out that disorder leads to extremely interesting novel phenomena, namely electron localization [80–82]. It was first discovered by Anderson that electron localization is possible in a disordered system when the disorder is strong enough [83]. With low disorder, or when the carrier density is very high, the kinetic energy of electrons is large enough that scattering off of impurities is negligible and transport can be described by the classical Drude model [84]. However, in low electron density systems the scattering may be strong enough to inhibit charge transport, resulting in bound electronic states. At finite temperatures this localization is destroyed by thermal effects, so the MIT is only observable at $T = 0$ K, where a continuous quantum phase transition occurs. A scaling theory of localization was then developed where Abrahams, Anderson, Liccardello and Ramakrishnan showed that the $T = 0$ conductance of a disordered system scales with the characteristic length scale in a universal manner [85].

Networks of semiconductor NCs are a prime example of a disordered system; fluctuations in NC size, packing density, electron density, film thickness, NC-NC separation, NC-NC crystal orientation and surface termination are just some of the inherent disorder in the system [86]. Electrons in an insulating NC network are localized via the

Anderson description because they are unable to traverse the NC network. Transport in an NC network is phenomenologically the same as through a disorder bulk semiconductor, with hopping between donors replaced with hopping between NCs. Charge transport between two NCs i and j can be described by a Miller-Abrahams network [87] with the conductivity between neighboring NCs given by

$$\sigma_{ij} = C\exp\left(-\frac{2r_{ij}}{\xi} - \frac{\epsilon_{ij}}{k_B T}\right),$$ (2.3)

where C is a temperature independent prefactor, r_{ij} is the distance between NCs, ξ the electron localization length and ϵ_{ij} the activation energy. In this model which considers all possible paths through an arbitrary lattice network conduction is dominated by the path of least resistance. At high temperature, or when ϵ_{ij} is small, transport is dominated by nearest neighbor hopping (nnh). In this case, the first term in equation 2.3 is a constant and the variation of σ with T is simply

$$\sigma_{nnh} \propto \exp\left(-\frac{\epsilon}{k_B T}\right),$$ (2.4)

where ϵ_{ij} has been replaced with the average activation energy ϵ.

More interesting situations occur when the two terms in equation 2.3 are comparable. In this situation there is a competition between the activation energy of sites i and j and the distance separating them; i.e, two neighboring sites might have very different activation energies while two distant sites have optimal energy offsets. This leads to what is known as variable range hopping (VRH) and results in a weaker temperature dependence of conductivity; the exact form of the temperature dependence depends on the density of states (DOS) used in the optimization of equation 2.3 as shown below.

Mott was the first to use the Miller-Abrahams network to tackle the conductivity of disorder systems [88]. He assumed a constant DOS based on the notion that at very low temperatures only states i, j very close to the Fermi level will contribute to the conductivity. Hence only small ϵ_{ij} will contribute to the current as there is not enough thermal activation to promote further away sites to sites near the Fermi level. Because the bandwidth of available states near the Fermi level is so small the DOS may be regarded as constant. If $g(\mu)$ is the constant density of states at the Fermi level, the concentration of states within the small, symmetric band about the Fermi level in which the relevant ϵ_{ij} exist is $n(\epsilon) = 2g(\mu)\epsilon$. Optimizing the Miller Abrahams network now,

with ϵ_{ij} expressed in terms of n and replacing r_{ij} with $n^{-1/3}$, leads to Mott's law for variable range hopping (M-VRH):

$$\sigma_M \propto \exp\left(-(\frac{T_M}{T})^{1/4}\right),$$ (2.5)

$$T_M = \frac{\beta}{k_B g \xi^3}.$$

Here T_M is a characteristic temperature, β a constant and ξ the electron localization length. The stretched exponent 1/4 is the characteristic signature of 3D M-VRH and can be easily found from experimental results by plotting the natural log of conductivity versus $T^{1/4}$.

Thus far the electron-electron interaction has been neglected, which of course needs to be included for an accurate description of hopping behavior near $T = 0$ when phonon processes are absent. Including the Coulomb interaction [89] alters the energy difference between the sites i and j: $\epsilon_{ij} = \epsilon_j$ - $\epsilon_i \rightarrow \epsilon_{ij} = \epsilon_j$ - ϵ_i - $\frac{e^2}{\kappa r_{ij}} > 0$, where the greater than zero term comes from the assumption that at low temperatures the system is in its ground state. Following the argument from above, where the states i, j are within $\pm \epsilon/2$ of the Fermi Level, the inequality leads to the requirement that $r_{ij} > e^2/\epsilon$, so that $n(\epsilon) \propto \epsilon^3/e^6$ and the DOS $g(\mu) = \frac{dn}{d\epsilon} \propto \epsilon^2/e^6 = (\epsilon_j - \epsilon_i)^2$. The quadratic dependence on energy in the DOS is termed the *Coulomb gap*, where there is a vanishing DOS at the Fermi level due to Coulomb repulsion between sites. Optimization of the Miller-Abrahams model with the quadratic DOS and the Coulomb term leads to Efros-Shklovskii Variable Range Hopping (ES-VRH):

$$\sigma_{ES} \propto \exp\left(-(\frac{T_{ES}}{T})^{1/2}\right),$$ (2.6)

$$T_{ES} = \frac{\beta e^2}{\kappa \xi}.$$

Here β is a numerical constant, κ is the dielectric constant and ξ the electron localization length. The 1/2 stretched exponent instead of 1/4 is the signature for ES-VRH, and as $T \rightarrow 0$ all semiconductors are expected to exhibit this behavior due to dominance of Coulomb interaction in this regime [3].

There have been numerous studies of charge transport in NC networks, and while the conductivity can be increased by orders of magnitude over initial NC films, to-date

the overwhelming majority of them have been insulators exhibiting variable range hopping transport [90–94]. In most cases the NCs are terminated in insulating ligands, a byproduct of their chemical synthesis origins [14], which makes inter-NC tunneling inefficient. Through ligand exchange, the length of the ligands can be decreased which increases the mobility by many orders of magnitude [95–97]. Additionally, ligand removal may be used to place colloidal NCs in direct contact [98], or the NCs may be synthesized in the gas phase [29,35] where direct contact NCs are achieved immediately. Even in NCs which are in direct contact, or faceted, the activation energies to free bound electrons is still high due to energy level misalignment between neighboring NCs [99]. Nearly all studies of temperature dependent conductivity in nanocrystal networks show variable range hopping behavior despite various attempts to dope [100], sinter [101] and conformally infill [102–105] NC networks. This has been has been attributed to the random charging of NCs due to different numbers of electrons in different NCs leading to a Coulomb gap. There has been promising studies with transport showing metallic or semi-metallic behavior [101, 103, 106–110] but to date there has been no thorough demonstration of an MIT in an NC network, even when the electron density exceeds the Mott criterion [100]. Evidently, a more strict criterion is needed for an MIT in an NC network.

To understand this, consider two adjacent NCs connected to each other via small facets of radius ρ, as depicted in figure 2.1A,B. These facets impede inter-NC electron transport leading to the situation where individual NCs may be metallic, with electron densities exceeding the Mott criterion, but the network itself insulating due to the facets between neighboring NCs. To describe the MIT criterion in this regime Fu, Reich and Shklovskii [99,100,111] derived a new MIT criterion for NC networks which depends on the electron density n and facet radius ρ rather than n and the Bohr radius a_B.

The inter-particle conductance between two materials connected via a small facet has been studied quasi classically [112] and results in a conductance of

$$G = \frac{e^2}{4\pi\hbar}k_F^2\rho^2, \tag{2.7}$$

where k_F is the electron Fermi wavevector and $\hbar$ is Plank's constant. The MIT will occur when this conductance is equal to the minimum metallic conductance $G = \frac{e^2}{\pi\hbar}$ [113]
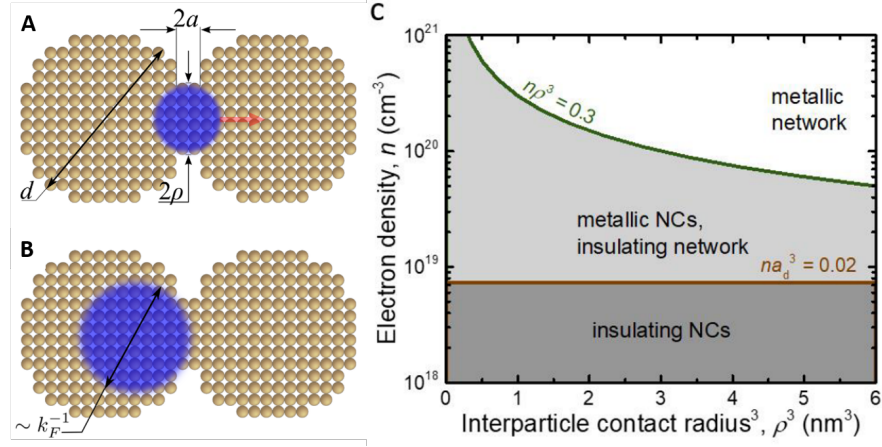
Figure 2.1: A,B) Schematic of a metallic and insulating NC network as a function of electron wavevector k_f and facet radius ρ. Figure reproduced with permission from reference [99]. C) Diagram of regimes of equations 2.2 and 2.10 as a function of n and ρ.

implying the criterion for an MIT in an NC network is

$$k_F \rho \approx 2. \tag{2.8}$$

Depicted schematically in figure 2.1A,B, electrons with large wavevectors may transverse through the facet while electrons with small wavevectors are scattered. Since the individual NCs are already metallic, the number of free electrons in an NC is large and hence can be described as a free electron gas with Fermi wavevector

$$k_F = \left(\frac{3\pi^2}{g}n\right)^{1/3} \tag{2.9}$$

where n is the density of electrons in an NC and g is the number of equivalent minima in the conduction band. Equating equations 2.8 and 2.9 leads to the criterion for crossing the MIT in an NC network:

$$n\rho^3 \simeq 0.3g. \tag{2.10}$$

This criterion leads to critical electron density for metallic behavior being several orders of magnitude larger than predicted via the Mott criterion. For instance, in 8 nm Si NCs the Mott criterion predicts an n_c of 3 x 10^{18} while equation 2.10 predicts $n_c \propto$ 5 x

10^{20}. This explains the results of ref [100] and other NC systems which had electron densities exceeding the Mott criterion but did not show metallic behavior. The phase diagram in figure 2.1C shows the relationship between insulating NCs, metallic NCs with an insulating network, and a metallic NC network as a function of n and ρ. At low electron densities, the Mott criterion is not surpassed and the individual NCs are insulating. As n is increased the Mott criterion is exceeded and the electrons become delocalized inside the NCs, but still the network itself is insulating due to the facets between NCs. Finally, the NC network may become metallic as some combination of n and ρ is increased. In the following sections we will attempt to cross the MIT by increasing both n and ρ in ZnO NC networks.

2.2 Controlling Electron Density and Facet Radius with Intense Pulsed Light in ZnO NC networks

Based upon the above arguments it is clear that in order to cross the MIT in an NC network both n and ρ must be increased. Previous studies of charge transport in ZnO NC assemblies have increased n via gating [92], and ρ has been increased by thermal sintering [101] or via conformal infill deposition of additional material into the NC network via ALD [103].

Here we work with plasma-synthesized ZnO NC films (synthesis described in Methods section) for which $g = 1$ due to the direct bandgap at the Γ point. ZnO NC networks have shown great promise for exhibiting metallic behavior; Thimsen *et al.* used thermal sintering and then Al_2O_3 ALD infill to passivate surface traps and attained electron mobilities as high as 3 $cm^2V^{-1}s^{-1}$ [101]. However, the thermal sintering increased the size of the NCs by a factor of 5, which makes utilizing the phenomena of quantum confinement in conductive NC networks impossible. Later, Lanigan and Thimsen used ZnO ALD to increase ρ prior to the Al_2O_3 infill, resulting in a 3 order of magnitude increase in conductivity at 2 Kelvin and a temperature independent electron density from 300 K to at least 100 K.

We build upon their work taking a new approach to changing the electronic properties of ZnO NCs via combining the Al_2O_3 ALD infill with a xenon flashlamp intense

pulsed light (IPL) annealing process [114–116]. IPL has numerous advantages to thermal annealing including being faster, easily extendable to roll-to-roll processing, and has the ability to be applied to almost all semiconductor materials [117]. We will show that with IPL on ZnO NC networks the electron density and facet size can be independently controlled by flashing the film before and after the ALD infill, all while keeping the NC diameter constant. IPL is applied under ambient conditions and the flashlamp has an energy density of 12 J/cm^2 with an 'on' duration of 1 ms and a repetition rate of 1 - 2 Hz.

2.2.1   Results

To increase ρ without increasing the NC diameter as deposited ZnO NC networks (no ALD infill) are flashed a variable number of times in the IPL system. ZnO has a wide bandgap but the UV portion of the Xe flashlamp is strongly absorbed by the ZnO NCs. When the photoexcited electron-hole pairs recombine or the holes recombine with negatively charged surface states the thermal energy released leads to sintering of the NCs. These 'hot' NCs will attempt to minimize their surface energy via necking, yet the high temperature duration is not long enough in the IPL process for grain growth to occur. Additionally, hole desorption on the surface leads to the possibility for new Zn-O bonds to occur, primarily between NCs (See Fig 2.2a).

Throughout this process, free electrons are being created as holes desorb onto the surface [118]. However, due to the NCs being in an ambient atmosphere n does not increase due to desorption of ambient species. Therefore, by applying IPL before the ALD infill we are able to increase ρ systematically while keeping n fixed. During the ALD process ρ also increases, due to the ALD step taking place at 180 °C leading to additional sintering (Fig 2.2b), but again n stays fixed.

After ALD the films are flashed again but now the situation is very different. Due to the Al$_2$O$_3$ infill the NCs no longer can sinter so ρ is fixed but the Al$_2$O$_3$ protects the NC surfaces from trapping species, so now any free electrons generated via the IPL process will remain free. Hence, with IPL after ALD we can independently tune n while keeping ρ fixed at the value from IPL before ALD.

We combine both of these processes to study the charge transport in ZnO networks as a function of $n\rho^3$. Specifically, we vary the number of IPL flashes before ALD from 0
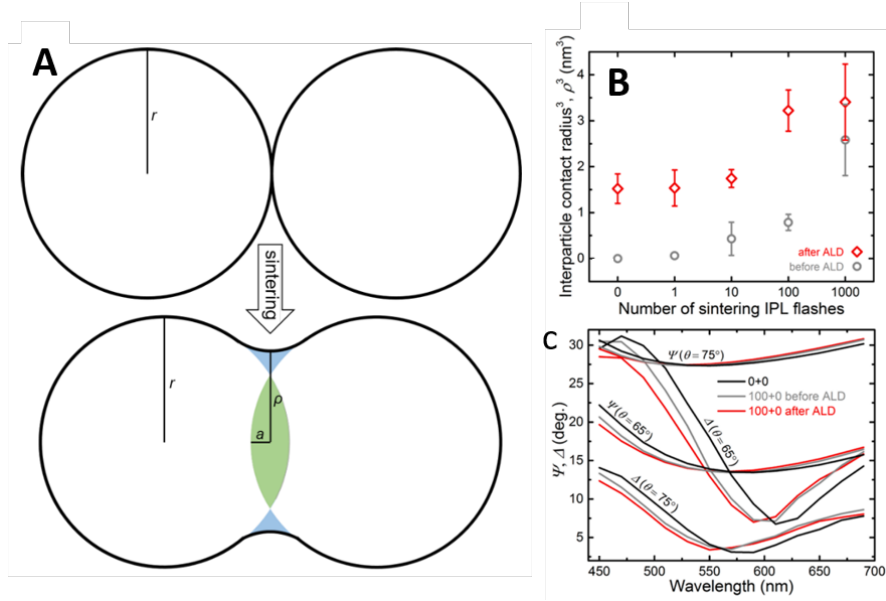
Figure 2.2: Sintering IPL. A) Schematic of NCs as deposited and then after 1000 IPL flashes before the ALD infill. The degree of sintering has been exaggerated for emphasis. B) ρ^3 as a function of IPL flashes. The red data points show the role that ALD does in further sintering the NC networks. C) Raw ellipsometry data where Ψ and Δ are then converted to L and ϕ

to 1000 (hereafter referred to as the sintering IPL step). We then take films that have been flashed 1000 times before ALD and vary the number of flashes after ALD from 0 to 1000 (referred to as the doping IPL step). The number of IPL flashes before/after ALD are represented in the form 'a + b' where a represents the number of sintering IPL flashes and b the number of doping IPL flashes. We do not study the transport properties of NC networks that have only been flashed after the ALD infill (i.e, '0 + b > 0'); due to the cubic dependence on ρ in equation 2.10 it is not possible to see metallic behavior unless ρ is increased beyond the point contact that exists after the film deposition. Essentially, we first vary sintering IPL such that the films go from '0 + 0' to '1000 + 0'. Then, we take the '1000 + 0' films and vary doping IPL flashes to reach the '1000 + 1000' film. There is additional phase space with reduced sintering flashes (i.e, '100 + 1000') that we do not explore here.

To directly quantify changes in ρ we use ellipsometry (figure 2.2C) to study the

packing density and film thickness of ZnO NC networks as a function of sintering IPL flashes. By measuring the porosity and thickness of multiple sport on a film after successive rounds of IPL systematic decreases in the film thickness L is seen along with increases in the packing density ϕ. Both of these changes are on the order of 5% when the number of flashes is varied from 0 to 1000. L and ϕ are related using a simple geometric model. After deposition adjacent NCs are connected via a point contact of radius ρ_0 = 0, with initial packing density ϕ_0. During sintering the NCs fuse together leading to an increase in the packing density ϕ and a decrease in the overall film thickness. The volumes of the blue and green sections in Fig 2.2A must be the same which allow for ρ and ϕ to be related. Using this method it is found that ρ increases from ~ 0 without sintering flashes to ~ 1.4 nm after 1000 sintering IPL flashes. However these measurements were done on films not exposed to ALD, which all the films for electrical characterization are. Because ALD is done at $180°C$, additional sintering may occur there. To simulate this films are heated on substrates at $180°C$ for 30 minutes prior to the ellipsometry measurements. These measurements indicate ρ increases from 1.15 nm to 1.5 nm as number of sintering IPL flashes varied from 0 to 1000. Evidently, most of the sintering comes from the ALD step! Further evidence for an increase in ρ while n is kept fixed is provided via electrical measurements, which will be shown later.

To increase the electron density of the films we take the 1000 sintering IPL series, infill the network with Al_2O_3 and then vary the number of doping IPL flashes. To measure the changes in n without measuring the films electronic properties we look at the Fourier transform infra-red (FTIR) spectrum of the ZnO localized surface plasmon (LSPR). We prefer this method over Hall measurements whose results can be difficult to interpret for low-mobility insulators exhibiting hopping conduction [119]. To estimate n we use the Maxwell Garnett effective medium approximation, which does not account for inter-NC conductivity but has been shown to produce good fits for NC films exhibiting hopping transport [120]. In this approximation the overall dielectric constant of the film, ϵ, is

$$\frac{\epsilon - \epsilon_m}{\epsilon + 2\epsilon_m} = \phi \frac{\epsilon_{NC}(\omega) - \epsilon_m}{\epsilon_{NC}(\omega) + 2\epsilon_m} \tag{2.11}$$

where ϕ is the NC packing density, ϵ_m is the dielectric constant of the surrounding medium (Al_2O_3 in this case), and ϵ_{NC} is the dielectric constant of the NCs given by the

Drude formula

$$\epsilon_{NC}(\omega) = \epsilon_\infty - \frac{\omega_p^2}{\omega^2 + i\omega\Gamma}. \tag{2.12}$$

ϵ_∞ is the high frequency dielectric constant (3.7 for ZnO), $\Gamma = e/\mu_l m^*$ is the carrier relaxation frequency, $\omega_p = \sqrt{\frac{ne^2}{\epsilon_0 m^*}}$ is the plasma frequency, m^* the electron effective mass ($0.3m_e$ for ZnO [121]), μ_l is the intra-NC mobility, n is the electron density, e is the elementary charge, ϵ_0 the permitivity of free space and i the imaginary number. For the '1000 + 0' insulating sample the imaginary part of ϵ is fit to the Maxwell Garnett effective medium approximation, which fits excellently as shown in figure 2.3b. This fit indicates an electron density of 1.1 x 10^{20} cm^{-3} and $\mu_l = 21$ cm^{2}V^{-1}s^{-1} (similar to other reported values). However, as the MIT is approached the transport mechanisms change making it unclear which effective mass approximation to implement and how to compare different samples. To remedy this we simply use the '1000 + 0' film, for which we know n, as a baseline and determine n for the more conductive samples based on the ratio of the area under their LSPR absorption feature, which depends linearly on n. This indicates that after 1000 flashes the electron density rises by a factor of $\sim$7 to $n = 7.6$ x 10^{20} cm^{-3}. This is comparable to the maximum n for bulk impurity doped ZnO and in photodoped ZnO NCs [122–124] and results in an $n\rho^3$ value of 2.6, much greater than the 0.3 criterion from equation 2.10.

We now examine the transport properties of the ZnO NC networks as a function of sintering and doping IPL to see if the MIT is crossed. All films studied henceforth have the Al$_2$O$_3$ added, whereas Al$_2$O$_3$ was excluded for some optical measurements to make measurement possible. First we examine the room temperature conductivity of ZnO NC networks as a function of IPL flashes before/after ALD. Figure 2.4B shows that the sintering IPL series (red) serves to increase the electron mobility of the networks by 2 orders of magnitude while n remains fixed as described previously. The conductivity

$$\sigma = \mu n e, \tag{2.13}$$

where μ is the electron mobility, also increases by 2 orders of magnitude (figure 2.4A). This can be easily understood through the increased facet size permitting electrons to explore other NCs unimpeded compared to the the NCs connected via point contact.

For the doping IPL series n increases while μ is essentially constant due to IPL removing carnivorous species from the surface via hole oxidation [118]. The conductivity
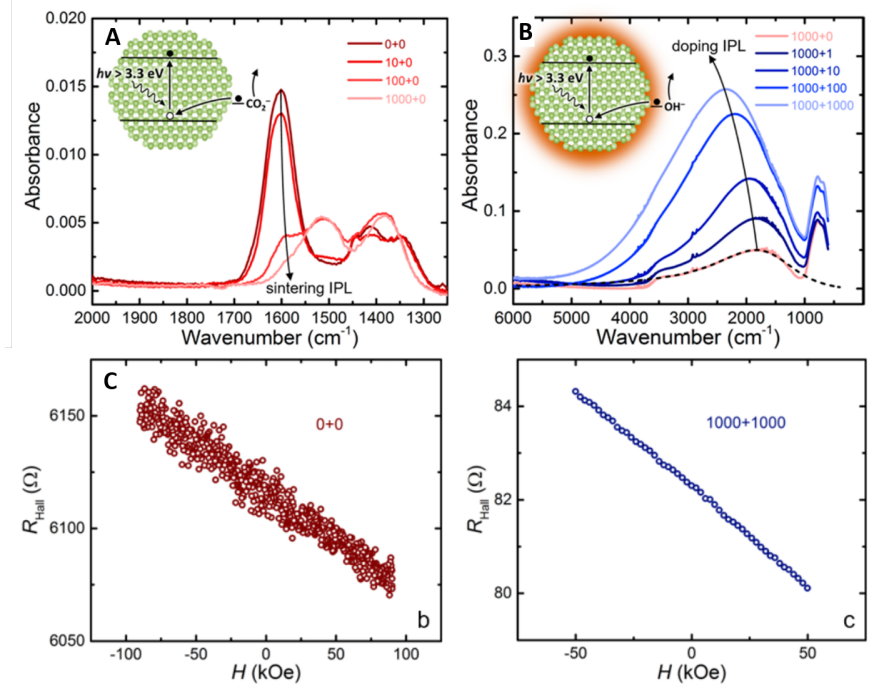
Figure 2.3: FTIR spectra. A) Sintering IPL effect on the 1600 cm^{-1} carboxylate feature due to removal of surface states via hole adsorption, as shown in inset. B) Doping IPL effect on the LSPR feature of ZnO NCs. The salmon curve is that of a film with no doping IPL flashes, and remains unchanged as the number of sintering IPL flashes is varied. C) Hall measurements of a film with no IPL flashes versus one with 1000 flashes before and after ALD.

of these NCs degrades in ambient conditions at the rate of about 1% per day while keeping the films in an inert nitrogen glovebox leaves the films stable for at least several months. Both the '1000 + 100' and the '1000 + 1000' network conductivity are greater than the minimum metallic conductivity $\frac{e^2}{\pi \hbar}$.

To provide further evidence of an increase in n we perform Hall measurements for all samples, of which the least and most conductive are shown in figure 2.3C. While sourcing a constant current of 10 μA across the diagonal of the film (see Methods) and sweeping the magnetic field from about -10 to 10 Tesla we measure the voltage induced across the other film diagonal, which is related to the free carrier density by

$$V_H = -\frac{IB}{neL}, \tag{2.14}$$
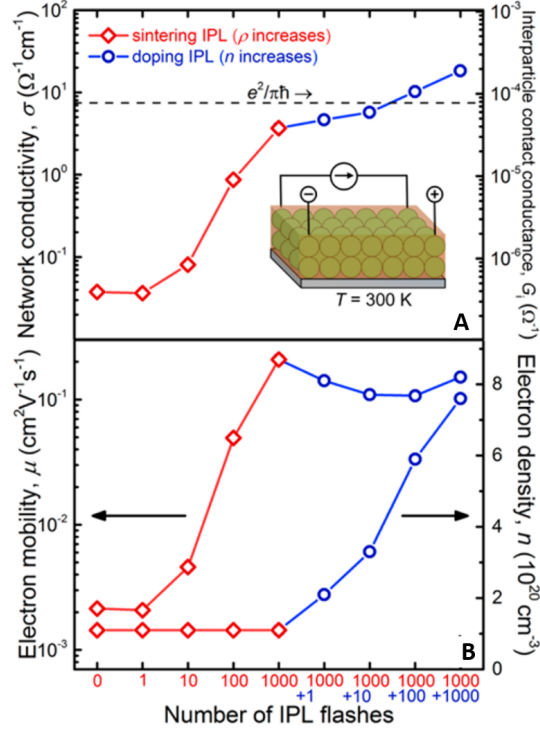
Figure 2.4: A) Network conductivity and inter-NC contact conductance as a function of IPL flashes. Red denotes sintering IPL series and blue the doping IPL series. B) Electron mobility (left) and electron density (right) as a function of IPL flashes. Mobility increases with flashes before ALD while electron density remains fixed, and vice versa after ALD.

where I is the current, B the magnetic field, n the electron density, e the charge of an electron and L the film thickness (assumed to be 300 nm for all films). Interestingly, the Hall measurements indicate an increase of n during the sintering IPL series ('0 + 0' to '1000 + 0'). As stated previously, Hall measurements in insulating samples is often difficult to interpret [119] so we attribute the apparent increase of n in Hall measurements to be due merely to increased Hall mobility. The Hall measurements indicate that n increases from 1.1 to 7.6 x $10^2$0 cm$^-$3 from before/after 1000 doping IPL flashes.

Both n and ρ are found to saturate after ~1000 flashes of IPL, with increasing the flashes to 2000 producing only slight, 1%, increases to the relevant variables. However with 1000 IPL flashes before/after ALD $n\rho^3$ is found to increase up to 2.6, well above

the predicted criterion of 0.3. Both flashes before/after ALD are needed to create conductive ZnO NC networks as the sintering and doping steps are done separately.

To study the nature of the transport mechanisms in these NCs we perform temperature dependent studies of the conductivity using a Physical Properties Measurement System (PPMS) which can reach temperatures below 2 K. Figure 2.5a shows the temperature dependence of the NCs on a $\log(\sigma)$ vs $T^{1/2}$ scale. The linear behavior of the data (particularly the more insulating red samples) indicates that on the insulating side of the transition the conduction is due to the ES-VRH mechanism, equation 2.6. As the films are doped after sintering (blue data points) the temperature dependence gets weaker than $T^{1/2}$ indicating an approach towards metallic behavior. Indeed, the most conductive network sees the conductivity drop by only a factor of 10 when varying T from 300 K to 2 K.

The characteristic temperature in ES-VRH depends inversely on the dielectric constant and the localization length, $T_{ES} \propto \kappa^{-1}\xi^{-1}$. Figure 2.5b plots T_{ES} versus $n\rho^3$. The vertical dashed line indicates the MIT criterion derived by Reich, Fu and Shklovskii [99, 100] while the horizontal dashed line uses the bulk ZnO dielectric constant (9) and the nanocrystal diameter (d) to estimate ξ. The super-linear drop of T_{ES} as $n\rho^3$ increases is indicative of a rapid approach to the MIT. Both κ and ξ diverge at the phase transition and our experiments do not isolate the two variables. As a rough approximation if κ is fixed then ξ increases to greater than 10 NC diameters, whereas previous work showed only ξ increasing to $\sim$4 NC diameters.

To verify if the MIT was crossed we compare our results directly to published MIT literature. Figure 2.6A,B is data from a classic paper on the MIT in boron doped Si films [68] where uniaxial stress was used to tune the sample (reversibly) through the MIT. As shown in equation 2.1, at the transition we expect to see power law conductivity of the form $\sigma \propto T^x$. To see this, one simply plots σ versus T on a log-log scale where the power law will show up as a straight line with slope x. In A), the power-law behavior is seen in the middle of the graph with a slope equal to 1/2, indicating $\sigma_C \propto T^{1/2}$. The bottom half of the figure A shows σ approaching 0 as $T \to 0$, indicative of insulating behavior. Meanwhile the top half of the plot shows finite σ as $T \to 0K$, indicative of a metal. It is only at the transition that power-law conductivity, $\sigma_c \propto T^{1/2}$, is seen which agrees with theory.
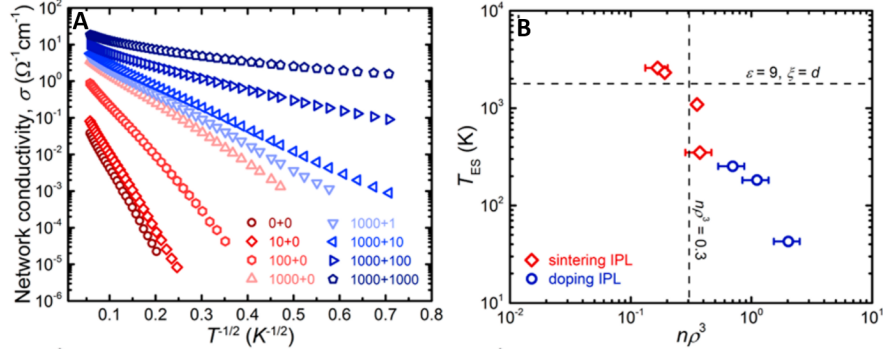
Figure 2.5: A) Temperature dependence of the conductivity plotted versus $T^{-1/2}$. The curvature of the high conductivity films indicates an approach to the MIT. B) Efros-Shklovskii characteristic temperature plotted versus $n\rho^3$ indicating a divergence of the dielectric constant and localization length as the MIT is approached. Vertical line is critical $n\rho^3$ criterion and horizontal line is T_{ES} with bulk ZnO dielectric constant and localization length equal to the NC diameter.

The second term in equation 2.1, $f(\Delta t/T^y)$, is the scaling function with branches on both sides of the transition. The scaling analysis is applied to the data of figure 2.6A in figure 2.6B with applied stress S the tuning parameter t, S_c the critical stress leading to power law curve in 2.6A and $y = 0.31$. The data sets clearly collapse onto two curves corresponding to insulating (bottom) and metallic (top) transport behavior. The exponent y is found through trial-and-error in determining best fit and indicates critical exponents $\mu = 1.6$ and $z\mu = 3.2$.
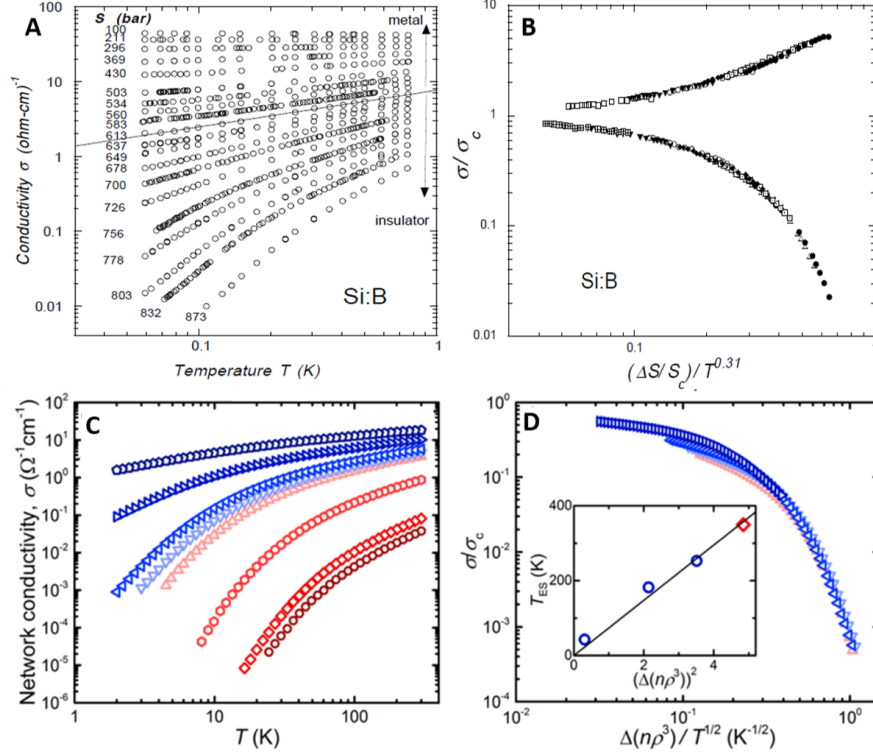
Figure 2.6: A,B) Scaling of the conductivity through the MIT in boron doped silicon. Reproduced with permission from reference [68]. A) Scaling of conductivity with pressure as a function of temperature. The critical curve at the MIT has power law of 1/2. B) The collapse of the insulating and metallic curves into two branches via the critical scaling relation equation 2.1. C) Conductivity versus temperature on a log-log scale of our ZnO NC networks. Same data as in 2.5A but plotted on log-log scale. D) Collapse of the insulating branch onto one curve near the MIT. Since the MIT is not crossed the metallic half of the scaling curve is not observable.

Analogous plots of our data with that of Bogdanovich *et al.* [68] is shown in figures 2.6C,D making it evident that we do not obsserve an MIT. While our most conductive sample ('1000 + 1000') only sees an order of magnitude drop in conductivity from room to cryogenic temperatures, on a log-log plot σ vs T is seen to have negative curvature indicating $\sigma(T \to 0) = 0$. However, the shallowness of the T dependence on σ and the near linearity of the curve indicates that the MIT critical point is close. To this end

we perform the scaling analysis using equation 2.1 with t now equal to $n\rho^3$. Because the transition was not actually seen, the critical curve is approximated by letting the most conductive sample be the critical curve with an $n\rho^3$ value of 2.6 and assuming that $\sigma_C \propto T^{1/2}$. The next four highest conductivity films is then shown to collapse onto a single scaling curve in figure 2.6D (with the more insulating curves not obeying the scaling behavior as they are far from the MIT and show standard ES-VRH behavior) with $y = 1/2$ yielding the best fit. Due to our not crossing the MIT, only scaling on the insulating side is possible and the use of $x = 1/2$ was based only literature values to show the closeness of our results to the MIT.

Our maximum measured value of $n\rho^3$ is significantly higher than the predicted MIT criterion of $n\rho^3 \sim 0.3$. As we do not observe an MIT equation 2.10 evidently errors on the side of underestimating the MIT criterion.

2.2.2 Conclusions

In this section we have shown the utility of IPL to enhance the conductivity of ZnO NC networks. Through applying IPL before/after the ALD infill, we are able to independently control the NC-NC facet size and the electron density without changing the NC diameter. This process should also be achievable in other NC materials, which will lead to high mobility NC networks that are still in the quantum confinement regime. While we performed all IPL measurements in ambient conditions, IPL under inert conditions could lead to a simultaneous enhancement of ρ and n; future work could relate the increase of n and ρ as surface hydroxyls and carboyxlates are removed.

Temperature dependent conductivity measurements indicate that through the IPL treatments we were able to nearly get to the MIT transition in a NC network. Evaluation of the most conductive sample with the NC MIT criterion proposed by Shklovskii *et al.* indicates equation 2.10 errors on the side of underestimating the critical $n\rho^3$ for the MIT. To cross the transition either n or ρ must be increased further. We found that applying more IPL flashes to the sample after 1000 yielded negligible increase to n in ZnO NC networks, so in order to increase $n\rho^3$ we must increase ρ. While it was shown that this cannot be done by IPL, it can be done via ZnO ALD infill into the NC network prior to the Al_2O_3 ALD infill [103]. This will be examined in depth in the next section. Of course, the MIT in NC networks is not limited to ZnO, and the transition could

be crossed with the same facet size by using a material with a higher intrinsic electron density such as ITO [106].

2.2.3   Methods

Sample Preparation: NCs were synthesized and deposited using a non-thermal plasma reactor (see chapter 1). To synthesize ZnO NCs diethylzinc (DEZ) is injected into a low pressure RF argon/oxygen plasma. The NCs form a high velocity particle beam when travelling through a rectangular orifice before being deposited inertially on a moving substrate. The NC diameter is controlled by the DEZ flow rates, which here lead to 10 nm NCs. The film thickness is controlled by the duration of deposition with films here being deposited for 60s and being 300 ± 30 nm thick. All samples were exposed to air immediately upon removal from the plasma reactor. NC networks were infilled with Al_2O_3 using a Cambridge Nanotech/Ultratech Savannah S200 ALD system. 70 cycles of ALD are done to completely infill the sample. One deposition cycle consists of four steps: (1) a 0.1 s H2O pulse, (2) a 30 s nitrogen purge, (3) a 0.1 s TMA pulse, and (4) a 30 s nitrogen purge. This infilling was done before all electrical characterization. Sintering and doping IPL were performed under ambient conditions using a Xenon Corporation Sinteron 2010 equipped with a 10 in. Xe U-lamp flashlamp operating at 3 kV.

Electron transport measurements. Transport measurements were conducted on 1x1 cm samples on boro-aluminosilicate Corning Eagle XG glass substrates under He vapor using a Quantum Design Physical Property Measurement System (PPMS). The van der Pauw method was employed with Al contact pads at the four corners of each square. The Al pads were deposited by thermal evaporation after ALD and IPL, and Au leads were attached to the Al by either wire bonding or soldering. For the conductive samples, a current from -10 to 10 uA was applied using a Keithley 220 current source and the resulting voltage measured using a Keithley 2182 nanovoltmeter. Above 10 Mohms the voltmeter reached its input impedance so for the less conductive samples a Keithley 6517A electrometer was used, where we applied a voltage from -1 to 1 Volts and measured the corresponding current. A Keithley 2700 switch box was used to perform the measurements in all possible configurations and ohmic behavior in four and two-point configurations was confirmed at 300 and 2K. The four-point conductivity in both configurations were then used to calculated the sheet conductivity from van der Pauw's

formula [125],

$$\exp\left(-\pi\sigma_S/\sigma_1\right) + \exp\left(-\pi\sigma_S/\sigma_2\right) = 1, \tag{2.15}$$

where σ_S is sheet conductivity (the conductivity shown in all plots), and $\sigma_{1,2}$ is the conductivity from one of the two possible configurations. Measurements of the temperature dependence of σ were done in the PPMS while it was warming from 2 K to 300 K. The temperature was allowed to stabilize before each σ measurement, and the resulting σ vs T curve was compared to the cool down curve to ensure film stability. Hall measurements were performed using a DC excitation of 10 μA.

Other Characterization: FTIR spectra were acquired under an N2 atmosphere from samples on polished NaCl substrates using a Bruker Alpha IR spectrometer in transmission mode. Ellipsometry spectra were acquired from samples on boro- aluminosilicate glass (Corning Eagle XG) substrates using a J.A. Woolam M44 ellipsometer. Prior to NC deposition, the backs of the glass substrates were roughened with a grinding wheel to prevent backside reflection during measurement. Spectra were fitted in WVASE using the Bruggeman effective medium approximation, assuming two components: ZnO and void. XRD patterns were acquired from samples on glass and Si substrates using a Bruker D8 Discover diffractometer equipped with a Be area detector and a Co Kα source. The collected patterns were mathematically converted to Cu Kα patterns. NC diameter, d, was determined using the Scherrer equation with a geometrical correction factor of 4/3 to account for the NCs' spheroidal morphology. SEM was performed on samples on glass substrates at an accelerating voltage of 5 keV.

2.2.4 Acknowledgements

2.3 Crossing the MIT in ZnO NC networks

In the previous section it was shown that intense pulsed light can be used to selectively sinter and dope ZnO NC networks. We were able to observe scaling behavior of the conductivity on the insulating side of the transition, indicating proximity to the MIT, though the most conductive samples were still insulating in nature. The measured values of $n\rho^3$ for the most conductive samples were greater than the predicted MIT criterion of $n\rho^3 \propto 0.3$ indicating equation 2.10 errors on the side of underestimating the MIT.

In this section we induce an MIT in ZnO NC networks by combining the sintering and doping IPL studied previously with an additional ZnO ALD step prior to the Al_2O_3 infill. The use of ZnO ALD to increase σ was previously studied by Lanigan and Thimsen [103]; they used as-deposited plasma-synthesized ZnO NC networks, coated the film with varying cycles of ZnO ALD (between 0 and 16), and then infilled the remaining voids in the NC network with 40 cycles of Al_2O_3 via ALD. They calculate that this increases ρ from ~ 0.7 nm to ~ 3.5 nm after 16 cycles of ZnO ALD, increasing the Hall mobility from 0.3 $cm^2V^{-1}s^{-1}$ to 5 $cm^2V^{-1}s^{-1}$. Temperature dependent analysis

of n indicates n is constant down to at least 100K, indicating lack of thermal activation in the transport of electrons, a sign of metallic behavior. However, their most conductive sample (whose conductivity drops by only a factor of ~ 5 with T varied from 300K to 2K) still shows negative curvature at low temperatures indicating $\sigma(T \to 0) = 0$.

2.3.1 Results

In this section we build upon their work by synthesizing conductive ZnO NC networks in the following manner: first, as-deposited plasma-synthesized NCs are flashed 1000 by IPL to maximize ρ. Then, ρ is further increased via deposition of additional ZnO into the network via ALD. Only eight cycles of ZnO ALD is used to prevent the NC network from turning into a granular material (i.e, we still believe the film is nanocrystalline in nature). Then the film is completely infilled with Al_2O_3 to render the network conductive [101, 103]. Lastly the number of doping IPL flashes is varied from 100 to 1000 to tune the NC network through the MIT. The tuning parameter in this study is the free electron density n, which is tuned in the last step. To summarize: first ρ is increased through photonic sintering then increased further with ZnO ALD and the remaining pores are infilled with Al_2O_3. Lastly, n is increased in a fine-tuned manner to observe the MIT. For schematic of the ZnO NC network and detailed micrographs of the system see figures 2.7 and 2.8.

All films receive the same treatment prior to the doping IPL step. The sintering IPL step results in $\rho \sim 1.5$ nm. To increase ρ further the NCs are conformally coated with additional ZnO by eight cycles of ALD using diethylzinc, trimethylaluminum and water precursors prior to infilling the network completely with 70 cycles of Al_2O_3 ALD. This results in networks with $\rho = 2.8 \pm 0.1$ nm, diameter d $= 10.4 \pm 0.2$ nm, average thickness L $= 300 \pm 30$ nm and porosity $\phi = 0.47 \pm .02$. The intrasample fluctuations of the above parameters are discussed in the methods section.
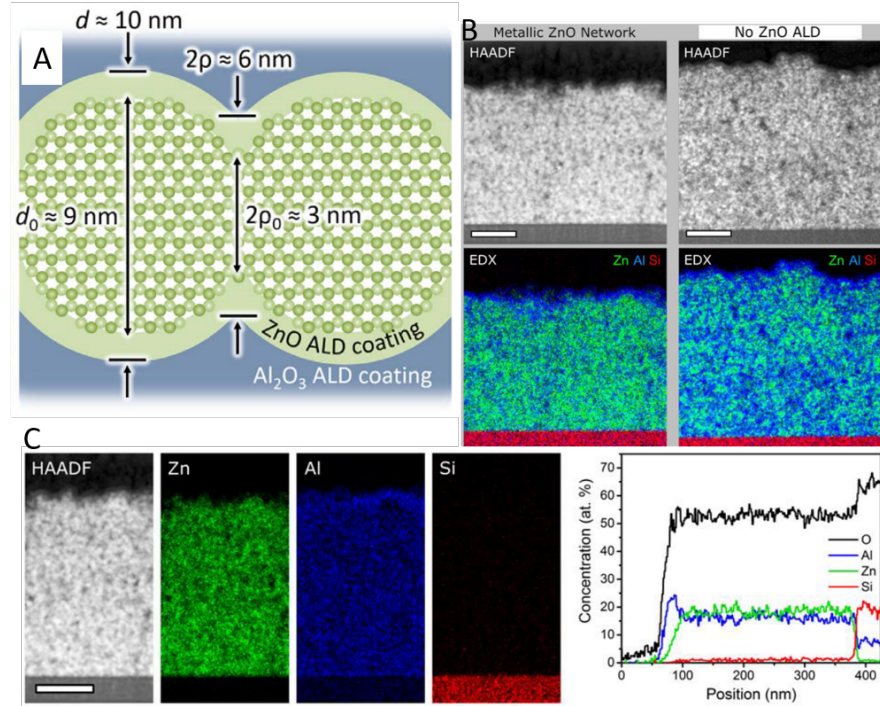
Figure 2.7: A) Schematic of neighboring NCs showing approximate relevant dimensions. B) Scanning transmission electron micrographs of metallic/insulating ZnO NC network lamella (thickness 50 nm) milled by focused ion beam. The corresponding colored graphs are composite energy-dispersive x-ray (EDX) spectral images showing counts of Zn (green), Al (blue), and Si (red). C) Elemental distribution of a metallic ZnO NC networks. HAADF-STEM and EDX spectral images showing the raw counts for Zn, Al, and Si for each of the networks. Right: Approximate atomic % of all relevant elements across the same regions demonstrating uniform and conformal coating with both ZnO and Al2O3 throughout the films. All scale bars are 100 nm.

Because now the system is very near the MIT henceforth n will be that measured via the Hall effect, n_{Hall}, and later this will be related to the electron density measured via the LSPR feature, n_{LSPR}. This is contrary to the last section where n_{Hall} results were difficult to interpret because the network was insulating. Varying the number of doping IPL flashes increases n from 2.2 x 10^{19} cm^{-3} to 6.9 x 10^{19} cm^{-3}. This value is well above the critical n for the Mott criterion so it is expected that all individual NCs are metallic

and hence the electron density will not change with temperature. In ZnO networks with similar electron density as ours n was found to be constant down to at least 100 K and there is no reason to expect n to change at lower temperatures [103]. At 300 K, σ varies from 16 to 92 ohm^{-1}cm^{-1} and the mobility from 4.5 to 8.3 cm^{2}V^{-1}s^{-1}. The highest conductivity achieved is three times that from our previous work and results in an inter-NC conductance range of 2 x 10^{-4} to 10 x 10^{-4} ohm^{-1}, well above the minimum metallic conductance e$^2/\pi\hbar = 8$ x 10^{-5} ohm^{-1}.
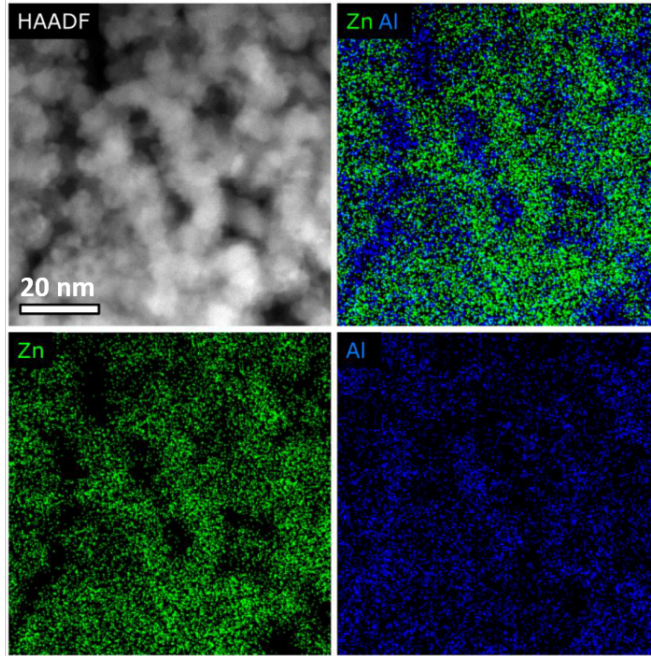
Figure 2.8: Higher magnification STEM/EDX images than in figure 2.7. While individual NCs (diameter 10 nm) can be distinguished in the images direct measurements of ρ are still not possible on these samples with current state-of-the-art microscopy.

The temperature dependence of σ in figure 2.9A provides unambiguous evidence of crossing the MIT. For $n\rho^3 < 0.71$ σ has positive slope and a negative curvature so that $\sigma(T \to 0) = 0$, indicative of insulating behavior. The most insulating sample, which incidentally is comparable to our most conductive sample in the previous section, has a slope of $\sim$0.5 on the Zabrodskii plot [127] in the inset of figure 2.9A, representative of ES-VRH (equation 2.6) and in agreement with previous results. However, for $n\rho^3 >$

0.71 $\sigma(T)$ has nearly zero slope and negative curvature, indicating a finite σ as $T \to 0$. For the most conductive sample $\sigma(T)$ is constant between 50 mK and 2 K, and at high temperatures the sample has negative slope (figure 2.9C) indicating a transition to the phonon-scattering dominated regime typical of metals [1]. The black data points in figure 2.9A are from an ALD grown fully-dense polycrystalline ZnO thin film. $\sigma(300$ K) of the most conductive NC sample is merely a factor of two below that of the polycrystalline film indicating we are close to reaching the maximum possible σ for a ZnO thin film, whether it be polycrystalline or nanocrystalline.

At $n\rho^3 = 0.71$ the critical curve $\sigma_c(T)$ follows a power law of $\sigma_C \propto T^{1/5}$ indicated by the solid line in figure 2.9A. In the inset of figure 2.9A, the critical curve has zero slope on the Zabroskii plot confirming the power law conductivity. Theory predicts power law behavior at the MIT to be with exponent x equal to 1/2 or 1/3 [128, 129]; the small exponent of 1/5 is very unusual. In the previous section we estimated the critical curve to be of the form $\sigma_C \propto T^{1/2}$ but this was done as an estimation using establish theory as the MIT was not seen there. Small values of x has been seen previously in the MIT of highly-correlated Mott-Hubbard systems YH_x [130] and $NiS_{2-x}Se_x$ [131], but these systems are very different from ours and the small x value likely has a different physical origin.

Interestingly, a theory for the frequency-dependent conductivity at the MIT [132] predicts an exponent of 1/5 would arise in fractal dimension $\tilde{d} = 2.5$. However, fractal transport has been studied quite rigorously over the past 25 years and most disordered systems have a fractal dimension of $\tilde{d} \approx 4/3$ [133], and additionally the MIT in fractal systems is known to not exist in systems with $\tilde{d} < 2$ [134–136]. $\tilde{d} = 2.5$ could be rationalized in disordered, porous, faceted networks such as ours with a thickness of $\sim$30 NC layers but is unprecedented in the literature so we are hesitant to attribute our results to such an explanation without further evidence. The concept of NC networks as fractals has been investigated [137–141] where fractal dimensions of $\sim$1.4 to $\sim$2.1 were found; perhaps future studies will investigate this across the MIT.
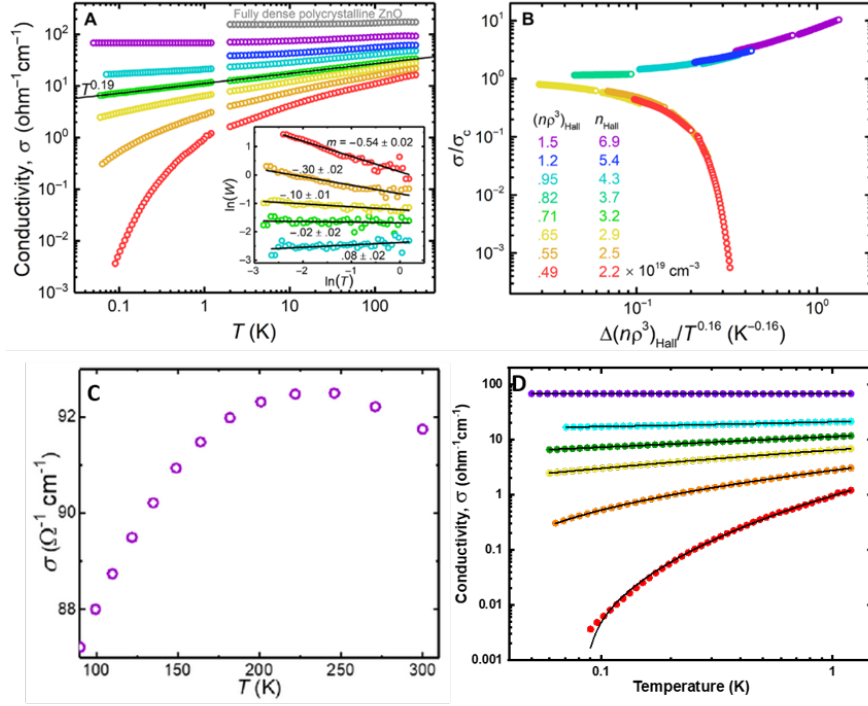
Figure 2.9: A) σ vs T for films with different $n\rho^3$. The black curve is an ALD grown fully dense ($\phi = 1$) polycrystalline ZnO film. B) Collapse of both sides of the transition into the two branches of equation 2.1. C) Enhanced view of the transition to the phonon-scattering regime of the most metallic NC network. D) Fits (black lines) to low temperature σ data from figure A for 5 of the samples.

Fits to the low temperature data for five of the samples is shown in figure 2.9D. Units are left off the fits for convenience; the units may be interpreted as needed. On the metallic side, the fit is of the form $\sigma(T) = \sigma_0 + BT^C$. The critical curve is fit with $A = 0$, resulting in $\sigma_c(T) = \sigma_{green}(T) = 11.29T^{.191}$. C is then fixed to .191 for the remaining fits. Doing so results in $\sigma_{blue}(T) = 10.46 + 10.42T^{.191}$ and $\sigma_{purple}(T) = 67.69$, a constant. On the insulating side the fits are done to the form $\sigma(T) = \sigma_0 + B*\exp\left(-(\frac{T_{ES}}{T})^{1/2}\right)T^C$, where the ES-VRH 1/2 term comes from the red curve in figure 2.9A (The Zabrodskii plot indicates the stretched exponent on the red curve is 0.55 but we use 0.5 in the fits due to the established theory of Efros and Shklovskii. This is the cause for the poor fit at low T on the red curve in figure 2.9D while the power law $T^{1/2}$ fits

the high T portion nicely). Intuitively C was again fixed to be 0.191, but the resulting fits were poor so C was allowed to be a free parameter. This resulted in $\sigma_{yellow}(T) = 0.539 + 2.58\exp\left(-(.016/T)^{1/2}\right)*T^{.26}$, $\sigma_{orange}(T) = $ -0.23 + 3.71$\exp\left(-(.046/T)^{1/2}\right)*T^{.39}$, and $\sigma_{red}(T) = $ -.0070 + 4.35$\exp\left(-(2.27/T)^{1/2}\right)*T^{.50}$. Such a change in the power law exponent has been seen before [142], when Maliepaard *et al.* used the work of Altshuler and Aronov [128] to argue that for systems where interactions are important $\sigma = $ A + B$T^{1/2}$ for low disorder becomes $\sigma = $ A + B$T^{1/3}$ at the transition, as their data showed. Our system behaves analogously, but with a power law exponent of $\sim 1/5$ at the transition and then an exponent of $\sim 1/4$, $\sim 2/5$ and $\sim 1/2^1$ as the system is moved away from the MIT. Evidently our system behaves 'normally' slightly away from the MIT where there is a $T^{1/2}$ power law and ES-VRH; it is only at, or very close to, the MIT that the unusual critical exponents are observed. Further samples near the MIT will be needed before these results may be considered conclusive. The small negative σ_0 correction in the orange and red fits is unphysical, but is needed for an accurate fit.

In contrast to the previous section where the critical scaling curve was limited to the insulating branch figure 2.9B shows both sides of the MIT can be described by equation 2.1 using our σ vs T data from 50 mK to 180 K (when the phonon-scattering begins to dominate). Most MITs are only seen at cryogenic temperatures, so it is intriguing that we are able to see evidence of a quantum phase transition at temperatures as high as 180 K. However, since the MIT in NC networks is governed not by the Mott critical density but by that of equation 2.10, n_c is several orders of magnitude higher than in traditional MIT systems. The 3D free electron Fermi temperature for these ZnO NC networks ranges from $\sim$1000-$\sim$2000 K compared to $\sim$10 K for a typical metal allowing for scaling at comparatively high temperatures [143].

Using $t = n\rho^3$, $(n\rho^3)_c = 0.71$, and y = 0.16 $\pm$ 0.2 (by testing a range of values), the data collapses onto the two branches of the critical scaling curve given by equation 2.1. The distance from the critical point, $\Delta n\rho^3$, varies from 0.2 to 0.8 and the ratio $\Delta n\rho^3/(n\rho^3)_c$ varies from 0.3 to 1.1. Expressing y in terms of critical exponents, y = $1/\nu z$ where ν is the critical exponent of the diverging length scales ($\xi \propto (\Delta n\rho^3)^{-\nu}$) and z that of diverging time scales ($\tau \propto \xi^z$). The critical conductivity at the transition, $\sigma_c \propto T^{0.19}$,

---

[1] The appearance of these fractions is intriguing but the cause is unknown. Possibly it is just a coincidence.

indicates the temperature exponent $x = \mu/\nu z = 0.19$, where μ is the conductivity exponent $(\sigma(T \to 0) \propto (\Delta n\rho^3)^\mu)$. Our results of $x = 0.19$ and $y = 0.16 \pm 0.2$ yield $\mu = 1.2 \pm 0.2$. The two finite σ_0 values from the fits to the blue and purple curves allow us to experimentally measure the critical conductivity exponent μ by plotting $\log(\sigma_0)$ vs $\log(\Delta n\rho^3)$. Doing so yields $\mu = 1.47$ (there are no error bars because there are only two data points), higher than predicted from the scaling data. However, there are only two σ_0 values to fit, only the purple curve is truly independent of temperature and 50 mK is not 0 K so for now we treat $\mu = 1.2 \pm 0.2$ as more reliable. Rigorous critical scaling analysis would require much more metallic samples and possibly even lower temperatures [68, 144].

Lastly, $y = 0.16$ implies $\nu z = 6.3 \pm 0.8$, whereas in most MITs $\nu z \leq 3$. As $\mu = 1.2 \pm 0.2$ is close to typical values of μ, the small critical temperature exponent $x = 0.19$ can be related back to the high measured value of νz. The high x values measured in the Mott-Hubbard systems mentioned previously were also found to be due to high νz values, with $\nu z \approx 5$ [131] and $\nu z \approx 6$ [130]. Further experiments will need to be done on the MIT in NC networks before this behavior can be considered universal, and then theory will be needed to explain these novel results.

2.3.2 Relating electron density measured from Hall and LSPR

We now turn to another interesting question that to date has not been studied in NC networks, namely the relationship between the electron density measured by Hall effect (n_{Hall}) and that measured by the LSPR absorption feature (n_{LSPR}). In section 2.2 n_{LSPR} was used throughout the analysis of the critical scaling of σ vs $n\rho^3$ as the Hall effect through percolating insulating networks is difficult to interpret. In this section n_{Hall} was used throughout the analysis as the measured n values agreed well with the 300 K conductivity measurements.

To relate $(n\rho^3)_{Hall}$ to $(n\rho^3)_{LSPR}$ we look at the NIR absorption of ZnO samples analogous to those studied in transport measurements[2]. The results are shown in figure 2.10A and show a strong σ dependence on the intensity yet the blueshift of the

---

[2] The LSPR samples were deposited (and received IPL treatment) on NaCL substrates adjacent to the borosilicate substrates used for transport studies so that each film was the same to within minute fluctuations.

peak intensity shifts only slightly. This is contrary to most absorption models and cannot be explained by a diverging dielectric constant near the MIT [145] as samples far from the MIT exhibit similar behavior [146].
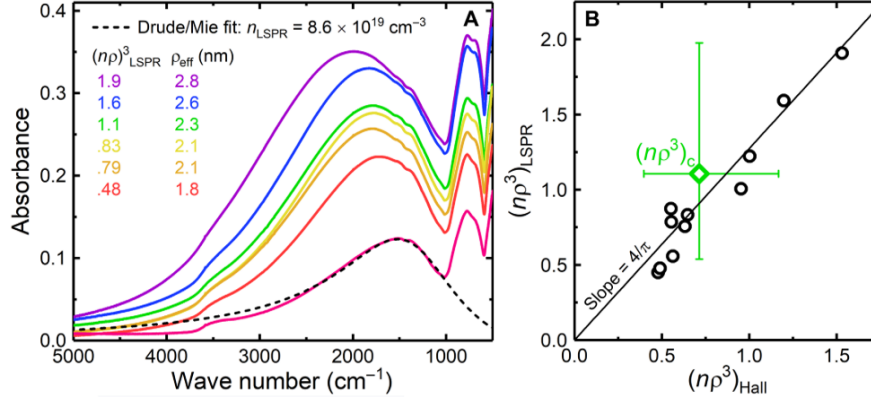
Figure 2.10: A) Select IR absorption spectra showing LSPR absorption. All samples correspond to those studied in figure 2.9A except for the magenta curve on the bottom which was acquired from a sample further from the MIT. B) Comparison of two estimates of $n\rho^3$ from LSPR and Hall measurements. $(n\rho^3)_{LSPR} = \mathrm{n}_{LSPR}\rho_{eff}^3$ and $(n\rho^3)_{Hall} = \mathrm{n}_{Hall}\rho^3$, where ρ^3 is determined by the ZnO lattice. The error bar on the critical data point represents an uncertainty in ρ of 0.5 nm.

Based off of work by Zandi *et al.* [147] and zum Felde *et al.* [148] we hypothesis that the lack of LSPR blueshift is due to depletion layers on the NC surfaces due to Fermi level pinning of surface states. Zandi *et al.* charged NCs electrochemically while monitoring the LSPR absorption feature. They found that the magnitude of the LSPR blue-shift decreases with both increasing NC size and electron density and attributed the increase in intensity to be due to a larger undepleted core volume while n stayed nearly constant. As our NCs are beyond the quantum confined regime (Bohr radius of ZnO is 2.34 nm vs 10 nm NC diameter) and extremely doped, and we know the vital role IPL plays in the trapping of charges on surface states (figure 2.3 and corresponding text), it is reasonable to expect our NCs also have depletion layers which are removed by IPL.

Previously the series of NC films in this study were considered to have fixed ρ while n is increased by photodoping. Now we propose an alternative explanation in which n is fixed but ρ changes with doping IPL flashes by removing depleted surface states
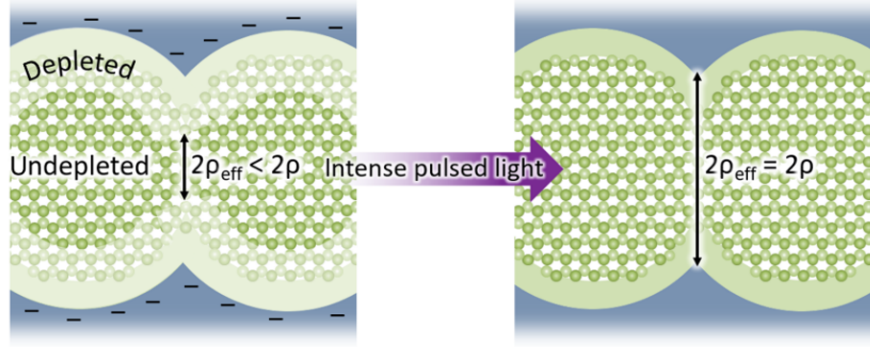
Figure 2.11: Schematic of the depletion layer due to filled surface states. The IPL serves to remove these surface states, increasing the undepleted core volume and hence the effective facet radius.

and promoting electrons to the conduction band, increasing the total number of free electrons N but keeping the electron density n fixed. A schematic of the concept is shown in figure 2.11 of a partially depleted NC and an undepleted NC. There is now an effective facet radius ρ_{eff} which increases from 0 nm for samples far on the insulating side to ρ for the most metallic sample (n is found to saturate around 1000 IPL flashes indicating a complete removal of surface traps and hence a fully undepleted core). To estimate ρ_{eff} from the LSPR features we ignore the slight blue shift with increasing intensity for simplicity and use the following series of assumptions:

1. ZnO NCs have a uniform 3D depletion layer at the ZnO/Al_2O_3 interface extending into the ZnO a width w so that $\rho_{eff} = \rho$ - w and the undepleted core volume has radius $r_{eff} = r$ - w.

2. The most conductive sample has $w = 0$.

3. Area under the LSPR feature is proportional to the number of free electrons N [149], which is in turn proportional to the undepleted volume [147].

Hence if a sample has half the LSPR area of the most conductive sample then $r_{eff} = (0.5)^{1/3}$ x 5.2 nm = 4.1 nm, $w = 5.2$ nm - 4.1 nm = 1.1 nm and $\rho_{eff} = 2.8$ nm - 1.1 nm = 1.7 nm. A sample far from the MIT, in which $\rho_{eff} = 0$, is used as a baseline measurement of the area under the LSPR feature and is the magenta curve in figure 2.10A. The curve

is fit with Mie theory and does not take into account inter-NC coupling, which we use justifiably for this insulating sample, and yields the electron density n_{LSPR}. From this, the aforementioned model is used to estimate ρ_{eff} for the samples used to cross the MIT. The results are plotted vs $(n\rho^3)_{Hall}$ in figure 2.10B, and show that $(n\rho^3)_{LSPR}$ is typically larger than $(n\rho^3)_{Hall}$ by a constant amount. Excellent agreement can be obtained by applying a correction factor of $4/\pi$, which is the predicted ratio of n within an NC to the measured n_{Hall} for NCs in a cubically packed network [150]. In our situation they are instead related by $n\rho^3$, where $(n\rho^3)_{Hall}$ corresponds to the network and $(n\rho^3)_{LSPR}$ to a single NC. In summary, n_{LSPR} serves as a measure of the *local* electron density while n_{Hall} serves as a measure of the *global* electron density and their ratios scale as expected for a granular system [150].

Lastly, we observed the MIT at an $n\rho^3$ value of 0.71, about a factor of 2 higher than the theoretical value $n\rho^3 \propto 0.3$. This is not surprising, as the theory was developed for 2 NCs in contact whereas in our networks there are approximately 10 trillion NCs![3] Fluctuations in NC size, facet size, porosity, film thickness, NC shape etc. all influence the transition and will increase the predicted critical value of $n\rho^3$.

In the previous section, when we failed to cross the MIT without the addition of ZnO via ALD, we found a maximum $n\rho^3$ of 2.6. This may be attributed to our use of n_{LSPR} in that section, which we have shown leads to a higher electron density than that from Hall measurements, and also to the large uncertainty in ρ. Figure 2.10C indicates that our separate measurements of n agree nicely and that it is ρ which limits our ability to accurately measure $n\rho^3$.

2.3.3 Methods

The ZnO synthesis, IPL and Al_2O_3 ALD methodology were all described in section 2.2. ZnO ALD was done with a Cambridge Nanotech/Ultratech Savannah S200 system with precursors of diethylzinc and water at 180°C. The fully dense polycrystalline ZnO thin film was grown on the same ALD system using 1000 cycles to produce a film ~170 nm thick.

The films were found to degrade at a rate of ~1% per day in an ambient atmosphere

---

[3] To give an idea of the scale of this number there are ~0.3 trillion stars in the Milky Way [151], ~3 trillion trees on earth [152] and ~20 trillion red blood cells in an adult human [153]!

so the films were kept in an inert N2 glovebox to prevent degradation. Some of the high T (300 K - 2 K) measurements were done months before the low T (1 K - 50 mK) measurements and the minimal σ difference at 2 K indicates these films are stable over at least several months in the glovebox, likely much longer. Degraded films could be re-flashed with IPL to recover their optimal conductivies, evidence that the degradation is due to readsorption of surface species onto the NC surfaces due to the hydroxyl groups diffusing through the alumina.

Structural characterization: XRD patterns were done using the method described previously, as were the ellipsometric measurements which yielded film thickness L, porosity and facet size. Intrasample deviations of L was 30 nm, diameter d $\sim$2 nm, ϕ 0.02 and ρ 0.3 nm. Intersample deviations of the average parameters were 0.1 nm for ρ, 20 nm for L, 0.02 for ϕ and 0.2 nm for d.

Microscopy: Figures 2.7B,C and 2.8 were done using lamellae prepared on an FEI Helios NanoLab dual-beam focused ion beam and examined using TEM and EDX spectroscopy. An aberration-corrected FEI Titan G2 60 - 300 STEM equipped with a Super-X EDX spectrometer was operated at 60 kV with a convergence semiangle of 25 mrad and a beam current of 120 pA. Spatially resolved STEM-EDX maps were collected with 1024 pixels by 1024 pixels over 450 nm by 450 nm areas, a dwell time of 4 ms/pixel, an acquisition time of 10 min, and drift correction after every frame. The Zn, Al, O, Si, and C K-edges were background-subtracted and integrated, producing spectral images. A three-pixel Gaussian blur was applied to the final spectral images to reduce noise and aid in visualization.

Transport measurements: Deposition of contacts and high temperature conductivity measurements were described in section 2.2. Data below 2 K was acquired using an Oxford Triton 200 dilution refrigerator. T was held at discrete values for 1 to 2 min to ensure stabilization. Conductivity measurements were performed in either DC or quasi-DC mode (13-Hz AC with a time constant of 1 s) using a custom IVVI rack with a high-precision current source, a Keithley 2000 voltmeter, and a Stanford Research Systems SR830 lock-in amplifier. IV scans were performed at the lowest T and excitation currents in the linear IV regime were selected for T scans. Comparison of DC and quasi-DC measurements at the lowest T confirmed that the two excitation modes yield the same σ.

Hall measurements were done at 300 K with a current of 10 µA while B was swept from -10 to 10 Tesla. Film thickness of 300 nm were used for all samples. Uncertainty in n was dominated by uncertainty in L. As L uncertainty was $\pm$ 30 nm, the corresponding uncertainty on n is thus $\sim$10%.

IR absorption feature: The LSPR spectra were measured in an inert atmosphere using a Bruker ALPHA spectrometer in transmission mode. The LSPR area was calculated by integrating the blue-half of the absorption feature in order to avoid the Al_2O_3 absorption feature at 800 cm^{-1}.

2.3.4 Acknowledgements

This work was published in August 2019 in *Science Advances* under the title "Metal-insulator transition in a semiconductor nanocrystal network" [154]. The American Association for the Advancement of Science grants the permission of the reuse of figures in dissertations, which we have utilized extensively in this section. This section has been rewritten for this thesis so is not a direct use of the full-text.

2.4   Conclusions

In this chapter we have demonstrated an MIT in a semiconductor nanocrystal network. Through a sophisticated series of steps consisting of plasma synthesis, IPL, ZnO ALD, Al_2O_3, and more IPL we have shown that the temperature dependent conductivity of the network can be tuned from Efros-Shklovskii variable-range hopping to metallic-like conduction. At the transition an unusual power law conductivity of the form $\sigma_c \propto T^{0.19}$ was observed as well as a correspondingly high νz value of 6.3 ± 0.8. Both sides of the transition collapsed onto the critical scaling curve equation 2.1 indicating quantum phase transition is observed.

As this is the first known thorough confirmation that an MIT is possible in an NC network there are numerous questions remaining regarding the MIT in an NC network. First, here the MIT was only crossed upon additional deposition of ZnO via ALD. While we are confident this is still an 'NC network' in nature it would be more aesthetically pleasing to be able to observe an MIT without needing to artificially increase ρ. We found that σ does not increase further with additional IPL flashes, so in order to increase $n\rho^3$ further either ρ could be increased by using larger NCs, or n increased by using a semiconductor with a higher intrinsic carrier density.

Numerous other relevant variables should also be studied in their effect on the MIT; in addition to NC size, the network porosity, NC size dispersion, film thickness, and lattice packing should all be related to the simplistic 2-NC $n\rho^3$ MIT criterion. The creation of NC superlattices is an extremely active area of current research where in sharp contrast to our disordered network of plasma-synthesized impact-deposited NC network tens of microns sized organized lattices of NCs can be created [155–161]. However, in 2D epitaxially connected superlattices disorder is *still* found to be strong enough to prohibit electron delocalization [107]. While the MIT in 2D systems has been shown to

exist in recent years in thin films [162, 163], for now 2D NC superlattices are still too disordered. There has been recent progress on the formation and transport studies of 3D superlattices [164] which show great promise for carrier delocalization.

The NCs in this study were too large to exhibit quantum confinement effects. Utilizing the properties of quantum confinement with high conductivity films has important applications for LEDs, photodetectors and solar cells. A recent paper [109] showed evidence of a Coulomb blockade in the drain-source current of an ensemble QD transistor at 77 K and bandlike transport behavior at $T > \sim 75$ K. While their films showed insulating behavior at cryogenic temperatures their high T measurements showing the filling of 1S and 1P states in the IV curve indicate a huge advancement in the utility of confined QDs as high conductors.

Our critical $n\rho^3$ of 0.71 was about a factor of 2 higher than the predicted value of 0.3. Future studies should also test this theory. Superlattices in particular have minimal disorder; perhaps the transition there will occur at $n\rho^3 = 0.3g$. Our results of $(n\rho^3)_{Hall}$ vs $(n\rho^3)_{LSPR}$ were found to agree well with the theory for transport in granular systems. This indicates our measurements of n are accurate and it is the measurement of ρ which limits our accuracy of experimentally determining $n\rho^3$. Our measurements of ρ were indirect through ellipsometry and a geometric model of depletion layer. Future studies of charge transport might measure ρ directly either through state-of-the-art transmission electron microscopy or electron topography. Recent TEM images of a PbSe NC superlattice [107] has shown the atomic crystal lattice structure is uniform between two NCs connected through a small facet making direct measurements of ρ possible and showing great promise for accurate measurements of ρ in the near future coupled together with Hall, LSPR and σ vs T measurements.

Our critical conductivity close to the form $\sigma_c \propto T^{1/5}$ most certainly deserves more study, which hopefully future observations of the MIT in NC networks will address. Whether it is universal to NC networks, a byproduct of the plasma synthesis (agglomerates are thought to form in-situ during the aerosol phase), or due to some other relevant variable such as those mentioned above is an interesting question both experimentally and theoretically.

Crossing the MIT in an NC network is an important demonstration for the utility of NCs in practical devices. Combining near bulk-like conductivity with the advantages

of nano-engineering may be exploited for use in solar cells, field-effect transistors, thermoelectric generators, electrochromic windows, wearable electronics and optoelectronic devices [165]. We have demonstrated the feasibility of metallic transport in a disordered NC system which may be extended via incorporation into the previously mentioned devices or be used as a starting point for additional fundamental studies of transport in NC systems.

To conclude, let us revisit a *Science Perspectives* article from 1996 on the metal-insulator transition in correlated disordered systems [166] which commented on the high νz value in the $NiS_{2-x}Se_x$ films mentioned previously [131]:

> "However, this experiment raises again many old questions... Why are the critical indices in this system so different from what is observed in doped semiconductors and amorphous alloys? Is the present universality class associated with the unusual strength of the electron-electron correlations that are present in this material? ... Much more work needs to be done to unravel the metal-insulator transition puzzle."

Evidently the past 20-odd years has not brought forth the answers but perhaps the addition of NC networks to this class of unusual materials will shed some fresh light onto an old problem. The metal-insulator transition is approaching its 90th year of rigorous study [72] implying $\sim$5 generations of physicists have worked on the problem; hopefully the next 90 years will result as much profound insight into the correlations governing transport in semiconductors as the past 90 years have.

Chapter 3

Synthesis and Electronic States of CdSe/HgS/CdS Quantum Dots

In this chapter we will study the synthesis, electronic states and optical properties of novel CdSe/HgS/CdS colloidal quantum dots. Our shell synthesis combines the techniques of colloidal atomic layer deposition and successive ion layer adsorption and reaction. This enables atomic-level HgS growth at the individual monolayer (ML) level. The emission is tunable from ~600 nm for CdSe/CdS QDs out to ~1200 nm for CdSe/HgS/CdS QDs with a 4 ML HgS shell. The emission spectra for various HgS thicknesses is almost non-overlapping between an 'N' ML HgS shell and an 'N±1' ML shell, a feature only possible due to the discreteness of the lattice sizes in the synthesis. We begin with a brief overview of CdSe/CdS QDs followed by an in depth discussion of the electronic properties of CdSe/HgS/CdS QDs studied numerically via the effective mass approximation. After familiarizing ourselves with this material we explore the synthesis and steady-state and time-resolved optical properties of this system. The final two chapters of this thesis will concern multi-exciton dynamics in these CdSe/HgS/CdS QDs and their potential use as near infrared single photon emitters.

3.1 Introduction

In the previous chapter we extensively used electrical measurements to study electron transport in ZnO NC networks. While electrical transport studies reveal lots of information about the states of a system there are many drawbacks. Primarily, the QDs must be deposited as a film making it impossible to study the properties of non-interacting QDs, and during the deposition process the QDs are likely exposed to air, potentially degrading the dots. Additionally, in disordered QD films many of the interesting electronic states are smoothed out through the macroscopic nature of charge transport, obscuring the delicate quantized states in QDs.

To this end, optical spectroscopy is a vital tool for studying the properties of QDs. In direct-gap semiconductors photons with energy greater than the bandgap E_G are absorbed by the material promoting an electron from the valence band into the conduction band of the material. As shown in figure 1.1, once the size of a semiconductor is comparable to or smaller than the exciton Bohr radius the quantum size effect leads to a blue shift in absorption levels due to the discrete states of the system. Hence, simple steady-state measurements like absorption and emission spectra provide an enormous amount of information about the quality and properties of any given QD system. Optical measurements are 'non-contact' in contrast to electrical measurements which makes them less invasive and measurements can be done while the QDs are in solution so that non-interacting studies can be done.

While steady-state measurements provide information on the electronic states of the system, they do not help with understanding the dynamics of the system. Time-resolved spectroscopy is used to evaluate temporally the absorption and photoluminescence of samples. In time-resolved photoluminescence (TRPL) measurements, a sample is excited by train of ultra-short laser pulses and the emission is put through a monochromator and then coupled into a single-photon counting (SPC) detector. Two different times are tagged by the system, a 'trigger' which denotes the $t = 0$ of the system and the time the photon reaches the detector. Collecting numerous decay events allows one to create a histogram of electron-hole recombination processes. Time resolution of TRPL can be as low as a few ps [167] with state-of-the-art SPC detectors.

For events faster than electron-hole recombination such as band-edge electron/hole

relaxation or separation a different technique must be used, the most popular of which is transient absorption spectroscopy (TA). TA allows ultra-fast dynamics to be resolved, such as 1P-1S relaxation [168] or electron/hole trapping [169]. TA is a pump-probe experiment where first the system is 'pumped' with a femtosecond laser which excites the sample and then 'probed' by white light generated from a sapphire, YAG or CaF_2 crystal. The probe path length is varied by a micrometer stage, and changes in the absorption of the white light by the sample are monitored as a function of the delay between the pump and probe allowing charge relaxation to be quantified by measuring intensity and spectral features across the absorption spectrum. The resolution is limited only by the pulse-width of the laser as state-of-the-art motor delay states can be controlled at the sub micron level (1 fs = 300 nm at the speed of light). Hence, relaxation processes at the sub-100 fs level can be extracted [170].

3.1.1   The Prototypical Quantum Dot: CdSe/CdS

By far the most studied and well understood QDs are those of CdSe [14,171,172], which have near unity QY, ideal color purity and monoexponential decay dynamics, indicative of only one relaxation channel. However, CdSe QDs are very unstable photochemically, even under ambient conditions [173]. To remedy this, often CdSe QDs are coated with a wide bandgap CdS shell. The CdS conduction band minimum is ∼0.1 eV higher than CdSe while the CdS valence band maximum is ∼0.6 eV below that of CdSe. This leads to confinement of the electron and hole in the core, while also protected the emissive core layer from surface defects or other traps [173–176]. A thicker shell can serve to prevent the QD from blinking, useful for LEDs and single QD applications [177–181].

CdSe-based QDs have 30 years of experimental and theoretical understanding behind them [182], and continue to be a very active research field today [173,183–188]. However, their emission maximum is limited to ∼580 nm to ∼680 nm making NIR applications impossible. Here we will work with CdSe/HgS/CdS QDs where the HgS interlayer thickness is controllable at the single ML level. It will be shown that this leads to discrete jumps in the emission spectrum for different thicknesses of HgS and the emission energy can be decreased to below 1 eV.

3.2 Electronic States of CdSe/HgS/CdS Quantum Dots

Prior to diving into the experimental results we will look at the electronic states of CdSe/HgS/CdS via the effective mass approximation [16]. This will allow us to understand the material at hand and this section will be referred to repeatedly throughout the rest of this chapter and the following ones.

HgS is a member of the mercury chalcogenides family along with HgSe and HgTe. Three forms of HgS are found in nature; the most common is α-HgS, also known as red cinnabar or vermilion, which has a trigonal lattice and a bandgap of 2.1 eV [121]. For centuries α-HgS was used by painters for the color red via the mineral vermilion,[1] long before the hazardous health effects of Hg were known. The second most common form and that to be focused on primarily in this thesis is β-HgS, or metacinnabar, which has a zinc-blende crystal structure and a bandgap of -0.5 eV to 0.5 eV [121] (see below for explanation of this range). Lastly there is hypercinnabar, in the wurtzite crystal structure, which is formed at higher temperatures than the previous to forms of HgS. Hypercinnabar is intimately related to β-HgS as well will see below. For the remainder of this section we will focus on β-HgS as that is primarily where our interests lie though the results here should be directly transferable to wurtzite HgS.

For many years all three members of the mercury chalcongenides were thought to belong to the group of materials which have inverted band structure, or 'zero' or 'negative' band-gap materials, in which the bottom of the conduction band is lower than the top of the valence band. However, experiments on HgS found a wide variety of bandgap values, both positive and negative, perplexing physicists for decades. Recent theoretical work by Cardona *et al.* found that spin-orbit coupling is negative in HgS whereas in HgSe and HgTe it is positive; this leads to HgS being a semiconductor with a bandgap of several hundred meV while HgTe and HgSe are semi-metals [189, 190].

Here HgS shells are grown on CdSe cores with atomic-level precision before coating with a final CdS shell to protect the QDs. Similar 'spherical quantum wells' have been created before in CdS/HgS/CdS heterostructures and other materials [191–198]. However, these QDs were synthesized from a H_2O based colloidal synthesis which severely limited their quality as the QY was limited to only 3-5%. Here we report the synthesis

---

[1] For instance, see *Assumption of the Virgin* by Titian (1516-1518) or the murals in the *Villa of the Mysteries* in Pompeii.
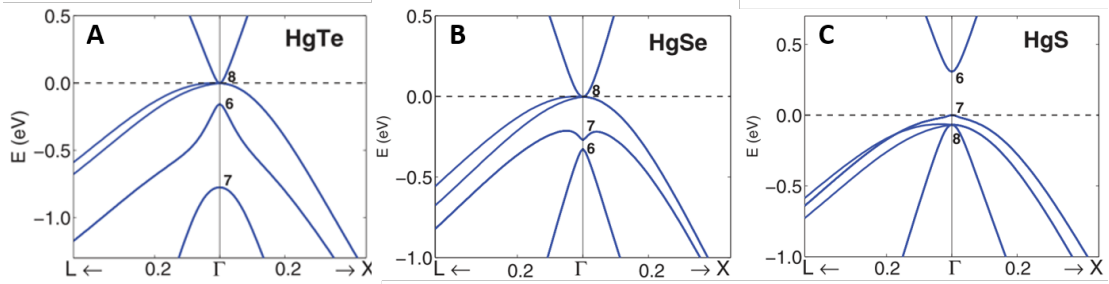
Figure 3.1: Calculated band structures of the mercury chalcongenides near the Γ point. A) HgTe and B) HgSe are semimetals, while C) HgS is a narrow gap semiconductor. Figures reproduced with permission from reference [190].

of high quality CdSe/HgS/CdS QDs with QY up to 60%+, far higher than is obtainable in CdS/HgS/CdS heterostructures. The synthesis is described in detail in the next section of this chapter.

As previously stated the CdSe conduction band minimum is 0.1 eV lower than that of CdS [18]. Based on calculations and experiments in the literature [191, 199] we take the bandgap of HgS to be 0.5 eV and the conduction band minimum to lie 1.35 eV below that of CdS [195, 200], so that it is 1.25 eV below that of CdSe (others use CdS conduction minimum 1.3 eV above HgS [191]; we find better matching to our 1S transition energies with a 1.35 eV offset and the 50 meV energy offset will not effect main results). The valence band maximum offset of CdSe/HgS is nearly zero at just .01 eV while the CdS valence maximum lies ∼0.6 eV below that of the core materials. As shown in figure 3.2B, this leads to a spherical quantum well in the HgS interlayer for the 1S electrons while holes are delocalized throughout the CdSe/HgS layer.

To calculate electronic states in CdSe/HgS/CdS QDs we implement an effective-mass formalism [201] using a mesh-based method of solving the radial Shrödinger equation as described in [23, 202]. Due to the strong confinement of this system the Coulomb interaction between charges is negligible so is not included in the calculations. We use a bandgap of 1.74 eV, 0.5 eV and 2.5 eV for CdSe, HgS and CdS respectively. The electron (hole) masses in units of the free electron mass m_0 are 0.16 (0.45) for CdSe, 0.036 (0.044) for HgS and 0.2 (0.7) for CdS. Lastly, the lattice constants are 6.08 Å for CdSe, 5.85 Å for HgS, and 5.82 Å for CdS [121]. The minimal lattice mismatches

allow for the growth of high-quality QDs even with single ML shell layers. Air is used as the outermost layer, with m = m$_0$, in all the calculations in order to truncate the wave functions (see figure 3.3A). The zero energy level is taken to be the bottom of the conduction band of HgS.
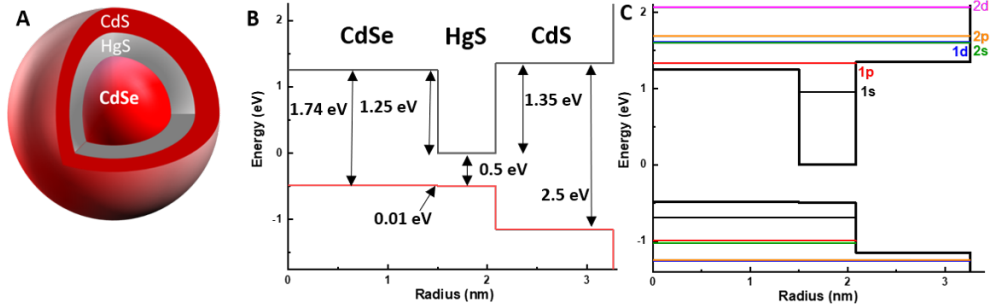
Figure 3.2: A) Schematic of the spherical quantum well. B) Schematic of the heterostructure band profiles with the parameters used in the calculations listed. C) Calculated electron/hole energy levels for a 1.50 nm radius CdSe core, 1 ML HgS, and 1.2 nm CdS shell. The 1S electron state is localized in the HgS well while the 1Pe state is above the CdSe conduction band minimum. All hole states are delocalized leading to this being a quasi-type-II structure.

Results of the six lowest electron and hole states is superimposed onto the energy level schematic in figure 3.2C using a 1.50 nm radius CdSe core, a 1 ML HgS shell, and a 1.2 nm CdS shell. The hole states are close together as is typical in semiconductors which have a much greater effective hole mass than electron mass, and are delocalized throughout the CdSe/HgS layer. The 1S electron state (1Se) is localized inside the HgS well lying 300 meV below the CdSe conduction band minimum. The 1Pe state lies 380 meV above the 1Se state and 80 meV above the CdSe conduction band. The 1Pe state is only 16 meV below the CdS conduction band minimum so may be treated as delocalized across the entire QD. The higher level states exist throughout the CdSe/HgS/CdS heterostructure as well, and above them exist more discrete states and a transition to a continuum of higher energy electronic states.

The 1Se, 1Sh and 1Pe radial wavefunctions, R$_{10}$(r) and R$_{11}$(r), are plotted in figure 3.3A for the 1 ML HgS sample. The cusps are non-physical and come from the discrete jump in effective masses at interfaces when using the effective mass formalism. Clear localization of the electron in the HgS layer is seen, while the hole is delocalized

throughout the structure. Doing this for 1-4 ML of HgS and calculating the square of the electron-hole wavefunction via equation 3.2 shows that the overlap increases with increasing HgS thickness (figure 3.3B). This can be understood intuitively as with thicker HgS widths the electrons move deeper into the well (becoming more localized) while holes remain delocalized. Furthermore as HgS width is increased the CdSe/HgS volume fraction decreases indicating a higher probability of finding a hole in the HgS layer and a correspondingly larger overlap integral.
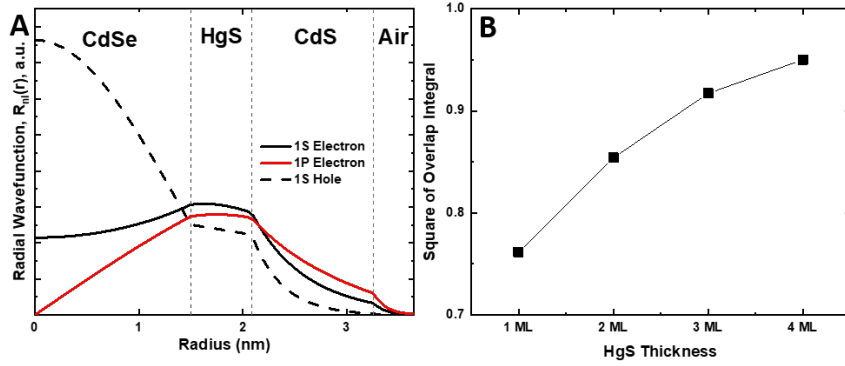
Figure 3.3: A) Radial 1Se, 1Sh and 1Pe wavefunctions for the 1 ML HgS sample. B) Square of the overlap integral for the 4 different HgS thicknesses.

In figures 3.4A,B the electronic (solid lines) and hole (dashed lines) energies are plotted as a function of HgS thickness with a fixed 1.50 nm radius core (figure A) and variable CdSe core radius with a 1 ML HgS shell (figure B). As the HgS interlayer thickness increases the hole states remain largely unchanged because the holes are delocalized throughout the CdSe/HgS heterostructure and therefore less susceptible to increases in the HgS thickness. On the contrary, as we increase the thickness of the HgS layer the electronic states move further and further into the well due to the decreasing quantum confinement in the HgS interlayer (figure 3.4A). This effect is most prominently seen in the lower energy 1Se and 1Pe states while the delocalized higher energy states are less susceptible to changes in the HgS interlayer thickness. The horizontal grey dashed line at 1.25 eV denotes the CdSe conduction band minimum while the vertical grey lines denote integer MLs of HgS. Previous work on CdS/HgS/CdS QDs showed that partial ML growth still resulted in shifts in the absorption/emission spectrum, so regions between

the vertical lines are in principle obtainable although this has not yet been explored in CdSe/HgS/CdS QDs [193].

For all HgS thicknesses (we use 3 Å as the minimum thickness which is $\approx 1/2$ ML) the 1S state is localized in the HgS core. Between 1 and 2 MLs of HgS the 1Pe state also drops into the well. A further increase of the HgS layer serves to push the 1Se and 1Pe states further into the well and the energy between them changes from 380 meV at very small HgS widths to $\sim$300 meV at larger shell thicknesses. The 1De state drops into the HgS well between 3 and 4 MLs of HgS located $\sim$500 meV above the 1Pe state while the remaining states are still above the CdSe and CdS conduction minima.
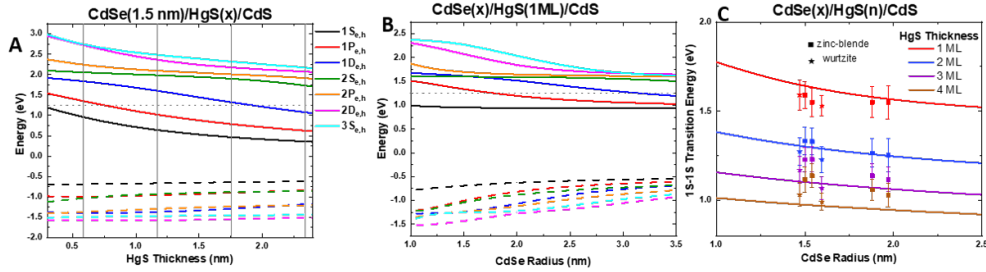
Figure 3.4: A) Electron (solid) and hole (dashed) energy levels for a fixed CdSe core and CdS shell while the HgS layer is continuously increased. The dashed line at 1.25 eV denotes the CdSe conduction band minimum and the vertical grey lines denote integer multiples of the HgS lattice constant (0.585 nm). B) Variable CdSe core radius while the HgS and CdS layers are fixed at 1 ML and 1.2 nm, respectively. The horizontal dashed line again denotes CdSe conduction band minimum. C) 1Se-1Sh transition energies of CdSe/HgS(n)/CdS(2) QDs with n an integer between 1-4. Solid lines are calculated data points are PL emission peaks from experiment. Square symbols denote zinc-blende crystal structure samples while stars represent wurtzite. The error bars represent the full-width at half-maximum of the PL spectra.

In figure 3.4B the CdSe radius is increased while the HgS layer is fixed at 1 ML. Here large changes in the hole energies is seen for small CdSe radii when the CdSe/HgS layer is in the strong confinement regime. Around 2.5 nm CdSe radius the 1Sh state becomes relatively insensitive to the core thickness but the other states are still moving up in the valence band slightly. The 1Ph state lies $\sim$25 meV below the 1Sh state. The 1Se state is largely unchanged by any variations in the CdSe radius as the 1Se state is localized in the HgS layer regardless of CdSe radius (horizontal dashed line denotes

conduction band minimum for CdSe) and thus impervious to changes in the CdSe or CdS layers. The higher order electronic states are more sensitive to to the CdSe radius with the 1Pe then 1De dropping into the HgS layer at CdSe radii of ∼1.75 nm and ∼3 nm, respectively.

Changing the CdS layer thickness does not effect the electron and hole energy levels by more than ∼1 meV as the 1S electrons and holes are localized in the CdSe/HgS layers. However, CdS shell thickness has very important contributions to surface passivation and the QY of the samples as will be discussed at length later.

The 1Se-1Sh transition energies are plotted for 1-4 ML HgS as a function of CdSe radius in figure 3.4C. The data points represent the PL emission peaks from experiments with various CdSe core and HgS ML thicknesses. The CdS outer shell thickness is 2 ML for all samples in 3.4C. The error bars serve to denote the full-width at half-maximum (FWHM) of the emission peaks due to size dispersion of the CdSe core. Thus far we have limited ourselves to discrete values of the HgS ML thickness but it is possible to grow fractional MLs of HgS which should extend the flexibility of emission energies even further [193].

CdSe/CdS QD emission (not shown) covers most of the visible spectrum but none of the NIR. Adding just a 1 ML HgS shell between the CdSe/CdS layers extends the transition energy out to the 700-850 nm range with additional HgS MLs continuing to decrease the transition energy out to below 1 eV. Such flexibility bodes very well for the potential applications of CdSe/HgS/CdS QDs as NIR emitters. Here we only examine 1-4 MLs of HgS but thicker HgS shells can in principle be grown leading to a further red-shift in transition energy out to more than 2 microns towards the HgS bulk bandgap of 0.5 eV. It will be shown in the next section that we are capable of growing CdSe/HgS/CdS QDs with up to 6 MLs of HgS but QY for these samples is comparatively low compared to the 1-4 ML HgS samples.

3.3 Experimental Results

Having familiarized ourselves with the electronic properties of CdSe/HgS/CdS quantum dots we now turn towards the experimental realization of these novel materials and the optical characterization of them. We begin with an overview of the synthesis technique,

followed by an analysis of their steady-state absorption and PL spectra and conclude with a study of their PL dynamics.

Throughout this section and the following chapters both the HgS and CdS shell thicknesses will be changed repeatedly which could potentially get confusing. To hopefully clarify the results each sample will be referred to as CdSe/HgS(n)/CdS(x) where n denotes thickness of HgS layer in unit of MLs and x will denote the CdS shell thickness. The core radius is fixed for most of the measurements at 1.5 nm.

3.3.1 Synthesis of CdSe/HgS/CdS QDs

To extend the CdSe/CdS core-shell material into the NIR we combined two well-established synthetic techniques that allow us to grow HgS shells onto CdSe cores with atomic-level accuracy: colloidal atomic layer deposition (c-ALD) [203] and successive ion layer adsorption and reaction (SILAR) [204] (figure 3.5). These self-limiting half-reactions of S^{2-} (in the form of $(NH_4)S$ OLA) and cationic Hg^{2+} (in the form of $Hg(OA_c)_2OLA$) on the CdSe surface in a non-polar phase enables us to generate 'closed-shell' structures at room temperature. The colloidal stability of the growing heterostructures is maintained by co-ligation of the NC surfaces with aliphatic alkyl chains of oleylamine molecules [205].

Specifically, highly monodisperse CdSe cores with either zinc-blende (zb) or wurtzite (w) crystal structures are functionalized with sulfide ions using ligand-exchange reactions. Here, S^{2-} efficiently strips off the pristine ligands from the NC surface and forms 1/2 ML of the shell material. To form a complete ML of HgS Hg^{2+} ions are deposited onto CdSe/S^{2-} using the SILAR approach. In contrast to the S^{2-} layer grown via c-ALD where the excess precursors (NH_4S) can be removed under low pressure, here the amount of Hg^{2+} ions added must be carefully controlled. The high affinity and reactivity of mercury ions towards sulfide ions leads to fast surface reactions; a large excess of Hg^{2+} ions can trigger undesirable Hg^{2+} to Cd^{2+} cation exchange despite the 'protective' sulfide layer [191]. Additionally controlling the amount of Hg carefully minimizes waste, something that should be always be done with a Hg based material. The precise amount of Hg-based precursors was calculated from the ratio between the core and shell volumes and known parameters of bulk CdSe and HgS. The initial concentration of CdSe QDs was determined based on the sizing curve and size-dependent molar

extinction coefficients [206].
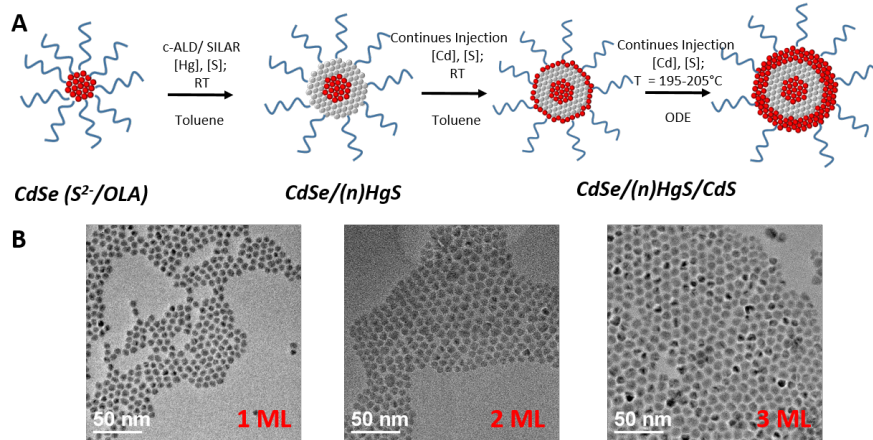
Figure 3.5: A) Schematic of the synthetic steps. Starting from a CdSe core Hg and S ions are added via SILAR and c-ALD respectively, while CdS outer shell is grown at $\sim$200 °C. RT stands for room temperature. B) TEM images of 1, 2 and 3 ML HgS of CdSe/HgS(n)/CdS(2) QDs.

By successively repeating S^{2-} and Hg^{2+} half-reactions we are able to strictly grow one ML of HgS at a time. After the formation of CdSe/HgS QDs with the desirable number of HgS MLs a protective outer CdS shell layer is deposited. CdS has almost a perfect lattice-match with HgS (differing by only $\sim$1/2%) guaranteeing efficient surface passivation. Two MLs of CdS shell were grown using the same approach as for the HgS layer deposition where S^{2-} and Cd^{2+} half-MLs were deposited using c-ALD and SILAR techniques, respectively. However Cd^{2+} cations do not show the same high affinity towards sulfide-terminated surfaces leading to the formation of homogeneously-nucleated CdS QDs along with CdSe/HgS(n)/CdS(2) QDs. Fortunately, the CdS QD sub-ensemble may be removed by means of size-selective precipitation using acetone as a non-solvent. The as-grown CdSe/HgS(n)/CdS(2) QDs do not show any emitting characteristics due to a high concentration of surface defects. To reduce the concentration of surface traps the QDs are thermally annealed at T = 200°C for 7 minutes in the presence of a small amount ($\sim$150 μL) of Cd- and S- precursors.

To grow thicker CdS shells the as-synthesized CdSe/HgS(n)/CdS(2) QDs are further heated to T = 220°C in the presence of Cd- and S- precursors. The amounts of the

precursors are calculated from the QD particle size and the desired final shell thickness. After the addition of the precursors is completed the temperature is lowered to 200°C and 1 mL of oleic acid is added. This reaction mixture is annealed for 30 min, leaving the final product. The high temperature treatment leads to the formation of highly crystalline QDs with impressive QYs, stability and symmetric and narrow PL linewidths.

Using this growth technique arbitrary complex sequences of different atomic layers can be grown around QD cores; for example CdSe cores could be coated in alternating HgS and CdS shells resulting in an 'onion' type QD structure with a series of HgS quantum wells. Alternatively, a variety of materials could replace the CdSe, HgS or CdS layers to synthesis a new nanomaterial with some desired property.

It took many years for CdS shell growth to be perfected on CdSe QDs. It is far from inconceivable that such advances may be made on these CdSe/HgS/CdS QDs in the future serving to maximize their potential as NIR emitters. Controlled doping, alloying or different temperature shell growths all might lead to more high-quality QDs with specific properties applicable for some desired purpose.
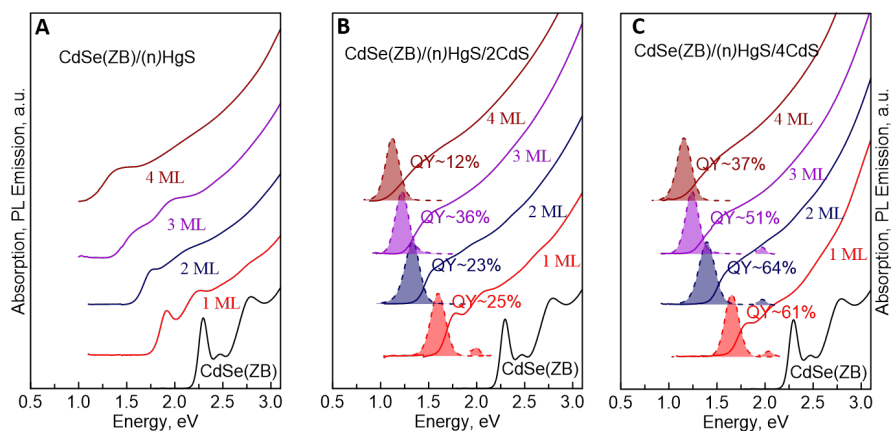
Figure 3.6: Absorption and emission of 3.8 nm zinc-blende CdSe cores coated with HgS and CdS. A) CdSe-zb QDs coated with n MLs of HgS. Clear absorption features can be seen. B) Coating in a 2 ML CdS shell and annealing results in emission. C) Absorption and emission of the 4 ML CdS shelled sample. The numbers in (B) and (C) indicate the QY.
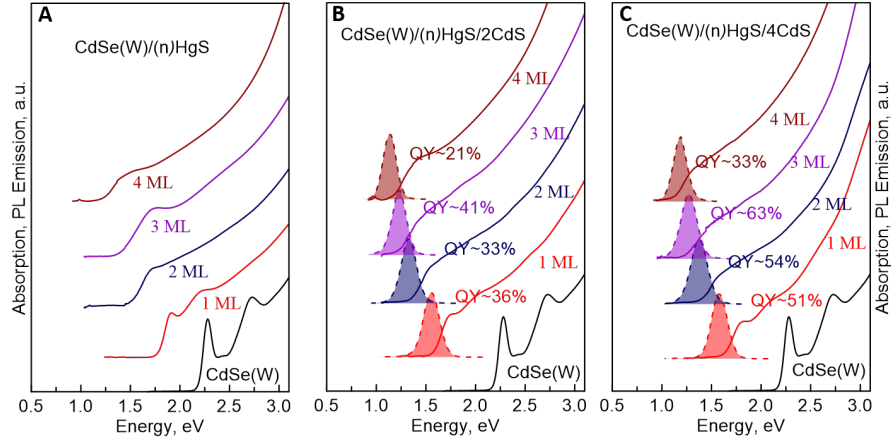
Figure 3.7: Absorption and emission of 3.2 nm wurtzite CdSe cores coated with HgS and CdS. A) CdSe-w QDs coated with n MLs of HgS. Clear absorption features can be seen. B) Coating in a 2 ML CdS shell and annealing results in emission. C) Absorption and emission of the 4 ML CdS shelled sample. The numbers in (B) and (C) indicate the QY.

3.3.2 Steady-State Optical Properties

The steady-state absorption, emission and QY are shown for 1-4 ML of HgS with 0, 2 and 4 ML of CdS on a 3.8 nm diameter CdSe-zb core (figure 3.6) and on a 3.2 nm CdSe-w core (figure 3.7). X-ray diffraction spectra (XRD), not shown, indicate that the HgS crystal structure follows the CdSe core crystal structure so the CdSe-zb core leads to βHgS, or metacinnabar, while the CdSe-w core leads to hypercinnabar, as discussed previously. Both of these materials have similar electronic properties, and indeed both of their PL peaks for various CdSe and HgS sizes nicely follow the EMA results in figure 3.4C. In figure A of both figures 3.6 and 3.7 CdSe/HgS(n) QDs show no emission but clear absorption features consistent with the quantum confinement of the CdSe core and the HgS interlayer, as in figure 1.1B. The progressive red-shift with increasing HgS thickness is consistent with a reduction in the quantum confinement as the HgS layer gets larger. Figures 3.6B and 3.7B show the CdSe/HgS(n) cores from figure A coated with 2 ML of CdS then thermally annealed. Now strong emission is observed near the absorption feature onset indicative of bandgap emission from the QD. PL emission maxima extend from 800 nm for the 1 ML HgS sample out to 1150 nm for the 4 ML HgS

sample. Figures 3.6C and 3.7C show the absorption and emission of the QDs coated with a 4 ML CdS shell. The PL peaks are nearly identical but the QY is enhanced by $\sim$50%. This can be attributed to improved passivation of trap states as will be discussed more in-depth later. The QY is greater than 50% for 1-3 ML HgS samples in both zb and w crystal structures, with the 4 ML HgS samples showing a slightly reduced QY of $\sim$35%. Such high QY in the NIR bodes well for the use of CdSe/HgS/CdS QDs in LEDs, lasers and as single photon emitters.

The full-width at half-maximum (FWHM) of the emission spectra is 205, 188, 162 and 141 meV for the zb crystal structure with 1-4 ML HgS and 2 ML CdS and 200, 185, 179 and 155 meV for the w crystal structure series. While far from the linewidth of $\sim$50 nm that state-of-the-art visible emitting QDs can achieve, these values are still quite remarkable for NIR-emitting QDs and without a graded core/shell interface. A later chapter will show that single QD emission spectra of the 1 ML HgS samples show linewidths of $\sim$80 meV, so the ensemble PL linewidths are comparatively narrow compared to the wide single QD linewidth. Hence size dispersion of the CdSe cores is not the only cause of the broad PL bandwidth, it is something intrinsic to the QDs themselves.

A natural question to consider is whether we are actually growing only 1 ML at a time or are a variety of ML thickness growing concurrently. Indeed, growing single ML on top of a QD is nearly impossible with most synthetic techniques and any sizable lattice mismatch will destroy any chance of having a smooth transition at the interface. Fortunately βHgS and HgS-w are very stable materials with similar properties, and both have a lattice mismatch with CdSe of merely $\sim$4%. To prove that only 1 ML is grown in each double 'half-reaction' we purposely grow 'messy' batches of QDs (did not wash between each half-reaction) and look at their emission spectra. As shown in figure 3.8, the 3 ML sample shows clear side peaks at the 2 ML and 1 ML emission energy, and the 2 ML sample shows a clear side peak at the 1 ML emission energy. The side peaks of the 'n' ML emission spectra match up perfectly with the emission peaks of the 'n - 1', 'n - 2', ... CdSe/HgS(n)/CdS QDs in a 'clean' synthesis, indication of a step-wise series of single ML growth. This analysis shows the strength of our self-limiting half-ML reactions via the c-ALD and SILAR steps. If the synthesis was not growing single MLs at at time instead of distinct peaks from each batch of QDs a broad

emission from a continuous distribution of HgS widths would be observed. As mentioned previously it was shown to be possible to grow fractional HgS MLs in CdS/HgS/CdS QD synthesis [193] but we have not examined that here as in each step the amount of Hg introduced is carefully controlled to account for exactly one ML of growth in each cycle. In these sub-ML fractions, Hg can effectively be treated as a dopant in the CdSe/CdS system; the abrupt shift in emission energy at only 5% of a ML indicates how efficiently Hg traps the electrons (and holes, in the case of CdS/HgS/CdS), something that will be explored in future studies.
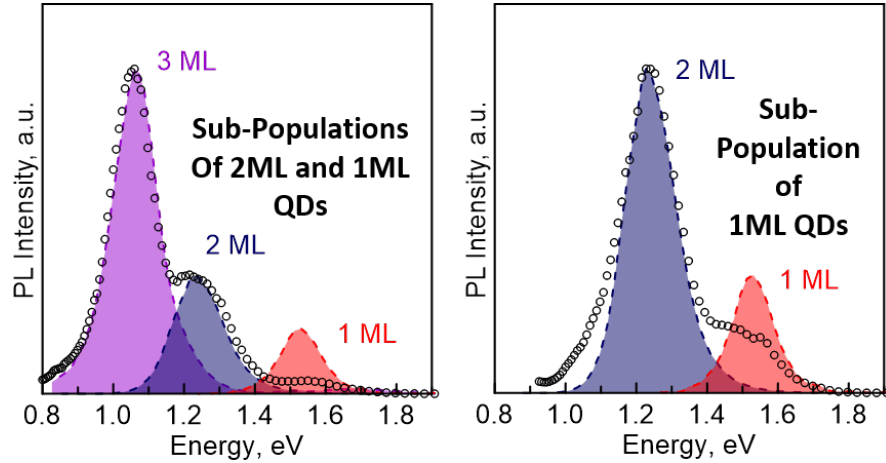
Figure 3.8: When the samples are not washed between each half-reaction the result is a sub-ensemble of different ML emission spectra. If the reactions were not self-limiting to 1 ML at a time then there would be a broad high energy emission peak from the sub-ensemble QDs rather than the distinct peaks observed.

Lastly, we directly compare the absorption and emission spectra of CdSe cores coated with 1 ML HgS and then coated with 2, 4, or 6 ML of CdS in the zb and w structures (figure 3.9). A small blue-shift is seen in the absorption and emission spectras with a thicker CdS shell which can be attributed to the higher temperatures required for thicker CdS shell growth. The CdS shell dependence on the emission maxima was calculated with the EMA to be negligible in the previous section, where changing CdS thickness resulted in minute ~1 meV changes in the 1S transition energy. Therefore something physically is changing in the system at these elevated temperatures. Whether this is partial cation exchange between Hg and Cd or a removal of emitting trap states is yet to

be determined, but whatever the cause the effect serves to create higher quality samples.

Strong increases in the absorption of thicker HgS samples is seen at higher energies, an indicator that the delocalized high energy electronic states play a role with the initial absorption process. This role will be examined more closely in the next chapter, where interesting high-fluence PL dynamics seem to arise from the absorption of these high energy photons.
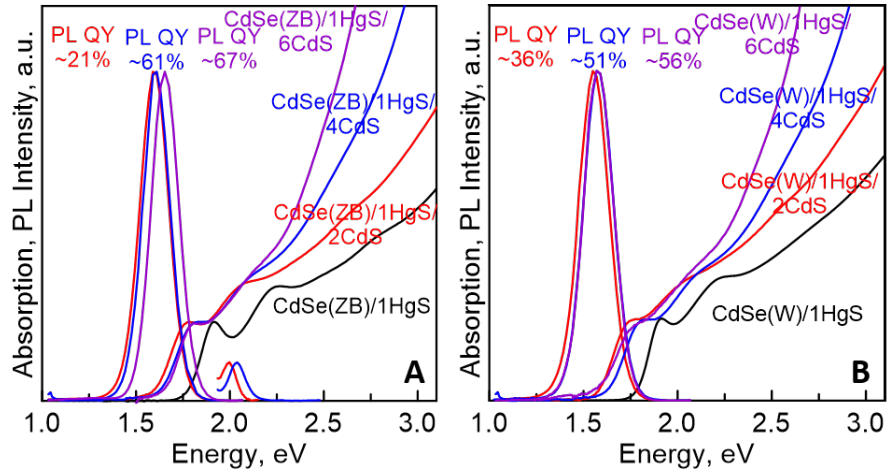
Figure 3.9: Comparison of absorption/emission spectra of CdSe/HgS(1)/CdS(x) QDs with $x = 2$ ML (red), 4 ML (blue) and 6 ML (purple) in A) zinc-blende crystal structure and B) wurtzite crystal structure.

Throughout experiments perfecting the synthesis parameters we also played with 5 and 6 ML HgS samples. These were shown to have greatly reduced QY and a strong fast component in the PL dynamics. Therefore we limited ourselves here to 1-4 ML of HgS due to their optical properties being optimized but in principle an arbitrary number of shell thickness could be grown. Future work will be needed in order to protect these delicate samples from degradation during the HgS and CdS shell growth where likely defects and surface traps dominate.

Going from 2 to 4 to 6 ML of CdS outer shell thickness resulted in consistent improvements in the QY of the QDs; this is in agreement with decades of work on CdSe/CdS QDs where thicker shell QDs prevent charging of the QDs and lead to higher QYs and monoexponential decays. CdS can be grown on CdSe out to 20 or more MLs in so called 'giant' QDs [177] or dot-in-bulk QDs [180] where the CdS shell is thick

enough that it is 'bulk-like'. Future work on extending the CdS thicknesses of these CdSe/HgS/CdS QDs will likely result in similar enhanced optical properties.

3.3.3   PL dynamics

Here we examine the low-fluence (average number of excitons per dot $\langle N \rangle << 1$) PL dynamics of CdSe/HgS(n)/CdS(x) QDs. The samples are excited with a 3.1 eV pulse with a temporal width of $\sim$200 fs. The emitted light is sent through a monochromater and then fiber-coupled to a superconducting single-nanowire photon detector (SNSPD) [207]. For these low-fluence measurements the beam size is kept large ($\sim$500 μm) and the power low. The repetition rate is kept at 250kHz.

PL dynamics for the 2 ML CdS shelled series is shown in figure 3.10 for both the zb and w series. With increasing HgS width a systematic increase in the PL lifetime is seen. In the following analysis we assume that in the ensemble PL dynamics all individual QDs have the same radiative lifetime τ_r while the non-radiative lifetime τ_{nr} may differ from dot-to-dot due to different concentrations of defects or ligand traps. The data for all samples is fit nicely by a multi-exponential fit wherein the PL decay is modelled by $I_{PL}(t) = \sum_{i=1}^{N} A_i e^{-t/\tau^i}$ for an N-exponential decay. Here τ^i is the effective single-exciton lifetime given by $\tau^i = \frac{\tau_r \tau_{nr}^i}{\tau_r + \tau_{nr}^i}$ and A_i is the relative fraction of the QDs in the i-th sub-ensemble normalized such that $\sum_{i=1}^{N} A_i = 1$. The QY in each sub-ensemble is defined as $\phi_i = \frac{\tau^i}{\tau_r}$ and the total QY can be expressed by $\phi = \sum_{i=1}^{N} A_i \phi_i = \sum_{i=1}^{N} \frac{A_i \tau^i}{\tau_r}$. Defining the average lifetime of the ensemble as $\langle \tau \rangle = \sum_{i=1}^{N} A_i \tau_i$, this relates the QY, $\langle \tau \rangle$ and τ_r by $\tau_r = \frac{\langle \tau \rangle}{\phi}$.

The data for the 2 ML CdS shelled series is fit nicely by a triexponential fit (N = 3) and the parameters are summarized in table 3.1 for the zb series. All show a fast sub 5 ns component followed by a second component of $\sim$25 ns. Lastly, the longest component varies from 62, 87, 121 to 136 ns as the HgS shell width is increased. Clearly, the longer time component is dominated by radiative relaxation while the fast components are likely due to non-radiative processes. The average lifetimes $\langle \tau \rangle$ vary from 34 ns to 58.2 ns as the HgS thickness increases, which when dividing by the QYs shown in figure 3.6 results in radiative lifetimes of 135, 153, 184 and 485 ns.
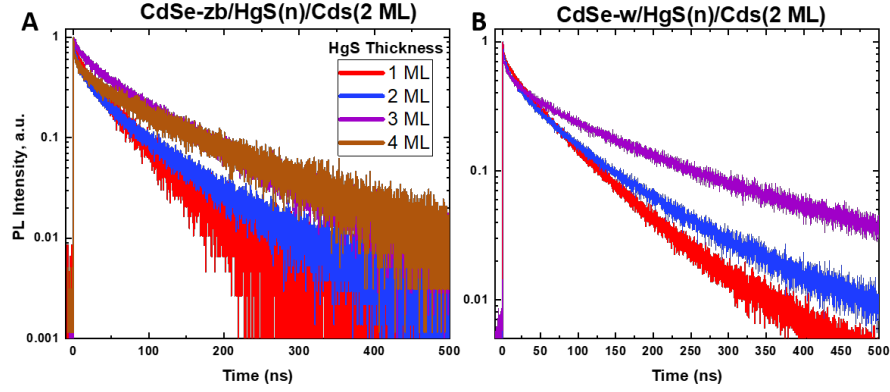
Figure 3.10: A) PL dynamics of CdSe-zb/HgS(n)/CdS(2) QDs. B) PL dynamics of CdSe-w/HgS/CdS(2) QDs.

	A_1	τ_1	A_2	τ_2	A_3	τ_3	$\langle \tau \rangle$	τ_{rad}
1 ML HgS	.212	2.2	.351	18.5	.437	61.6	33.8	135.4
2 ML HgS	.335	2.3	.355	20.9	.310	87.4	35.3	153.4
3 ML HgS	.190	4.9	.400	40.0	.410	120.6	66.3	184.3
4 ML HgS	.361	1.4	.260	24.0	.260	135.8	58.2	484.9

Table 3.1: Parameters of tri-exponential fits for the zinc-blende 2 ML CdS shelled series. All lifetimes are in nanoseconds.

Dynamics of the 4 ML CdS shelled series were done only on the zb cores. These samples show much more 'single-exponential' behavior than the 2 ML CdS sequence (figure 3.11A, a consequence of the thicker CdS shell passivating surface defect sites or reducing the probability a QD is charged. In figure 3.11B the dynamics of the 2, 4 and 6 ML CdS shelled samples on 1 ML of HgS are compared, normalized at $t = 0$. All samples show a similar long lifetime component while the 2 ML sample shows a strong fast component (shown clearly in inset of figure 3.11B) that is nearly completely removed in the 4 ML sample. Going from 4 to 6 ML of CdS results in a further, albeit slight, decrease in the amplitude of the fast component. Due to the strong relationship between decreasing the fast PL dynamic amplitude and the increasing QY the fast PL components can be attributed to charged QDs due to the trapping of charges on surface

sites leading to an increased probability for trion emission and Auger processes to occur. The is will be explored more thoroughly in the multi-exciton dynamics studied in the next chapter.
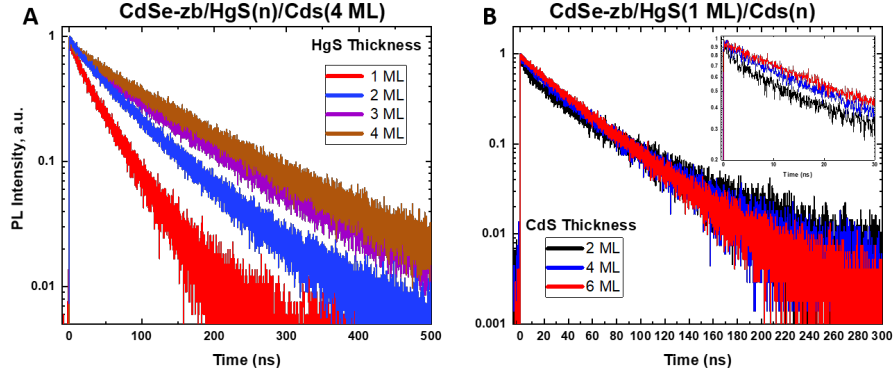
Figure 3.11: A) PL dynamics of CdSe/HgS(n)/CdS(4) series. B) PL dynamics of 1 ML HgS sample with 2, 4 and 6 ML of CdS. Inset: short time decay dynamics.

The 4 and 6 ML CdS shelling series are fit by a bi-exponential curve (N=2) with the reduction in the number of parameters needed for a good fit being an early indicator that a thicker CdS shell reduces the number of non-radiative decay channels. For the 4 ML CdS sequence, the fast component is nearly fixed at $\sim$30 ns while the long component increases systematically from 79 to 140 ns (table 3.2). The radiative lifetimes are calculated to be 73.5, 106.2, 183 and 306 ns respectively for 1-4 ML of HgS using the QYs from figure 3.6. These values differ significantly from the 2 ML CdS series for all but the 3 ML HgS sample; the cause of this is unknown, as the increase in CdS thickness should effect only the non-radiative lifetimes and not the radiative lifetime as the electron-hole overlap only changes by $\sim$1% and emission maxima changes only by $\sim$1 meV when changing the CdS thickness according to the EMA calculations.

	A_1	τ_1	A_2	τ_2	$\langle\tau\rangle$	τ_{rad}
1 ML HgS	.675	29.0	.325	77.8	44.8	73.5
2 ML HgS	.362	31.4	.638	88.7	68.0	106.2
3 ML HgS	.334	28.8	.666	126.0	93.5	183.4
4 ML HgS	.226	25.9	.774	138.8	113.3	306.1
1 ML HgS / 6 ML CdS	.217	19.0	.783	44.4	38.9	58.0

Table 3.2: Parameters of biexponential fits for the 4 ML CdS shelled series as well as for the 1 ML HgS / 6 ML CdS sample. All lifetimes are in nanoseconds.

In chapter 5 single QD studies of the CdSe-zb/HgS(1)/CdS(4) series are performed. There a single-exponential lifetime of ~75 ns is found, in excellent agreement with the $\tau_r = 73.5$ ns calculated from the ensemble PL dynamics. The 4 ML CdS sequence is of much higher quality than the 2 ML CdS sequence so we treat the τ_r values from table 3.2 to be more accurate than that from table 3.1.

6 ML of CdS has thus far has only been grown on the 1 ML HgS sample; the PL dynamics there indicate a much weaker fast component than in the CdSe/HgS(1)/CdS(4) sample. The average and radiative lifetimes are measured to be 38.9 ns and 58.0 ns, both faster than that measured in the 4 ML CdS sample. Again, this is not predicted by the calculations but can be explained via 1)removal of long-lived trap species and 2) the blue-shift in the emission spectra when moving from 4 ML of CdS to 6 ML as shown in figure 3.9. The cause of this is likely due to some physical or chemical change in the sample occurring during the high temperature CdS shell growth but the exact cause is still under investigation. Single QD measurements of these CdSe/HgS(1)/CdS(6) QDs show an average PL lifetime of 59 ns, in perfect agreement with the radiative lifetime measured here through the ensemble PL dynamics.

3.3.4 Theory of PL lifetimes

We conclude this chapter with a theoretical assessment of the PL lifetimes in CdSe/HgS/CdS heterostructures after beginning with an overview of the radiative decay of CdSe/CdS QDs.

The radiative lifetimes of bulk II-VI semiconductors are typically on the order of 1

ns [208], but low temperature PL decay dynamics of CdSe QDs are on the order of 1 μs. A long-standing puzzle, the cause was found not to be from surface states as initially thought but from the existence of a dark exciton in the ground state of the system [209–211]. Due to fine structure splitting during quantum confinement, the lowest band-edge state is optically forbidden leading to long lifetimes at low temperatures when thermal reactivation is impossible. At room temperature, there is a mixture of bright/dark states due to thermal activation and lifetimes are on the order of 15-20 ns. The radiative lifetime of CdSe can be calculated [212] via

$$\Gamma_{ex} = \frac{1}{\tau_{ex}} = \frac{8\omega n E_p}{9 \times 137 m_0 c^2} K\mathbb{D}^2 \tag{3.1}$$

where ω is the frequency of emitted light, n the refractive index of surrounding medium, E_p is the Kane energy parameter [213], m_0 is the free electron mass, K is the square of the overlap integral between the electron and hole wavefunctions in the confined exciton,

$$K = \left| \int d^3 r_e d^3 r_h \Psi_{ex}(r_e, r_h)\delta(r_e - r_h) \right|^2, \tag{3.2}$$

$\mathbb{D} = \frac{3\epsilon_{out}}{2\epsilon_{out}+\epsilon_{in}}$ is the depolarization factor, and $\epsilon_{in/out} = n_{in/out}^2$ are the high frequency dielectric constants of the emitting material and the surroundings. For CdSe NCs in a standard solvent this leads to a zero-temperature radiative lifetime of ~3.3 ns. Because the 1S electron and $1P_{3/2}$ hole transitions are optically forbidden via selection rules the lifetime of CdSe is increased by a factor of 16/3 at room temperature leading to a room temperature lifetime of ~17 ns [212], in excellent agreement with experiments.

We attempt the same analysis as that for CdSe but including the HgS MLs. The QDs are in hexane ($\epsilon = 1.9$) and 11.4 and 6.3 are used for the dielectric constants of HgS and CdSe, respectively [121]. The Kane energy of HgS is 21 eV [214] and 17.5 eV [215] for CdSe. The square of the electron/hole overlap integrals was calculated in figure 3.3B for the QDs in question here. In general equation 3.1 applied to CdSe/HgS/CdS in hexane results in

$$\frac{1}{\tau} = \Gamma = 1.505 \times 10^{11} \omega E_p K\mathbb{D}^2. \tag{3.3}$$

Here things get more difficult as now the electron is localized in the HgS well while the hole is delocalized; we need to decide on how to incorporate the Kane energy and

the dielectric constants into the calculations of the radiative lifetime. As a first order approximation we ignore the dielectric effect of the HgS layer and use the Kane energy of CdSe. This results (for the 1 ML sample) in a low temperature lifetime of 4.8 ns, merely 45% larger than that of CdSe, but serves to establish a lower-bound on the radiative lifetime in CdSe/HgS(1)/CdS QDs. On the other end of the spectrum if we ignore the dielectric constant of CdSe and treat everything as in HgS we find $\tau = 9.0$ ns, about a factor of three larger than for CdSe, while volume averaging the dielectric constants of CdSe and HgS results in a lifetime of $\sim$7.5 ns. These results indicate that the zero-temperature radiative lifetime of CdSe/HgS(1)/CdS should be around 2.5 times larger than for CdSe alone.

To verify this, we will need to measure the low temperature PL dynamics of the CdSe/HgS/CdS QDs, which is planned for a near-future study. Temperature dependent emission spectra were measured (not shown) and the PL was found to increase in intensity until saturating around 30 K. This saturation indicates the QY at low temperatures approaches 100%. Future work will also focus on the fine structure states of the CdSe/HgS/CdS QDs as currently we have focused only on the n and l quantum numbers in the EMA. Due to the general nature of II-VI semiconductors we assume that the same optical selection rules which apply to fine structure of CdSe apply to CdSe/HgS so that the room temperature lifetime will be increased by a factor of 16/3 over that of the low temperature lifetime. This implies the room temperature lifetime of CdSe/HgS(1)/CdS would be $\sim$48 ns, still considerably smaller than our measured τ_r values of 73.5 ns and 58.0 ns for the 1 ML HgS samples with 4 ML and 6 ML of CdS shell thickness. However, both of these decay curves are still bi-exponential while state-of-the-art CdSe QDs show single-exponential ensemble PL dynamics. Hence, growth of a thicker CdS shell leading to a single exponential PL decay could indeed show a radiative lifetime of $\sim$50 ns.

The measured PL dynamics of the 1-4 ML HgS series show consistently longer lifetimes with thicker HgS interlayers. To understand this with the above analysis the changing variables in equation 3.1 are emission frequency, square of overlap integral, and dielectric confinement. The emission frequency decreases by about 50% when going from 1 to 4 ML of HgS, which is not enough to explain the factor of $\sim$4 increase in radiative lifetime. The square of the overlap integral increases from 0.76 with 1 ML to 0.95 with

4 ML which should lead to an *increasing* PL decay rate contrary to our experimental results. Thus, the dominant contribution to the changing PL decay dynamics must come from changes in the dielectric confinement of the electrons and holes. The above study of the 1 ML HgS sample showed how drastically the lifetime could be altered with changing the $\mathbb{D}^2$ term; this role must be further understood before a systematic analysis of theoretical radiative lifetimes can be made in CdSe/HgS/CdS QDs.

3.4 Conclusions

In this chapter, we have explored the synthesis and electronic and optical properties of novel infrared emitting CdSe/HgS/CdS QDs. A dual use of SILAR and c-ALD synthesis techniques allow us to synthesize high-quality QDs of novel materials with the potential to be extended to the synthesis of a variety of new materials. The HgS well leads to a quasi type II structure with electrons localized in the HgS well while the holes are delocalized throughout the CdSe/HgS heterostructure.

The emission wavelength is increased from 750 nm out to nearly 1200 nm with increasing HgS width. Through growth of 4 or 6 ML CdS outer shells the QY can be increased to nearly 70%, remarkably high for an NIR emitting material. The radiative lifetime is found to increase systematically with thicker HgS interlayers, and thicker CdS outer shells result in close to single exponential decay dynamics.

The next chapter will concern the multi-exciton decay dynamics of CdSe/HgS/CdS QDs, while the final chapter will show preliminary studies of single photon emission from CdSe/HgS/CdS QDs. Extending single photon emission out into the NIR is one of the primary applications of these QDs, and will be covered in depth in that chapter.

CdSe/HgS/CdS QDs show great potential for broad use as fast, stable and narrow linewidth NIR emitters. Future work on alloying the CdSe, HgS, and CdS interfaces should lead to the same ultra-high quality optical properties in the NIR as shown in compositionally graded CdSe/CdS QDs.

3.4.1 Methods

Synthesis: The synthesis was primarily described in-text. The temperatures cited were found by systematic studies of emission and QY of QDs grown at various temperatures.

The QDs were dispersed in toluene or hexane for all optical measurements.

Spectroscopy: The steady-state absorption and PL were measured using a Horiba FluoroMax system. Time resolved PL was done using a SNSPD single photon detector, and the sample was excited with a 3.1 eV pulse train from a Ti:sapphire amplifier (Coherent RegA-9000) at 250 kHz.

Calculations: The EMA calculations were done in Mathematica using a modified version of code used previously for PbSe/CdSe samples. All parameters used were found in literature.

3.4.2   Acknowledgements

Chapter 4

Multi-exciton dynamics in CdSe/HgS/CdS Quantum Dots

In the previous chapter we studied the synthesis, electronic states and optical properties of novel CdSe/HgS/CdS QDs. In this chapter we will build off of this foundation by examining the dynamics of multi-excitons (when the average number of excitons per dot $\langle N \rangle >> 1$) in CdSe/HgS/CdS heterostructures. Intuitively, one might predict that the strong confinement of the electrons in the HgS layer would lead to intriguing dynamics when N >> 1 excitons are pumped into the system. This is indeed the case as we study in the CdSe-zb/HgS(n)/CdS(4) series. We begin with a power dependent PL dynamics study on the 1 ML sample, where we see a biexciton component but also a second, longer fast component appear at high excitation powers. The same measurements are done on the 2-4 ML HgS samples and comparisons are made. We conduct a power dependent steady-state PL study where we obverse weak emission at ~620 nm from what presumably is the CdSe core.

4.1 Power Dependent PL dynamics CdSe/HgS/CdS Quantum Dots

Here the samples are excited with the same 3.1 eV pulses as for the low-fluence measurements using the 2nd harmonic of a Ti:sapphire laser from a RegA amplifier. Operated

at 250kHz, these pulses have a FWHM of ∼200 fs, and the SNSPD photon-detection system has a time resolution of ∼40 ps. The pulse train is focused tightly onto a ∼70 μm spot on the sample to enable the excitation of large numbers of excitons. The power is varied from 12.5 μW to 25 mW so that the per-pulse fluence varies from 5.8×10^{12} to 1.2×10^{16} photons/cm^2. The samples are continuously stirred to prevent charging of the QDs with prolonged exposure to the incident laser pulses.

The probability of a QD absorbing a photon in any given excitation cycle is a Poissonian process as each absorption event is independent of any prior absorption events. This implies that for an excitation power that results in $\langle N \rangle$ excitons per dot on average the probability of finding a QD in the Nth excitonic state is

$$P(N, \langle N \rangle) = \langle N \rangle^N e^{-\langle N \rangle}/N!. \tag{4.1}$$

Furthermore, $\langle N \rangle$ can be expressed in terms of the per-pulse photon fluence j$_p$ multiplied by the absorption cross section σ, $\langle N \rangle = \sigma j_p$. This allows the absorption cross section to be readily calculated by measuring the saturation in the PL dynamics. Following all multi-excitonic recombination, which likely is non-radiative, each QD eventually emits a single exciton before the system returns to its ground state. Hence the late time PL dynamics can be modelled by I$_{PL}$(t→ ∞) = 1-p$_0$ = 1-e$^{\langle N \rangle}$ = 1-e$^{\sigma j_p}$ (i.e, the probability that no excitons are excited goes to zero at high excitation powers, which is observed via the saturation of the long-time PL dynamics). By varying the power of a sample and plotting the long-time PL amplitude $\langle N \rangle$ and σ can be determined.

We begin with an analysis of the power dependent dynamics of the 1 ML sample and then extend that to the 2-4 HgS ML samples. To prevent overloading the SNSPD detector a neutral density (ND) filter is used to limit the amount of light entering the detector. We operate at 250kHz so the counts/s is kept below 10kHz/s. This means a photon is detected once every ∼20 laser cycles allowing for sufficient time for the nanowire to cool. To accurately count the number of photons entering the system we convert the ND filter to fractional transmittance defined by $T = 10^{-ND}$. This, along with keeping track of measurement time for each power, allows us to accurately measure photon decay events as a function of excitation power.

The raw data for the 1 HgS ML sample is shown in figure 4.1A,B. Figure A shows the full PL decay over 200 ns while figure B is zoomed-in on the first 3 ns. The time between

data points is 8 ps, and at low fluence (dark green) we observe the same decay dynamics as that measured in figure 3.11A with a larger beam size and lower resolution. In figure 4.1A a clear saturation is seen at longer times allowing us to convert the excitation power into $\langle N \rangle$, as shown in the legend. Detailed analysis of the saturation behavior will be done later. Fast components can be seen at increasing powers, most easily seen in figure 4.1B. Such decay dynamics is typical of QDs where biexciton (BX) decay (quasi-particle formed from 2 excitons which may recombine radiatively, leaving behind an exciton, or non-radiatively via the Auger process) dominates due to the strong confinement of the system. The fast BX component can be initially seen in the 3rd decay from the bottom, where $\langle N \rangle = 0.16$; the appearance at such low fluences is due to the Poissonian nature of photon absorption as even at $\langle N \rangle = .16$ there is still a 1.1% probability a QD has a BX via equation 4.1.
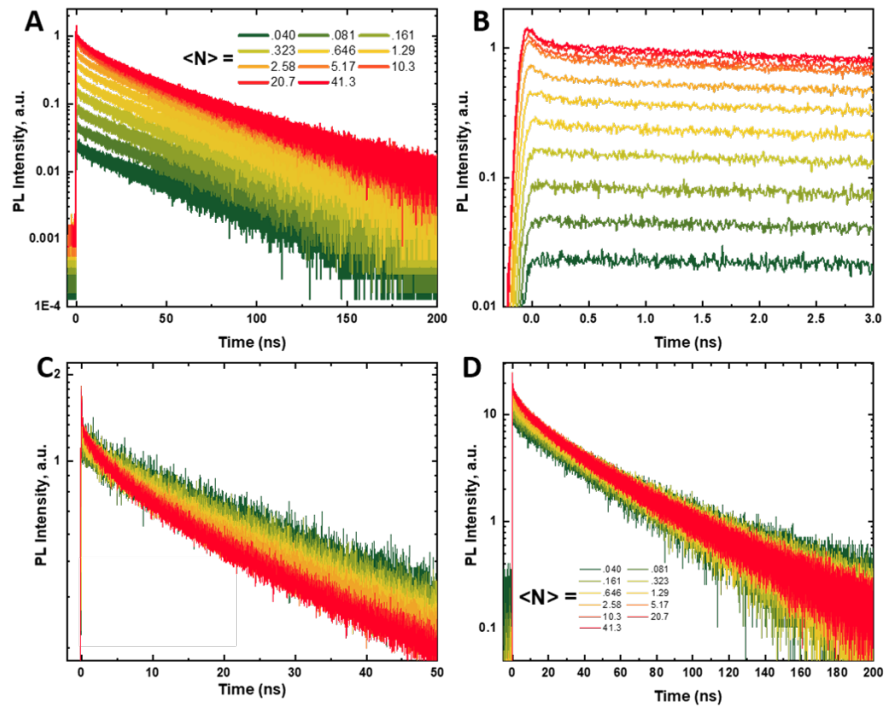
Figure 4.1: Power dependence of the 1 ML HgS sample plotted 4 different ways. A) Raw data showing full PL decay, B) short time decay of raw data, C) decays normalized at 3 ns and D) decays normalized at 100 ns.

To isolate the multi-exciton components over the single exciton (X) components one

typically normalizes the decay at 'long times' [51, 216] where long means $t >> \tau_{BX}$. As τ_{BX} is on the order of 100 ps, this means that normalizing at any time larger than 1 ns should result in identical decay dynamics for all powers at longer times. Such analysis is done in figure 4.1C, yet instead of the decay dynamics following each other at longer times the higher powered samples are found to have a second, longer fast component arise as well. To see this fully, we instead normalize the PL decays at 100 ns in figure 4.1D. Now the decays at long times, starting around 70 ns, all have the same decay rate, namely that of the single exponential decay rate. At shorter times there is the BX component near $t = 0$ but also a second fast component with lifetime of $\sim$10 ns. Such behavior is unusual and will be examined extensively throughout this chapter.

To isolate the fast components the decays normalized at 100 ns as in figure 4.1D and then the low intensity single exciton decays are subtracted. The resulting curves feature only the multiexcitonic component (figures 4.2A,B) allowing us to focus on those dynamics exclusively. In (A), the data is the same data as in figure 4.1D just with the low-fluence curves subtracted while in (B) the decays are normalized at 2 ns. In 4.2B, the BX component is clearly seen rising over the longer fast component, and also the longer fast components are all seen to follow the same decay.
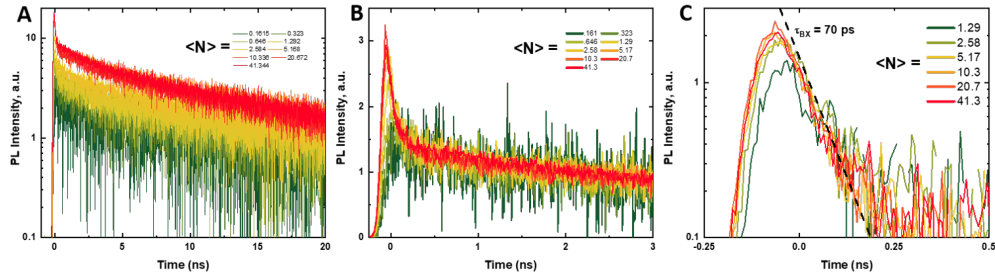
Figure 4.2: A) Isolated multi-exponent components found by subtracted the self-similar single exciton decays. B) The decays from (A) normalized at 2 ns showing the self-similar longer multi-exponential feature as well as the strong BX component. C) Isolated BX component by subtracted the self-similar longer fast component decays in (B).

Lastly, we take the data from 4.2B and subtract off the lowest intensity decay to isolate the BX component, similar to what was done initially going from figure 4.1D to 4.2A. Such analysis is typically only done once to isolate the BX component [217], yet here it must be done twice due to the appearance of the second fast component.

This process results in an isolated BX decay (figure 4.2C) with a lifetime of 70 ps. Again, the BX component is found to not change with increasing powers even when the fluence produces $\gg 2$ excitons per dot. Such behavior can be attributed to the ~40 ps resolution time of our detector, as $N > 2$ exciton recombination processes will happen even faster than 40 ps [218]. The radiative lifetimes of higher-order exciton states can be expressed via statistical scaling [219–221] where the lifetime of a N-exciton complex is $\tau_{r,NX} = N^{-2}\,\tau_{r,x}$. Therefore $\tau_{r,2X} = \tau_{r,BX} = \tau_{r,x}/4$. Based on the measured τ_r for the single exciton we would predict that the BX component for the 1 ML HgS sample has a lifetime of 15-20 ns, orders of magnitude longer than the measured value of 70 ps. This can be attributed to highly efficient Auger recombination in QDs [218], particularly in these QDs where the electrons are tightly bound in the HgS well.

The same analysis is performed for the 2-4 ML HgS samples and similar behavior is seen. Rather than going slowly through each one, the decays normalized at 100 ns (the same as figure 4.2D) are shown in figure 4.3A-C. In figure 4.3A a strong second fast component is seen in the 2 ML sample akin to that seen in the 1 ML sample, while in the 3 and 4 ML samples a second fast component is seen though not as strong as in the 1 and 2 ML samples. However all samples do show this second fast component in addition to the BX decay indicating this behavior is intrinsic to the CdSe/HgS(n)/CdS(4) QD samples themselves and not just an artifact of the very strongly confined 1 ML sample. Comparisons of the multi-exciton decay components for 1-4 ML HgS is shown in figure 4.3D; all show clear multi-exponential decay and the thicker HgS shelled samples have stronger BX emission.

The multi-exciton decay components in figure 4.3D are fit with a tri-exponential function. All samples show a sub 100 ps BX component followed by a ~2 ns component and a ~20 ns component. The BX lifetimes are found to be 70 ps, 98 ps, 75 ps and 64 ps for 1-4 ML of HgS, respectively. The 70 ps for the 1 ML agree perfectly with that found from subtracting off the self-similar longer multi-exponential components in figure 4.2C. This fast BX lifetime is dominated by Auger recombination in all samples as the radiative BX lifetime is $\tau_r/4$ and τ_r was found in chapter 3 to be ~70 - ~300 ns for the 4 ML CdS shelled series.

It is well known that Auger lifetimes scale with the volume of the QD [216, 222, 223], explained due to the decreasing confinement at larger QD volumes. However such
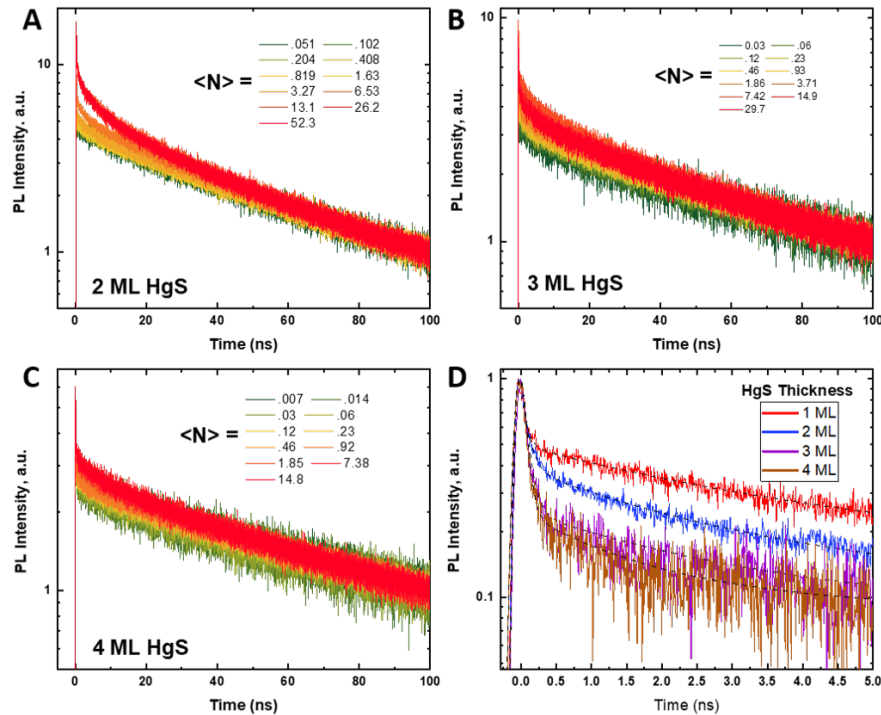
Figure 4.3: PL decay dynamics normalized at 100 ns for A) 2 ML, B) 3 ML and C) 4 ML HgS samples. D) Multi-excitonic decays with the self-similar single exciton components subtracted off for all 4 HgS MLs.

behavior is not observed in these CdSe/HgS/CdS QDs. The volume of the CdSe/HgS region increases from 20.4 nm^3 with 1 ML to 38.6, 65.1 and 101.6 nm^3 for the 2-4 ML HgS samples. Hence, if the 1 ML Auger lifetime is 70 ps we would expect that the 2 ML sample has an Auger lifetime of ~130 ps, 3 ML ~220 ps and 4 ML ~350 ps. What is observe is drastically different, with the 2 ML Auger lifetime ~100 ps and the 3 and 4 ML Auger lifetimes 75 and 64 ps. The small rise and then drop of Auger lifetime (one might argue that the small changes in Auger lifetimes are negligible and they could be treated as the same) with increasing HgS width is extremely unusual and must be a consequence of the unique heterostructures here. In addition to the larger volume of higher ML HgS samples, based on the EMA calculations and experiments we also know that increasing the HgS width does several other things: 1) the 1S and 1P electrons drop further into the HgS well 2) the 1S and 1P separation changes from ~20 meV to ~30 meV 3) The 1D state drops into the HgS well at the 3 ML HgS thickness 4) the

square of the electron-hole overlap integral increases from $\sim$0.6 to $\sim$0.85 and 5) all of the samples have longer multi-exciton components and these lifetimes are also comparable for all samples studied here.

First we will examine the last comment, that all of the samples have similar longer high-fluence lifetimes in addition to the BX component. As mentioned previously, this longer component has a bi-exponential decay with lifetimes of $\sim$2 ns and $\sim$20 ns. Recall that the 2 ML CdS shelled series (figure 3.10 and table 3.1) needed a tri-exponential fit to model the low-fluence PL dynamics where the longest lifetime increased systematically with increasing HgS widths while the two shorter lifetimes were less susceptible to changing HgS widths. In fact, the two short time components for the low-fluence 2 ML CdS samples were $\sim$2 ns and $\sim$20 ns for all but the 3 ML HgS sample, exactly the same as that found for the 4 ML CdS series in the multi-exciton PL dynamics at high fluence! This 'coincidence' led us to directly compare the high-fluence 4 ML CdS decay against the low-fluence 2 ML CdS decay. Shown in figure 4.4, near perfect agreement is seen between the two curves for all four samples with varying HgS widths, minus the strong BX component near $t = 0$ in the high-fluence 4 ML CdS samples.
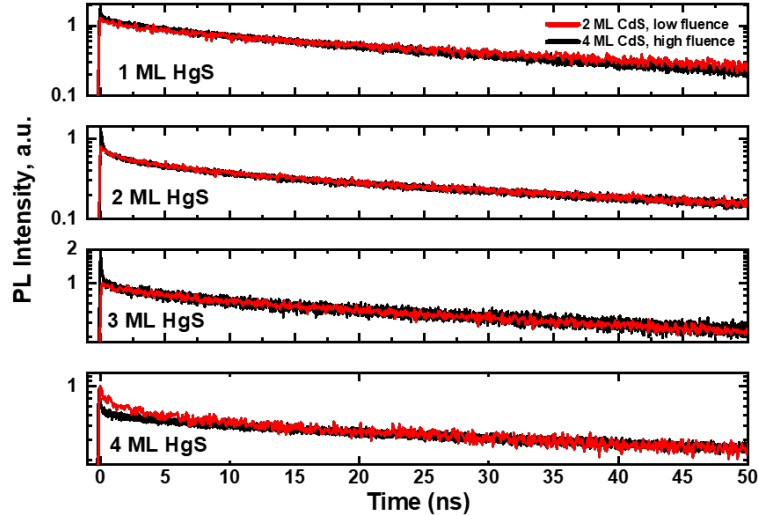
Figure 4.4: Direct comparison of decay dynamics for low-fluence 2 ML CdS samples (red) with high-fluence 4 ML CdS samples (black).

Such results strongly suggest that the QDs are charged even at low fluence in the 2 ML CdS shelled series. Photo-induced charging of bulk semiconductors has long been understood [224]. There, photoionization happens via the removal of an electron (typically not holes, as holes tend to have higher effective masses than electrons) to a zero-energy vacuum state after absorption of a photon of sufficient energy. In QDs the incident high energy photon ejects the electron to an acceptor state in the ligand shell or surrounding solvent or encapsulating matrix [225]. Work on PbSe based IR emitting QDs has shown strong photoinduced charging with 3.1 eV excitation (as is used here) and an absence of photoinduced charging at 1.55 eV excitation [225, 226]. This implies the photoinduced charges require photons of sufficient energy E $>>$ E$_G$ in order to efficiently promote electrons to the trap states.

That these effects of charging are seen in the ensemble 2 ML CdS series PL dynamics even at very low fluences, when $\langle N \rangle << 1$, implies at least one of the following: 1) the dots remain charged for long periods of time so that the probability of accepting a photon in the charged state is high or 2) the QDs are intrinsically charged. Charge-separated states in PbSe and PbS *were* found to have extremely long lifetimes of 20 - 85 seconds [225], giving credence to the first option. Additionally, Chen and Guyot-Sionnest showed that HgS and HgSe QDs can be intrinsically n-doped in ambient conditions [227]. Through detailed electrochemistry measurements they found the Fermi level in HgS QDs to lie ∼400 to ∼600 meV above the HgS conduction band minimum. While electrochemistry measurements have not been performed on these dots at this time their being intrinsically charged would explain the experimental results. In figure 3.4A the electron and hole energy levels were plotted as a function of HgS thickness over a 3.0 nm diameter CdSe core. The bottom of the conduction band is the zero energy level on the graph and the 1S energy level is found to lie ∼900 meV and ∼350 meV above the HgS conduction minimum for the 1 and 4 ML samples. These values are reasonably close to the Fermi level reported by ref [227] though this system is considerably different than theirs so again, more experiments are needed before we can definitively conclude that the QDs here are intrinsically charged.

Contrary to the 2 ML CdS series, in the 4 ML CdS series the fast components are not strongly seen at low fluences. However, the fast component does not come in only at $\langle N \rangle >> 1$ as a gradual increase in the fast component is seen for all but the

lowest excitation powers in figures 4.1C,D. At low fluences the absence of a charging component in the PL dynamics in the 4 ML CdS series can be attributed to either the increased shell thickness making it harder for photoionization to occur as the surface ligands, which likely are the acceptor states for the electrons, are further away from the CdSe/HgS core, or else the CdS shell prevents ambient charging of the QDs for the same reason, namely that it is more difficult for an electron or hole to tunnel from the surface to the HgS well. The rise of the fast components with increasing exciton occupancy is interesting; it could be that there is a distribution in the number of traps per QD so that as more QDs are excited per pulse the probability that a charged QD is excited increases. At the same time as individual QDs start to get multiply excited in a single pulse (recall the BX component appears at only $\langle N \rangle = 0.16$ in figure 4.1B) Coulomb interaction between two electrons, or two holes, will be very large due to the ML thicknesses of the HgS region. Hence, through Coulomb repulsion a charge may be 'not allowed' to relax to the 1S state and remain in the 1P state or higher, after which photoionization may more readily occur as it is already in, or near, the CdSe core states. Such a 'Coulomb blockade' has been observed in core/shell QDs with volumes much larger than our HgS shell volumes [18] so such behavior is not unprecedented.

4.1.1 Saturation of the Short and Long Time PL Amplitudes

Throughout this chapter the average number of excitons excited per dot per pulse, $\langle N \rangle$, has been used extensively. Finally we devote time to analyzing the saturation behaviors in depth. Per equation 4.1 we expect the long time PL amplitudes to saturate as $I_{PL} \propto 1 - e^{\langle N \rangle}$. Due to the second fast component we observe at high powers we take the 'long time' component to be 100 ns for all samples studied here. Fits to the Poisson model with the PL amplitudes at 100 ns taken from figure 4.1A and analogous figures for 2-4 ML HgS are shown in figure 4.5A with the different data sets offset for clarity. Each curve fits the data nicely and allows us to calculate $\langle N \rangle$ and σ for each sample. The fits indicate absorption cross sections of 5.5, 7, 4 and 2 x 10^{-15}cm^2 for 1-4 ML of HgS. The error bars on these fits are large, so the absorption cross section may be taken as constant between the 4 samples until further measurements are done. This contradicts intuition, where the larger HgS shell sizes should increase the absorption cross section as the corresponding CdS shell thicknesses will also be larger. To verify these numbers TA

measurements will need to be done on all 4 samples and the saturation of the bleaching of the 1S states examined. To date this has been done with only the 1 ML HgS / 2 ML CdS sample (see below).

The saturation of the $t = 0$ component is shown in figure 4.5B with the data sets offset for clarity. The saturation of the BX component can be attributed to the two-fold degenerate 1S state in the sample. As mentioned previously higher order recombination processes (tri-excitons, etc.) occur too fast to be registered on the SNSPD system. A direct comparison of the PL amplitudes at 0, 1 and 100 ns (from figures 4.1A,B) is shown in figure 4.5C for the 1 ML HgS sample. Saturation at $t = 1$ ns is also included due to the appearance of the second fast components at higher fluences; the 1 ns delay is long enough to ignore the BX component while still capturing all of the secondary fast components. The 0 and 1 ns components both start off at the same value a factor of $\sim$9 above the long tail component. The large separation between the 0 and 1 ns delays and the 100 ns delay can simply be attributed to recombination of electrons/holes reducing the amplitude of the long time component. The 0 ns and 1 ns amplitudes do not separate until $\langle N \rangle \sim 1$, after which the $t = 0$ component rises $\sim$50% over the 1 ns component. The ratios of the 0 ns amplitude with the 1 ns and 100 ns amplitudes are shown in figure 4.5D for all samples, using the color-coding from figures A,B. The closely packed group of data points at the bottom shows the ratio between 0 ns and 1 ns amplitudes. All of the ratios there start near 1, as at low fluence there is no BX or secondary fast component decays, and they saturate between 1.5 and 2.

The more sparsely packed group of data at the top shows the amplitude ratios for $t = 0$ and 100 ns. The spread of values at low fluence can be attributed to the increasing PL lifetimes with HgS thickness; the thinner HgS samples decay faster and hence their ratio at all fluences is higher than for slower decaying samples. The ratio from low fluence to high fluence varies from $\sim$1.75 for the 4 ML sample to 3.6 for the 2 ML sample, with the 1 ML sample ratio being 2.7 and the 3 ML sample 2.4.

The BX component has 4 recombination pathways, so the PL of the BX component should saturate at 4 times the single exciton component. Likewise, charged states known as trions (bound states of 2 electrons and one hole (T^-) or one electron and two holes (T^+)) will have radiative lifetimes half that of neutral excitons, and correspondingly will have a saturation at twice that of the single exciton level. If the data is normalized at
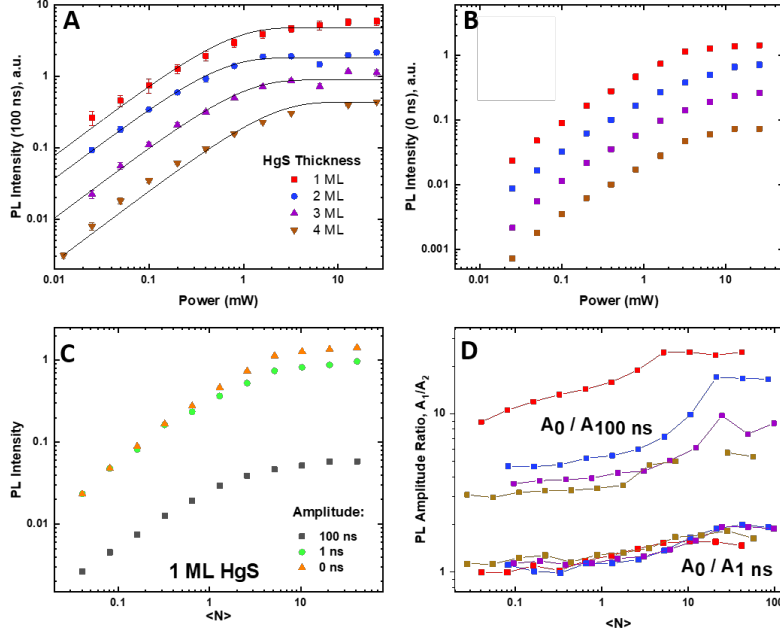
Figure 4.5: A) Saturation of PL amplitude at 100 ns, where data is normalized to in figure 4.1D and 4.3A-C. Lines are from 1 - p_0 Poissonian fits. B) Amplitude saturation at $t = 0$ ns. C) PL amplitudes at 0, 1 and 100 ns for the 1 ML HgS sample. D) Ratio of PL amplitudes at 0 and 1 ns (bottom group of data points) and ratio at 0 ns and 100 ns (top group of data points.

low fluence and scaled such that long time component saturates at 1, as is done for the 2 ML HgS sample in figure 4.6A, we see that the 1 ns amplitude then saturates at 2 and the 0 ns component saturates near 4 as expected from statistical scaling. This process is shown schematically in figure 4.6B overlaid on the PL decay normalized at 100 ns (figure 4.3A) but on a log-log scale. The fast component is attributed to BX recombination, which is dominated by the Auger process. The second longer components are taken to be trions, either negative (X^-), as shown first in the schematic, or positive (X^+) as is shown later. Further measurements using photochemical charging will need to be done before positive and negative trions can be distinguished in this system. The trions show lifetimes of ~2 and ~20 ns, much greater than the Auger lifetime found for the BX to be <100 ps. The cause of this is currently unknown, although the 20 ns lifetime could be due to X^+ where the confinement is not as great due to the delocalized holes. Lastly,

only a single exciton remains which recombines radiatively with a lifetime of ~100 ns (for the 2 ML HgS sample).
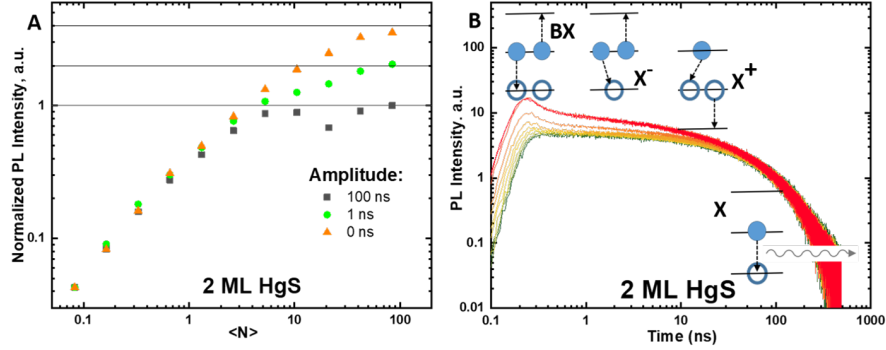
Figure 4.6: A) Saturation of the 2 ML HgS amplitudes normalized at low powers. Here, the long delay time saturates at $1/2$ the value of the 1 ns component and $1/4$ the value of the 0 ns component, in agreement with statistical scaling for exciton, trion and biexciton recombination pathways. B) PL decay of 2 ML HgS sample normalized at 100 ns on a log-log scale. Fast component is due to biexciton (BX) recombination, while longer fast components are attributed to either positive (X^+) or negative (X^-) trion recombination. Last term due to exciton radiative recombination.

As shown in figures 4.5D and 4.6A, the 2 ML HgS sample is fit nicely by the expected saturation values. The other samples have similar values for the amplitude saturation of the 1 ns delay but the $t = 0$ component saturates at less than 4 for all of the samples except the 2 ML sample. This likely is due to some combination of neutral and charged BX emission in the QDs, something that needs to be investigated more thoroughly. On basic photon absorption principles the exciton intensity should increase linearly, so that $I_{PL,X} \propto \langle N \rangle$. Following this the PL intensity of the BX should vary as $I_{PL,X}^2 = \langle N \rangle^2$ due to two photon absorption events needing to occur before BX recombination is possible. However, figure 4.5B shows nearly a linear dependence at all fluences until saturation. Evidently something more complicated than Poissonian absorption of excitons is occurring in these QDs; full analysis will require TA across all 4 samples as well.

4.1.2 CdSe Core PL Dynamics

Thus far we have focused on the PL dynamics from the HgS emitting layer and neglected weak emission from the CdSe layer. We consider that fully here and show that the PL dynamics indicate this is a natural process arising from fast radiative recombination of excitons prior to relaxing to the HgS layer. The core emission is only seen in the zinc-blend crystal structure samples; it is absent in the wurtzite samples. The cause of this is unknown and will not be discussed here.

The power dependent PL emission spectrum is shown in figure 4.7A normalized to the peak emission value. The shape of the HgS layer is seen to be constant over a range of exciton numbers from $\langle N \rangle << 1$ to $\langle N \rangle >> 1$ indicating the binding energies of any multi-exciton species must be very small. In addition to the main PL peak weak emission is seen at 620 nm. As this is consistent with emission from CdSe/CdS QDs we refer to this emission as 'core' emission. The intensity of the 'core' PL is $\sim 1\%$ that of the HgS PL as shown in figure 4.7B. Such low intensity indicates extremely low QY from the core PL, likely do to the fast relaxation of electrons to the HgS layer.

At first glance one might think that this PL is due to a sub-ensemble of CdSe/CdS QDs. Indeed, imperfect shell growth of the 1 ML HgS sample could in principle leave some QDs uncoated with HgS. However, the PL dynamics of the 1 ML HgS sample core emission over a range of powers from $\langle N \rangle << 1$ to $\langle N \rangle >> 1$ show that the core PL dynamics is always much faster than that expected for radiative recombination in CdSe/CdS QDs indicating there are not sub-ensembles in these samples. A bi-exponential fit of the lowest fluence decay (figure 4.7D green) provides lifetimes of 240 ps (65% amplitude) and 1.5 ns (35% amplitude). Treating the radiative lifetime of the core PL as ~ 20 ns (typical for CdSe QDs) and the QY as $\sim 1\%$ from the ratio of the core and HgS layer PL areas implies that the measured lifetime of the core PL should be τ_r x QY = 20 ns x .01 = 200 ps, in excellent agreement with the measured fast components in figures 4.7C,D.

To determine the origin of this core PL we return to figure 3.4A and examine the relevant energy levels. The 1Pe-1Sh transition energy is 2.02 eV in near perfect agreement of the PL emission seen here. In the next section this will be examined more thoroughly. 1Pe-1Sh transitions have been observed in core/shell QDs previously [23].

The core emission gets progressively weaker with a thicker HgS width which can
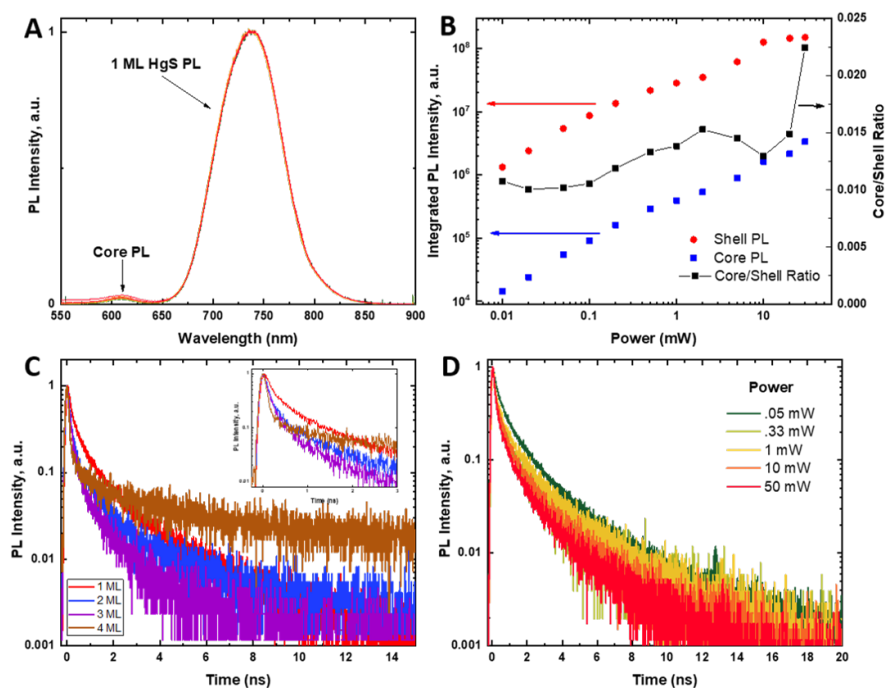
Figure 4.7: A) Emission spectrum of the 1 ML HgS sample showing the weak core emission. B) Integrated areas of the core (blue) and HgS (red) emission as well as the ratio between them (black, right axis). C) Core PL dynamics for 1-4 ML of HgS. Samples are excited at high powers so $\langle N \rangle >> 1$. D) Power dependence of the core PL dynamics from $\langle N \rangle << 1$ to $\langle N \rangle >> 1$.

intuitively be explained by a faster electron relaxation time to the HgS well the deeper the 1S state falls inside the HgS layer. Hence, to see the core PL from these samples they must be excited at high excitation powers. Such dynamics are shown for 1-4 ML of HgS in figure 4.7C as the samples are pumped with high-fluence ($\langle N \rangle >> 1$) pulses. The short time component gets progressively faster with thicker HgS layers, in agreement with the previous argument that electron relaxation to the HgS well will be faster in samples with more MLs of HgS. For the 3 and 4 ML samples, the decay is close to resolution-limited (inset of figure 4.7C), indicating that the PL decay is near $\sim$40 ps. In addition to the fast component a second longer component is seen all the samples. The cause of this second component is likely due to 1) detrapping of charges on the ligand shell 2) re-excitation of charges from the 1S state through Coulomb repulsion or 3) direct trap emission from the ligand shell or defect sites.

4.2 Transient Absorption of CdSe/HgS(1)/CdS Quantum Dots

Having examined the interesting PL dynamics in CdSe/HgS/CdS QDs many questions still remain. The BX lifetime for all four samples is comparable, all the samples have a longer fast component, there is core emission with a fast (∼100 ps) and slow (∼1-2 ns) component, and the scaling of short time and long time components are similar, indicating that the quadratic BX dependence is not seen. Quantification of PL dynamics is limited by the resolution of our detector, ∼40 ps, and the recombination rate of electron-hole pairs in the system. To this end, we now perform TA spectroscopy on the CdSe/HgS(1)/CdS(2) sample. These results are preliminary, and TA data on the 4 ML CdS sequence for all 4 MLs of HgS needs to be done before systematic conclusions can be made in comparison to the PL data.
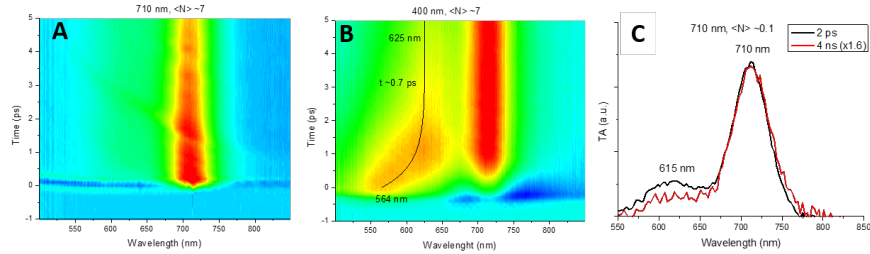
Figure 4.8: High-fluence TA spectra excited at A) 710 nm and B) 400 nm. Clear bleaching is seen of the 1S state as well as a core state. C) The core state is visible even at low fluence and 710 nm excitation.

In figure 4.8A,B an overview of TA data for the CdSe/HgS(1)/CdS(2) QDs excited at (A) 710 nm and (B) 400 nm is shown. The system is pumped resonantly at 710 nm in order to isolate the electron/hole relaxation dynamics versus the intrinsic 1S dynamics. Figure 4.8A shows a very strong 1S bleach when pumping resonantly, but also shows a weak peak at 615 nm even at low fluence (seen more clearly in figure 4.8C). With 400 nm excitation there is a pronounced core peak with a fast decay and redshift of energy as well as a delay in the growth of the 1S feature. This can be attributed to electron relaxation to the HgS well, as will be discussed later. It is intriguing that the core feature is seen even when pumping resonantly at 710 nm. This implies that the core PL

and absorption must be related to the 1Sh state, as that is the only delocalized state absorption at low fluences. Inspection of figure 3.4A indicates that for the 1 ML HgS sample the 1Pe-1Sh transition lies at 610 nm, a likely source for the core absorption feature seen here and the PL seen in the previous chapter. Such behavior has been observed before [23] in PbSe/CdSe core/shell structures; optical selection rules are not strictly conserved in core/shell structures as inversion symmetry breaks down allowing the potential for transitions where $\Delta n \neq 0$ and $\Delta l \neq 0$ like 2S-1S or 1P-1S [215].
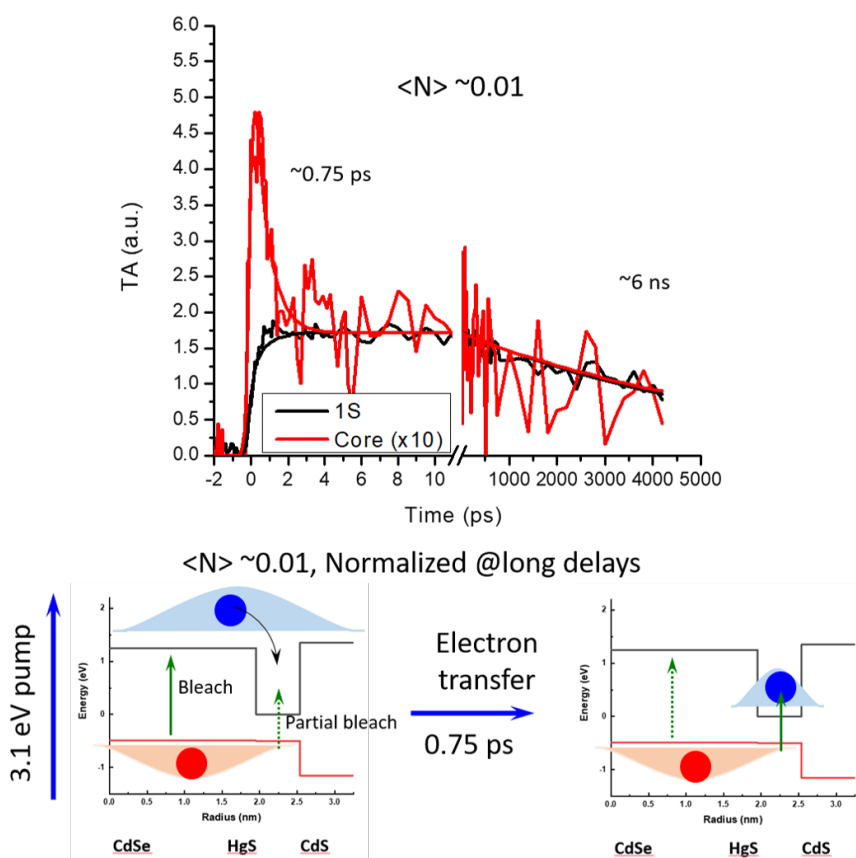
Figure 4.9: Low-fluence TA with 3.1 eV excitation. The 1S state shows no fast component and a 6 ns long component while the core state shows a fast 750 fs component. The fast component is evidence for electron localization in the core as indicated by the schematic.

Now we go more in depth through each of the TA results. First we study the low-fluence dynamics with 400 nm excitation. The core and 1S features are normalized at

long times and the decays are found to line up perfectly (figure 4.9). The core component has an additional fast 750 fs component which can be attributed to electron relaxation into the HgS localized 1S state (figure 3.2C). This is twice as fast as the 1.5 ps electron localization time in CdS/HgS/CdS QDs [228] though these QDs were different sizes so more data is needed before this can be considered conclusive. The bottom of figure 4.9 is a schematic of the initial absorption and then relaxation processes.

At high-fluence ($\langle N \rangle \approx 7$) the 1S and core features are no longer self-similar (figure 4.10). The 1S state shows a tri-exponential decay with lifetimes of 20, 180 and 6000 ps while the core state shows a tri-exponential decay with lifetimes of 7, 60 and 3500 ps. The amplitude of the fast component on the core state is much stronger than the fast component on the 1S state. Interestingly, the fast component of the core feature (7 ps) is an order of magnitude slower than for low-fluence. This is likely due to the Coulomb blockade suggested above, wherein charges are impeded from relaxing to the core due to charges already being there.[1]   The cause of this is currently unknown, but a schematic of the possible processes involved is shown in the schematic at the bottom of figure 4.10.

Lastly the dynamics when the system resonantly are examined (figure 4.11). The dynamics are similar for both low and high power between the core and the 1S features. This feature is attributed to 1Sh absorption as the 1Pe state is not excited here. At high excitation powers the core bleach becomes more pronounced. As mentioned with the longer fast components in the PL decays, this likely has to do with excitons getting 'pushed out' of the HgS well due to the higher occupancy there when the system is strongly excited.

To date we have only performed TA on the CdSe/HgS(1)/CdS(2) sample though it was the 4 ML CdS samples studied extensively earlier in this chapter. For this reason we will not spend time extensively comparing the measured lifetimes of the TA versus the PL as any conclusions drawn would not be conclusive at this time. However, tri-exponential fits were needed for all studied dynamics (low/high power and 1S/core states) as was found in the low-fluence 2 ML CdS series (figure 3.10). The fastest component in TA is due to relaxation to bandedge states, whereas the hundreds of ps

---

[1] This is in addition to state-filling, which will obviously also cause some charges to remain at higher energy states.
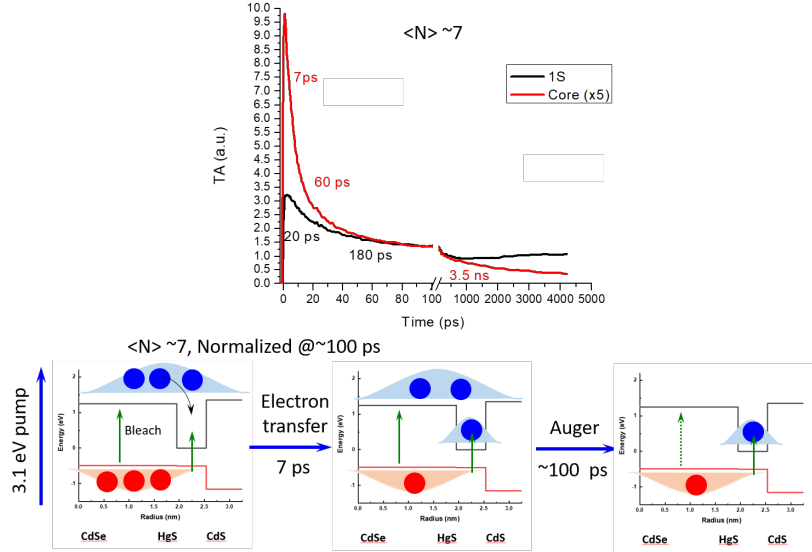
Figure 4.10: High-fluence TA with 3.1 eV excitation. The curves are no longer self-similar and the electron localization time is now 7 ps. Auger processes dominate in this situation when $\langle N \rangle >> 1$.

and ten ns components are likely due to Auger processes and radiative recombination. TA on the 4 ML CdS samples, where the fast components in the PL at low fluences was absent, will provide important additional insight into what is happening in these samples.

4.3 Conclusions

In this chapter we have examined the multi-exciton dynamics of CdSe/HgS/CdS QDs. With an emphasis on the 4 ML CdS shelled sequence, we performed power dependent PL measurements for 1-4 ML of HgS. Each sample showed a strong biexciton component with a sub 100 ps lifetime, but also showed longer fast components with lifetimes of ~ 2 and ~ 20 ns. The cause of the longer fast components is shown to likely be due to charging of the QDs, with the most strong evidence for this coming from the saturation behavior of the charging component amplitudes as well as the fact that the high-fluence charged components match up almost perfectly with the low-fluence dynamics of the 2
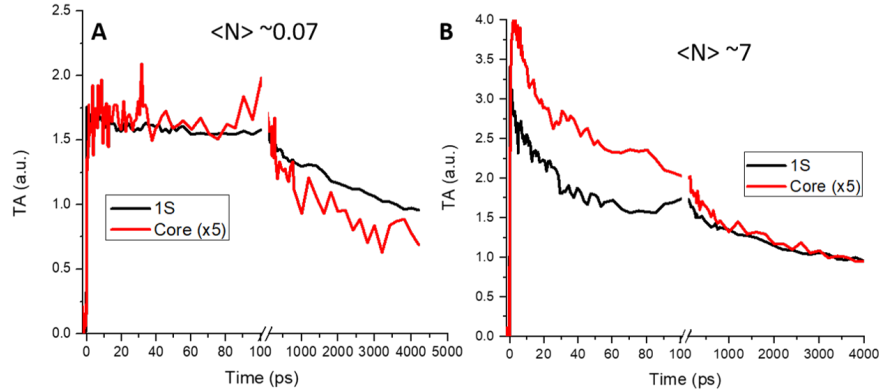
Figure 4.11: TA at low fluence (A) and high fluence (B) when pumping the system resonantly at 1.75 eV (710 nm). The core feature is seen even at low fluences. The decays are similar in short time but not long time at low excitation powers and at high excitation powers the dynamics are similar though the core short time amplitude is much more pronounced.

ML CdS series.

We looked at the core emission and showed that the dynamics there are consistent with fast radiative relaxation during relaxation to the HgS well. The emission from the core was found to be ~1% that of the main HgS peak, and did not increase drastically with power. TA data showed that the core PL is intrinsic to the ground state of the system as it was observed even when pumping the system resonantly at low powers. The core absorption bleach at 400 nm excitation had a fast component of 750 fs, quantifying the electron relaxation time to the 1S state in the HgS well. Future work will examine the TA data more thoroughly and carefully relate the results back to the PL dynamics.

4.4   Acknowledgements

This work is under preparation for submission to a suitable journal.

Chapter 5

Single Photon Emission from CdSe/HgS(1)/CdS Quantum Dots

In this final chapter we will explore the use of the aforementioned CdSe/HgS/CdS QDs as single photon emitters (SPE). Here we will limit ourselves to the 1 ML HgS sample and vary the thickness of the CdS outer shell. We will show fast single-exponential decay dynamics, excellent anti-bunching indicating the applicability of these dots as SPEs, and reduced blinking with thicker CdS shells.

5.1   History

Single photons are ideal sources for the transportation of information; they are indivisible and their quantum state cannot be cloned [229]. The act of receiving or not receiving a photon can be recorded as a binary qubit with the information potentially secure secure over arbitrary distances. Moreover, photons can be used in quantum key distribution (QKD), a secure communication based on components of quantum mechanics with allows two parties to produce a shared secret key known only to them. The first and most famous example of a QKD is BB84, named after C. Bennet and G. Brassard who developed the scheme in 1984 [230], which uses a private quantum channel and

public classical channel to provably share information securely.

Prior to studying QKD from photonic sources first one needs an ideal source of an SPE. The first SPEs were lasers which were heavily attenuated until they reached the point where the average photon per cycle was much less than one. However, the number of photons in each pulse is described by Poissonian statistics so this is not a perfect source of single photons. Epitaxial QDs have been heavily investigated as use for SPEs and show great promise at cryogenic temperatures. Their large sizes of ~50 nm (large in the sense that they are not in the quantum confinement regime) means their energy-level spacing is small so that at room temperature the systems are non-emissive. This makes practical applications more difficult, as QDs must be cooled to ~4 K prior to efficient single photon emission.

Colloidal QDs are thus ideal to use as SPEs as they have all of the advantages of epitaxial QDs plus the huge benefit of a large separation of electronic states due to quantum confinement. The study of single QDs has numerous uses in addition to being used as SPEs because single QD studies reveal vital information into intrinsic linewidths and radiative processes of QDs that are obscured in ensemble results. On this note colloidal QDs have been extensively studied at the single QD level over the past 25 years [172, 231] and many of the advances and understandings made there may be directly applied to our QDs.

5.1.1 Quantifying Single Photon Emission

To quantify the degree or quality of single photon emission the Hanbury-Brown and Twiss (HBT) technique is employed (figure 5.1A). In the HBT technique a stream of photons, in this case emitted from QDs, is incident on a 50/50 beamsplitter, such as a half-silvered mirror, which splits the incident photon stream into two different paths. Both of these beams then go to photodetectors (commonly Si amplified photodetectors (APD)) and the arrival times of the photons on each detector is recorded along with the trigger time of the excitation source. Then photon correlations are done on the arrival times of the photons of the two APDs as a function of time.

For a continuum of photons, such as from a continuous wave (CW) laser or a lamp, the number of photons is large so that the beamsplitter merely sends half of the input one way and half the other way. At the single photon level things get much more

interesting: a photon incident on the beamsplitter *must* end up along one path after the beamsplitter. Therefore for a single photon source only one of the detectors registers a photon in any given excitation cycle.

The second-order correlation function is defined as

$$g^2(\tau) = \frac{\langle I_1(t) I_2(t+\tau) \rangle}{\langle I_1(t) \rangle \langle I_2(t+\tau) \rangle} \tag{5.1}$$

where I_1 and I_2 are the signal intensities on the two APDs, t is the arrival time of the photons and τ is the repetition rate of the pulsed excitation source. g^2 serves to quantify the degree of 'singleness' from a single photon emitter. $g^2 = 0$ indicates perfect single photon emission while $g^2 = 1$ indicates perfectly classical emission where the probability of measuring two photons in a single pulse is the same as measuring photons in adjacent pulses.

A simulated g^2 profile is shown for a classical pulsed light source and a perfect single photon source in figure 5.1B,C, excited at an arbitrary repetition rate of 2 MHz and a single exciton lifetime of 20 ns. The side peaks correspond to a photon being detected at APD 1 on one pulse cycle with APD 2 detecting a photon at the previous excitation cycle or the next excitation cycle (peaks at ± 500 ns) while the peaks at 1000 ns correspond to a photon being detected at APD 1 two cycles before/after a photon is detected at APD 2. The amplitude of the $t = 0$ peak corresponds to the probability that two photons were detected within a single excitation cycle, is the what is absent when studying SPEs in the HBT system. Figure 5.1B corresponds to a classical light source where the probability of detecting multiple photons from a single pulse is the same as detecting photons excited by adjacent pulses while 5.1C represents a perfect SPE in which two photons from a single pulse are never recorded on the detectors. The $g^2(0)$ value is found by integrating all of the peaks and calculating the ratio of the area under the central peak over that of the side peaks. Typically, the area of the different side peaks is averaged to give a more accurate value.

The situation in 5.1C represents an ideal SPE but in practice QDs will always have some biexciton emission leading to a small peak at $t = 0$. The photon absorption process is treated as Poissonian, as was done chapter 4. The probability of finding a QD in the Nth excitonic state, with an average of $\langle N \rangle$ excitons per dot, is $P(N, \langle N \rangle) = \langle N \rangle^N e^{-\langle N \rangle} / N!$. Hence, even with $\langle N \rangle = 0.2$, the probability that a QD has a biexciton
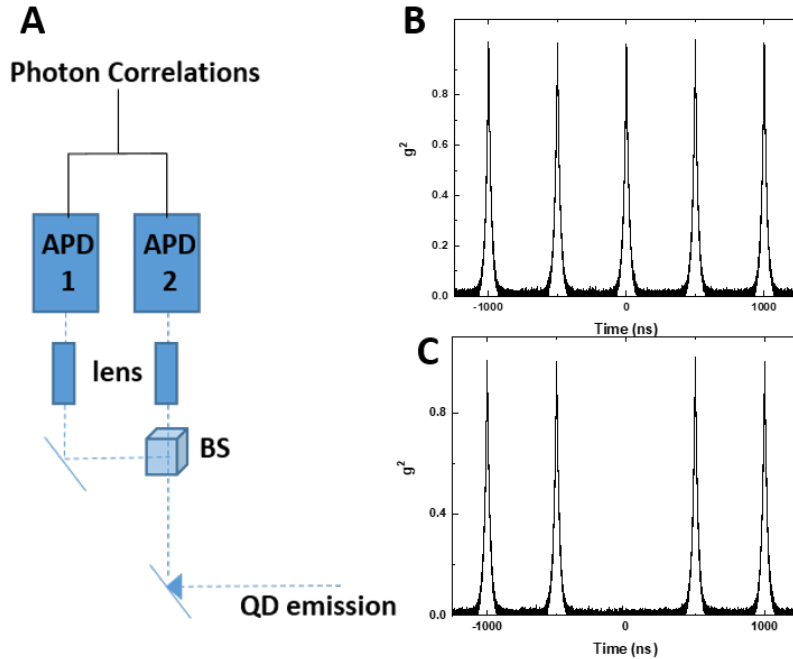
Figure 5.1: A) Schematic of the Hanbury-Brown and Twiss setup. APDs 1 and 2 time tag all photons and are synced with the pulse trigger of the diode laser. B/C) Simulated g^2 measurement using a 2 MHz repetition rate. A) Non-single photon source. The peak at t=0 indicates the probability of 2 photons arriving to the detectors at the same time is the same as 2 photons arriving on adjacent pulses. C) Simulated g^2 of a perfect single photon source. The lack of a peak at t=0 indicates that 2 photons from the same pulse train are never emitted.

is still .016, far from negligible. This leads to a finite $g^2(0)$ peak even for SPEs; $g^2(0)$ < 0.5 is defined as the cutoff for single photon emission though for QDs $g^2(0)$ is often much less than 0.1.

In the previous chapter it was seen that non-radiative Auger process dominates over biexciton emission in CdSe/HgS/CdS QDs. This leads to the measured $g^2(0)$ peak being even less than the probability a QD has a biexciton because many of these biexcitons do not decay radiatively. The Bawendi group used this fact to argue that the $g^2(0)$ value is proportional to the biexciton QY divided by the exciton QY [232], so that $g^2(0) \propto \frac{\Phi_{BX}}{\Phi_X}$, where Φ is the QY and BX, X denote biexciton and exciton respectively. Therefore the $g^2(0)$ measurement together with the enesmble QY may be used to determine the BX

QY. In certain applications, such as lasers or LEDs, a high BX QY is required in order for stimulated emission or high injection currents to be possible. For single photon emitter applications a low BX QY is desired as it leads to a greatly reduced $g^2(0)$ value. For quantum applications this leads to a catch-22 of sorts where single photon emission is necessary but the cause of low BX QY, fast Auger recombination, would destroy any chance of long-term coherence of the system.

Fortunately, 'Auger-suppression' has been developed in CdSe/CdS QDs, and other QDs, by alloying the core/shell interface. This leads to an increase in the $g^2(0)$ value [233] (though still below 0.2) but serves to create nearly non-blinking QDs with the possibility for increased coherence times. Recent work measured the coherence time of perovskite QDs at 3.6 K to be 80 ps, a significant fraction of the low temperature radiative lifetime of 210 ps [234]. Future work will measure coherence times in graded CdSe/CdS QD systems as well as in CdSe/HgS/CdS QDs.

5.2   Results

We measured single QD emission and dynamics for the 1 ML HgS QD with 2, 4 and 6 ML of CdS shelling. The concentrations of QDs dispersed in hexane is diluted from that used for ensemble studies by ∼500,000 prior to dropcasting onto a glass slide. The samples are excited with a diode laser at 488 nm and the emitted light is sent to an HBT setup as in figure 5.1A or to a spectrometer. Detailed description of the experimental setup is provided in the methods section. The two APDs in the HBT setup time-tag the arrival of each photon on each detector enabling photon-correlation measurements to be done as a function of time or intensity.

The intensity versus time trajectories are shown in figure 5.2 for zb-CdSe/HgS(1) QDs coated with 2, 4 or 6 MLs of CdS. This is done by summing the photon counts on both APDs with a 40 ms bin time over a period of 5 minutes. The 2 ML CdS sample shows very strong intermittency in the intensity as a function of time. This process is known as 'blinking' and is due to the QD switching between a bright 'on' state and a dark 'off' state [235]. The mid-level states may be attributed to a finite binning time so that some of the 'on' states are not fully captured in the 40 ms window due to the fast blinking [236]. Blinking arises from from the escape of charge carriers to the QD

surface [231]. If one charge carrier is trapped a charged QD remains, resulting in fast non-radiative Auger upon the re-excitation of the QD. If both charge carriers are trapped then no photon is emitted as the electron-hole pair is quenched during thermalization prior to relaxation to the bandedge. Based on our previous studies of PL dynamics in ensemble CdSe/HgS/CdS QDs with various CdS thicknesses we presume that the cause of the fast blinking here is due to charging of the QD leading to dominant Auger processes which limit the QY of the sample.
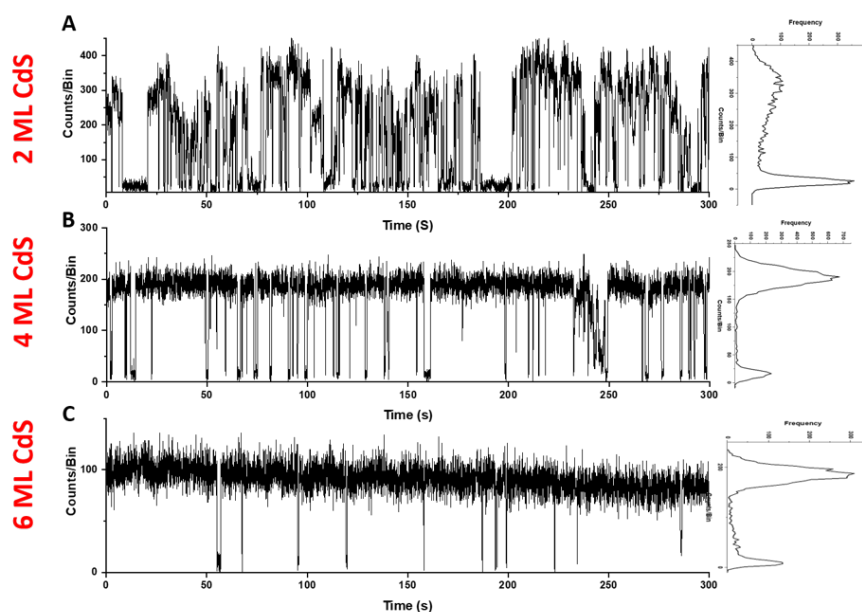
Figure 5.2: Blinking trajectories (left) and frequency histograms (right) of Cd-Se/HgS(1)/CdS(x) with x equal to A) 2 ML B) 4 ML C) 6 ML. The thicker shells heavily suppress blinking, leading to 'on' times of greater than 95% in the 6 ML CdS shelled sample. Here the binning time is 40 ms and the collection time 5 minutes for each sample.

Indeed, going from 2 ML CdS to 4 or 6 ML of CdS results in a drastic reduction in the blinking of the QD, akin to the reduction in the fast component of the PL dynamics in figure 3.11B. The 6 ML sample is in the 'on' state greater than 90% of the time indicating it would be an excellent SPE. Reduced blinking with increasing shell thickness has long been observed in CdSe/CdS QDs and an onset in blinking suppression has been observed at 4 ML CdS [237], in excellent agreement with our results. At thinner CdS

shell layers the electrons or holes can still efficiently tunnel through the CdS barrier to surface defects while thicker CdS shells suppress this tunnelling exponentially. In giant CdSe/CdS QD systems shell thicknesses can be grown out to 16-20 ML [177, 237], far beyond our current synthetic capabilities for CdSe/HgS/CdS QDs. However, such a drastic increase in the photo-stability of these NIR QDs with 'only' 4 or 6 ML of CdS bodes well for even thicker shelled CdSe/HgS/CdS systems where blinking would likely be completely suppressed and QYs would approach 100%.
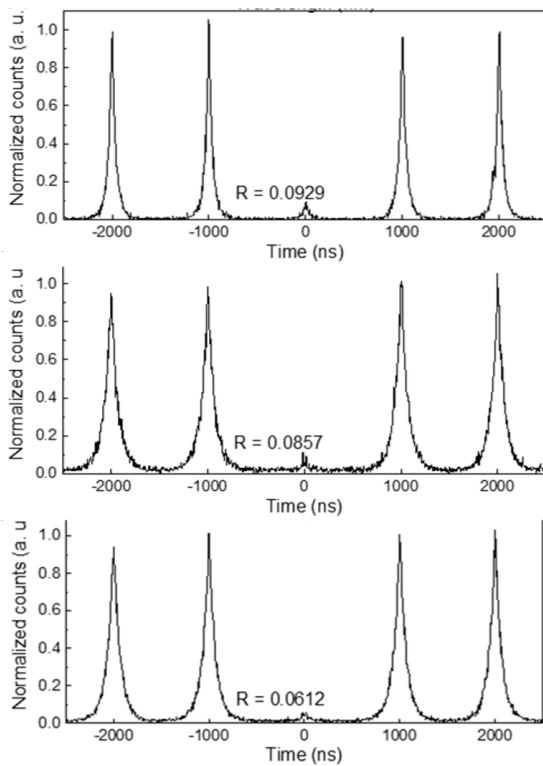
Figure 5.3: Second order photon correlation measurements for three of the 1 ML HgS 6 ML CdS QDs. The $g^2(0)$ value is less than 0.1 for each sample, indicating near optimal single photon emission.

The QDs exhibit excellent anti-bunching with $g^2(0)$ values of less than 0.1. Data for 3 separate QDs is shown in figure 5.3. Each shows only a small, barely discernable peak corresponding to 2-photon emission. Base on measurements in the previous chapter the BX lifetime much faster than their radiative lifetimes so it is not unexpected that we

have such low $g^2(0)$ values. We have not performed g^2 measurements for the thicker HgS MLs but there is no reason to expect them not to exhibit similar values of $g^2(0)$. Hence, CdSe/HgS/CdS are well poised to be used as SPEs in the NIR spectrum.

Next we examine the single QD emission spectra, focusing on the CdSe/HgS/CdS(4) QDs though the 2 and 6 ML CdS samples show analogous emission characteristics. The ensemble (a thick film dropcast onto a glass substrate and studied in the single QD setup) emission spectra is peaked at 1.67 eV (745 nm) and has a FWHM of 141 meV (63 nm) when fitted by a Gaussian, as shown in figure 5.4A. Superimposing over this several different single QD emission spectra (figure 5.4B) reveals that the single QD emission peaks are centered near the ensemble peak and have FWHM of approximately half that of the ensemble spectrum. This is shown most clearly in figure 5.4C where the FWHM versus peak emission energy is plotted for $\sim$20 different QDs. The FWHM varies from $\sim$50 meV to $\sim$100 meV with most being around $\sim$75 meV, more than half that of the ensemble PL spectrum. The red data point in figure 5.4C is that of the ensemble emission spectrum for a dropcast film. There is no observable sensitivity on FWHM to the emission peak for these QDs.
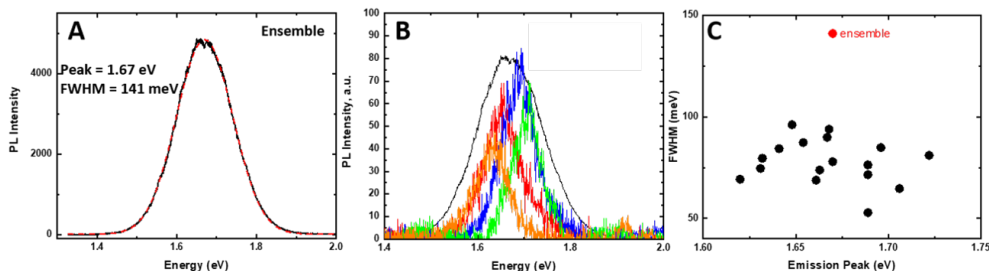
Figure 5.4: Single QD spectra of CdSe/HgS(1)/CdS(4) QDs. A) Ensemble PL spectra of a dropcast film. B) Single QD spectra superimposed over the ensemble spectra. Color is used only for clarity. C) FWHM as a function of emission peak for a variety of single QDs. Red data point is the ensemble sample.

Bare CdSe QDs can have ensemble PL linewidths as low as 96 meV, and can be reduced to 67 meV with a CdS shell [238]. CdSe/CdS single QDs have linewidths of 50-70 meV [239], in general agreement with our results here, though our ensemble broadening is more pronounced than theirs. Due to the ML control over HgS thickness, the broadening must come from either the CdSe core or CdS shells. Still, emission linewidths of

~75 meV for an NIR material is quite remarkable. State-of-the-art $CdSe/Cd_xZn_{1-x}Se$ asymmetrically strained QDs have sub-thermal linewidths of < 20 meV [186]. Applying such techniques, as well as an alloyed shell [22], to our samples here might lead to near room-temperature linewidths. The cause of the $\sim3k_BT$ linewidth of the CdSe/HgS/CdS QDs is unknown. Studying the samples as a function of temperature will reveal information about the phonon broadening of the system. An HgS ML will experience great strain upon contraction of the CdSe core with reduced temperature; the effect of this on emitting characteristics will be interesting but is beyond the scope of this thesis. The FWHM of the thicker HgS MLs has not been measured at the single QD level at this time, but in chapter 3 the ensemble steady-state PL linewidths systematically decreased with increasing HgS widths for both the zb and w crystal structures.

To better characterize these materials, we measured the time-binned lifetime as a function of time as well as the counts/bin. The resulting graphs show excellent overlap (figure 5.5A) with the PL lifetime in the 'on' state being nearly constant at 80 ns while the 'off' periods show a greatly reduced lifetime. In figure 5.5C the 'on' state decay, represented by the shaded red region in figure A, and the 'off' state decay, represented by the shaded grey box in figure A, are shown for a 4 ML CdS sample. The 'on' state shows a single exponent decay with a lifetime of 75 ns, while the off state has a fast decay of 3 ns. The 'off' state corresponds to weak glass emission, as has been shown previously [240]. The fluorescence lifetime-intensity distribution (FLID) indicates these dots do not show a strong second emission and are characterized by a single 'on' state (figure 5.5B).

Statistics of the 'on' fraction and lifetime distribution for the 4 ML CdS and 6 ML CdS shelled QDs is shown in figure 5.6. The 'on' fraction clearly increases when going from 4-6 ML of CdS, with the 6 ML CdS exhibiting the 'ceiling effect' with most of the dots nearly 100% on. The 4 ML CdS QDs show more of a bimodal distribution with a peak of 50-60% on and another peak of 80-90%. The 4 ML CdS series also shows a bimodal distribution of the average lifetime, with 2 fractions having lifetimes of ~60 ns and ~90 ns, while the 6 ML CdS series has a more symmetric single-peaked distribution of lifetimes with an average lifetime of 59 ns. The narrower distributions and higher average 'on' time can be attributed to the higher quality of QDs with the 6 ML CdS shell. The average on percentage increases from 49% for the 2 ML CdS QDs
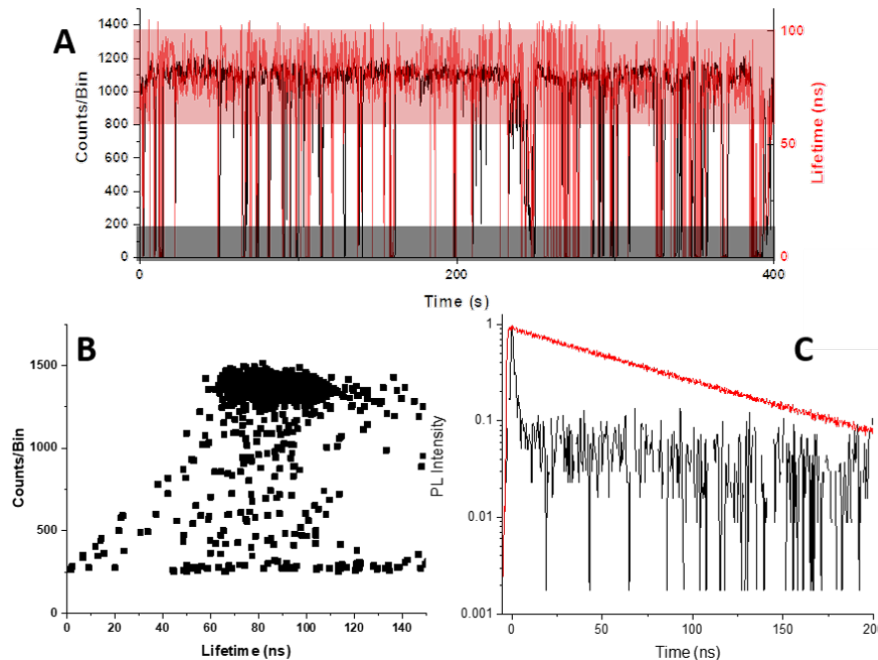
Figure 5.5: A) PL lifetime and intensity as function of time for a CdSe/HgS(1)/CdS(4) sample. B) fluorescence lifetime-intensity distribution for same dot as in (A). C) Lifetime of 'on' state, red, and 'off' state, black, based on shaded regions in (A).

(not shown) to 64% for the 4 ML CdS QDs and finally 83% for the 6 ML CdS dots. Clearly the cause of reduced QY in the thinner CdS shelled samples is due to strong blinking of the QDs.

The average lifetimes for the 4 ML CdS is ∼80 ns in good agreement with the radiative lifetime of the CdSe/HgS(1)/CdS(4) sample as seen in table 3.2. The average lifetime of the 6 ML CdS series is 59.1 ns, nearly coincident with the measured ensemble radiative lifetime of 58 ns (table 3.2). Such close alignment gives validity to the measured ensemble radiative lifetimes, though the cause of the increasing lifetime with increasing electron-hole overlap is still unknown as it is contrary to equation 3.1.

5.3 Conclusions

In this chapter we have explored preliminary use of CdSe/HgS/CdS QDs as single photon sources. Thicker CdS shells were found to greatly suppress the blinking of
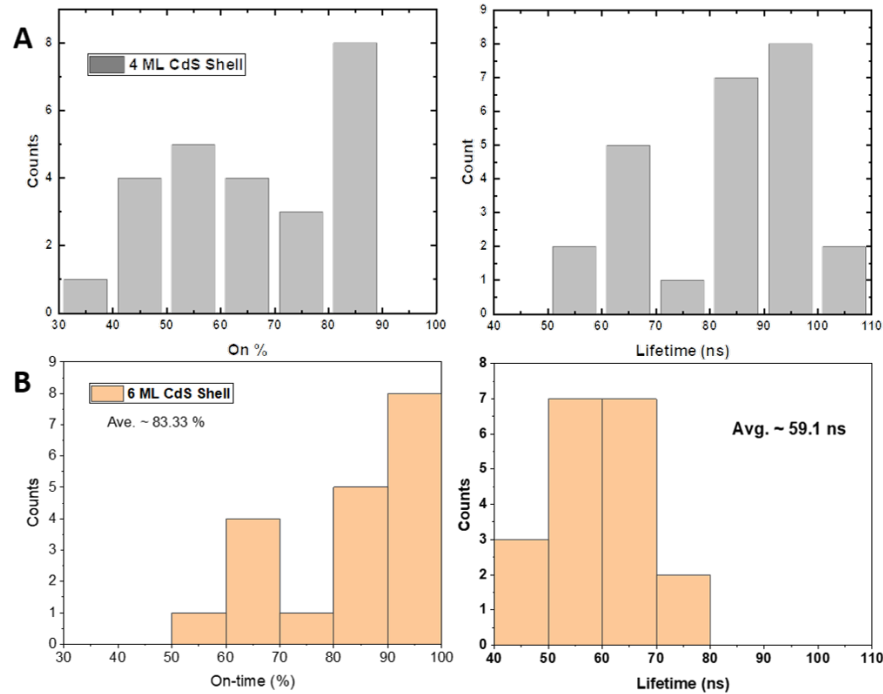
Figure 5.6: Histograms of on% and lifetime for numerous 1 ML HgS QDs with A) 4 ML CdS and B) 6 ML CdS shells.

the QDs just as in CdSe/CdS QDs. Together, these results indicate that many of the synthetic techniques applied to CdSe/CdS to increase their single photon optical properties should also be applied to CdSe/HgS/CdS as well. $g^2(0)$ values of less than 0.1 were consistently seen and linewidths were on the order of 75 meV, about half that of the ensemble spectrum.

Having established the use of CdSe/HgS/CdS as SPEs, future work will focus on their more interesting quantum photonic properties, studying such effects as low temperature single QD emission, coupling CdSe/HgS/CdS QDs to NIR optical cavities, and studying Hong-Ou-Mandel interference [241, 242] in order to quantify the coherence of optical states in this system. The results of this chapter, and the results of the previous two chapters, show clearly the great quality and potential for CdSe/HgS/CdS QDs.

5.3.1 Methods

The single QD measurements were performed on a home-built confocal fluorescence microscope system [186]. The samples were dropcast onto glass substrates from hexane after dilution of ∼500,000 over that of a sample for ensemble optical studies. Pulsed (1 MHz) or CW 488 nm laser was used for excitation, coupled to the sample using a 100X air-objective lens (numerical objective 0.9) with a 1 mm working distance. This objective was used both for focusing the laser beam onto the sample and for collecting the emitted PL. PL lifetimes, g^2 and FLID measurements were measured using a time-correlated photon counting setup in the HBT configuration with two silicon avalanche photodiode detectors (time resolution ∼350 ps).

The PL emission was measured on an optical grading spectrometer using a CCD camera. Integration times were 5 ns for each PL spectrum, and the samples were excited with a CW 488 nm pulse from the same diode laser used for the APD measurements. All measurements were done at room temperature and ambient conditions.

5.3.2 Acknowledgements

References

[1] Charles Kittel. *Introduction to Solid State Physics*. Wiley, 8th edition, 2005.

[2] Neil W. Ashcroft and David N. Mermin. *Solid State Physics*. Cengage Learning, 1976.

[3] Boris I. Shklovskii and A. L. Efros. *Electronic Properties of Doped Semiconductors*. Springer Series in Solid-State Sciences, vol. 45, 1984.

[4] J. Bardeen and W. H. Brattain. The Transistor, A Semi-Conductor Triode. *Physical Review*, 74:230–231, 1948.

[5] A. Ekimov and A. Onushchenko. Quantum size effect in three-dimensional microscopic semiconductor crystals. *Soviet Journal of Experimental and Theoretical Physics Letters*, 34(August 1981):345, 1981.

[6] Gang Wang, et al. Colloquium: Excitons in atomically thin transition metal dichalcogenides. *Reviews of Modern Physics*, 90(2):1–25, 2018.

[7] Michel Nasilowski, Benoit Mahler, Emmanuel Lhuillier, Sandrine Ithurria, and Benoit Dubertret. Two-Dimensional Colloidal Nanocrystals. *Chemical Reviews*, 116(18):10934–10982, 2016.

[8] István Robel, Bruce A. Bunker, Prashant V. Kamat, and Masaru Kuno. Exciton recombination dynamics in CdSe nanowires: Bimolecular to three-carrier auger kinetics. *Nano Letters*, 6(7):1344–1349, 2006.

[9] Daniel Vakulov, et al. Ballistic Phonons in Ultrathin Nanowires. *Nano Letters*, 2020.

[10] Victor I. Klimov. *Nanocrystal Quantum Dots, Second Edition*. CRC Press, 2010.

[11] Alexander L. Efros and A. L. Efros. Interband Light Absorption in Semiconductor Spheres. *Soviet Physics Semiconductors USSR*, 16(July 1982):772–775, 1982.

[12] Robert S. Knox. *Theory of Excitons*. Academic Press, 1963.

[13] Jeffrey M. Pietryga, et al. Spectroscopic and device aspects of nanocrystal quantum dots. *Chemical Reviews*, 116(18):10513–10622, 2016.

[14] C. B. Murray, David J. Norris, and Moungi G. Bawendi. Synthesis and Characterization of Nearly Monodisperse CdE (E = S, Se, Te) Semiconductor Nanocrystallites. *Journal of the American Chemical Society*, 115(19):8706–8715, 1993.

[15] A. I. Ekimov, et al. Absorption and intensity-dependent photoluminescence measurements on CdSe quantum dots: assignment of the first electronic transitions. *Journal of the Optical Society of America B*, 10(1):100–107, 1993.

[16] L. E. Brus. Electron-electron and electron-hole interactions in small semiconductor crystallites: The size dependence of the lowest excited electronic state. *The Journal of Chemical Physics*, 80(9):4403–4409, 1984.

[17] Felix Bloch. Über die Quantenmechanik der Elektronen in Kristallgittern. *Zeitschrift für Physik*, 52(7-8):555–600, 1929.

[18] Christophe Galland, et al. Dynamic Hole Blockade Yields Two-Color Quantum and Classical Light from Dot-in-Bulk Nanocrystals. *Nano Letters*, 13(1):321–328, 2012.

[19] Jaehoon Lim, Young-Shin Park, and Victor I. Klimov. Optical gain in colloidal quantum dots achieved with direct-current electrical pumping. *Nature Materials*, 17(1):42–48, 2018.

[20] L. Spanhel, H. Weller, A. Fojtik, and A. Henglein. Photochemistry of Semiconductor Colloids. 17. Strong luminescing CdS and CdS-Ag2S Particles. *Berichte der Bunsengesellschaft/Physical Chemistry Chemical Physics*, 91(2):88–94, 1987.

[21] David A Hanifi, et al. Redefining near-unity luminescence in quantum dots with photothermal threshold quantum yield. *Science*, 363(March):1199–1202, 2019.

[22] Oleg V. Kozlov, et al. Sub-single-exciton lasing using charged quantum dots coupled to a distrubuted feedback cavity. *Science*, 365(August):672–675, 2019.

[23] Claudiu M. Cirloganu, et al. Enhanced carrier multiplication in engineered quasi-type-II quantum dots. *Nature Communications*, 5(1):1–8, 2014.

[24] L. Esaki and R. Tsu. Superlattice and Negative Differential Conductivity in Semiconductor. *IBM Journal of Research and Development*, 14(1):61–65, 1970.

[25] A. Y. Cho and J. R. Arthur. Molecular beam epitaxy. *Progress in Solid State Chemistry*, 10(PART 3):157–191, 1975.

[26] Manfred Bayer. Bridging Two Worlds: Colloidal versus Epitaxial Quantum Dots. *Annalen der Physik*, 531(6):1–25, 2019.

[27] C. B. Murray, Cherie R. Kagan, and Moungi G. Bawendi. Synthesis and Characterization of Monodisperse Nanocrystals and Close-Packed Nanocrystal Assemblies. *Annu. Rev. Mater. Sci.*, 30:545–610, 2000.

[28] Uwe R. Kortshagen. Nonthermal plasma synthesis of semiconductor nanocrystals. *Journal of Physics D: Applied Physics*, 42(11), 2009.

[29] Uwe R. Kortshagen, et al. Nonthermal plasma synthesis of nanocrystals: Fundamental principles, materials, and applications. *Chemical Reviews*, 116(18):11061–11127, 2016.

[30] Yuan Pu, Fuhong Cai, Dan Wang, Jie Xin Wang, and Jian Feng Chen. Colloidal Synthesis of Semiconductor Quantum Dots toward Large-Scale Production: A Review. *Industrial and Engineering Chemistry Research*, 57(6):1790–1802, 2018.

[31] Jennifer A. Hollingsworth. Semiconductor Nanocrystal Quantum Dots. *Encyclopedia of Inorganic Chemistry*, 2006.

[32] Guanying Chen, Jangwon Seo, Chunhui Yang, and Paras N. Prasad. Nanochemistry and nanomaterials for photovoltaics. *Chemical Society Reviews*, 42(21):8304–8338, 2013.

[33] Patrick Felbier, et al. Highly luminescent ZnO quantum dots made in a nonthermal plasma. *Advanced Functional Materials*, 24(14):1988–1993, 2014.

[34] Katelyn S. Schramke, Yunxiang Qin, Jacob T. Held, K. Andre Mkhoyan, and Uwe R. Kortshagen. Nonthermal plasma synthesis of titanium nitride nanocrystals with plasmon resonances at near-infrared wavelengths relevant to photothermal therapy. *ACS Applied Nano Materials*, 1(6):2869–2876, 2018.

[35] Lorenzo Mangolini, Elijah Thimsen, and Uwe R. Kortshagen. High-Yield Plasma Synthesis of Luminescent Silicon Nanocrystals. *Nano Letters*, 5(4):655–659, 2005.

[36] Lorenzo Mangolini and Uwe R. Kortshagen. Plasma-Assisted Synthesis of Silicon Nanocrystal Inks. *Advanced Materials*, 19:2513–2519, 2007.

[37] Rebecca J. Anthony, David J. Rowe, Matthias Stein, Jihua Yang, and Uwe R. Kortshagen. Routes to achieving high quantum yield luminescence from gas-phase-produced silicon nanocrystals. *Advanced Functional Materials*, 21(21):4042–4046, 2011.

[38] Jeslin J. Wu and Uwe R. Kortshagen. Photostability of thermally-hydrosilylated silicon quantum dots. *RSC Advances*, 5(126):103822–103828, 2015.

[39] Kai Xie, et al. Quasi continuous wave laser sintering of Si-Ge nanoparticles for thermoelectrics. *Journal of Applied Physics*, 123(9):0–7, 2018.

[40] Chad A. Beaudette, Xiaojia Wang, and Uwe R. Kortshagen. Nanocrystal-based inorganic nanocomposites: A new paradigm for plasma-produced optoelectronic thin films. *Plasma Processes and Polymers*, e2000002:1–9, 2020.

[41] Lance M. Wheeler, Nathan R. Neale, Ting Chen, and Uwe R. Kortshagen. Hypervalent surface interactions for colloidal stability and doping of silicon nanocrystals. *Nature Communications*, 4:1–10, 2013.

[42] David J. Rowe, Jong Seok Jeong, K. Andre Mkhoyan, and Uwe R. Kortshagen. Phosphorus-doped silicon nanocrystals exhibiting mid-infrared localized surface plasmon resonance. *Nano Letters*, 13(3):1317–1322, 2013.

[43] Nicolaas J. Kramer, Katelyn S. Schramke, and Uwe R. Kortshagen. Plasmonic Properties of Silicon Nanocrystals Doped with Boron and Phosphorus. *Nano Letters*, 15(8):5597–5603, 2015.

[44] Katharine I. Hunter, Nicholas Bedford, Katelyn Schramke, and Uwe R. Kortshagen. Probing Dopant Locations in Silicon Nanocrystals via High Energy X-ray Diffraction and Reverse Monte Carlo Simulation. *Nano Letters*, 20:852–859, 2020.

[45] Jaehoon Lim, Young-Shin Park, Kaifeng WU, Hyeong Jin Yun, and Victor I. Klimov. Droop-Free Colloidal Quantum Dot Light-Emitting Diodes. *Nano Letters*, 18(10):6645–6653, 2018.

[46] Yu Ho Won, et al. Highly efficient and stable InP/ZnSe/ZnS quantum dot light-emitting diodes. *Nature*, 575(7784):634–638, 2019.

[47] Victor I. Klimov. Optical nonlinearities and ultrafast carrier dynamics in semiconductor nanocrystals. *Journal of Physical Chemistry B*, 104(26):6112–6123, 2000.

[48] Wan Ki Bae, et al. Controlling the influence of Auger recombination on the performance of quantum-dot light-emitting diodes. *Nature Communications*, 4(1):1–8, 2013.

[49] Nobuhiro Fuke, et al. CdSe quantum-dot-sensitized solar cell with ???100% internal quantum efficiency. *ACS Nano*, 4(11):6377–6386, 2010.

[50] Weyde M.M. Lin, et al. Simulating nanocrystal-based solar cells: A lead sulfide case study. *Journal of Chemical Physics*, 151(24), 2019.

[51] Richard D. Schaller and Victor I. Klimov. High Efficiency Carrier Multiplication in PbSe Nanocrystals. *Physical Review Letters*, 92(18):186601, 2004.

[52] Markus Karl, et al. Flexible and ultra-lightweight polymer membrane lasers. *Nature Communications*, 9(1), 2018.

[53] Francesco Meinardi, et al. Highly efficient luminescent solar concentrators based on earth-abundant indirect-bandgap silicon quantum dots. *Nature Photonics*, 11(3):177–185, 2017.

[54] Moon Kee Choi, Jiwoong Yang, Taeghwan Hyeon, and Dae-Hyeong Kim. Flexible quantum dot light-emitting diodes for next-generation displays. *npj Flexible Electronics*, 2(1):1–14, 2018.

[55] Alicia J. Kollár, Mattias Fitzpatrick, and Andrew A. Houck. Hyperbolic lattices in circuit quantum electrodynamics. *Nature*, 571(7763):45–50, 2019.

[56] Francesco Meinardi, et al. Large-area luminescent solar concentrators based on Stokes-shift-engineered nanocrystals in a mass-polymerized PMMA matrix. *Nature Photonics*, 8(5):392–399, 2014.

[57] Matthew R. Bergren, et al. High-Performance CuInS2 Quantum Dot Laminated Glass Luminescent Solar Concentrators for Windows. *ACS Energy Letters*, 3(3):520–525, 2018.

[58] Iacopo Carusotto, et al. Photonic materials in circuit quantum electrodynamics. *Nature Physics*, 16(3):268–279, 2020.

[59] Frank Arute, et al. Quantum supremacy using a programmable superconducting processor. *Nature*, 574(OCTOBER), 2019.

[60] Charles Santori, Matthew Pelton, Glenn Solomon, Yseulte Dale, and Yoshihisa Yamamoto. Triggered single photons from a quantum dot. *Physical Review Letters*, 86(8):1502–1505, 2001.

[61] Haixu Leng, Brian Szychowski, Marie Christine Daniel, and Matthew Pelton. Strong coupling and induced transparency at room temperature with single quantum dots and gap plasmons. *Nature Communications*, 9(1), 2018.

[62] Brahim Lounis and Michel Orrit. Single-photon sources. *Reports on Progress in Physics*, 68(5):1129–1179, 2005.

[63] Vladimir Dobrosavljević. Introduction to Metal-Insulator Transitions. *Conductor-Insulator Quantum Phase Transitions*, 2012.

[64] D. Belitz and T. R. Kirkpatrick. The Anderson-Mott transition. *Reviews of Modern Physics*, 66(2):261–380, 1994.

[65] Masatoshi Imada, Atsushi Fujimori, and Yoshinori Tokura. Metal-insulator transitions. *Reviews of Modern Physics*, 70(4):1039–1263, 1998.

[66] S. L. Sondhi, S. M. Girvin, J. P. Carini, and D. Shahar. Continuous quantum phase transitions. *Reviews of Modern Physics*, 69(1):315–333, 1997.

[67] Lev. D. Landau. On the Theory of Phase Transitions. *Journal of Experimental and Theoretical Physics (Zh. Eksp. Teor. Fiz.)*, 7:19–32, 1937.

[68] S Bogdanovich, Myriam P Sarachik, and R. N. Bhatt. Scaling of the Conductivity with Temperature and Uniaxial Stress in Si : B at the Metal-Insulator Transition Si : B. *Physical Review Letters*, 82(1):137–140, 1999.

[69] Nigel Goldenfeld. *Lectures On Phase Transitions And The Renormalization Group*. CRC Press, Boca Raton, 1992.

[70] Arnold Sommerfeld. Zur Elektronentheorie der Metalle auf Grund der Fermischen Statistik. *Zeitschrift für Physik*, 47:1–32, 1928.

[71] Hans A. Bethe. Theorie der Beugung von Elektronen an Kristallen. *Annalen der Physik.*, 87:55, 1928.

[72] A. H. Wilson. The Theory of Electronic Semi-Conductors. *Proceedings of the Royal Society A*, 133(450), 1931.

[73] E. Wigner. On the interaction of electrons in metals. *Physical Review*, 46(11):1002–1011, 1934.

[74] E. Wigner. Effects of the electron interaction on the energy levels of electrons in metals. *Transactions of the Faraday Society*, 34:678–685, 1938.

[75] N. F. Mott. The basis of the electron theory of metals, with special reference to the transition metals. *Proceedings of the Physical Society. Section A*, 62(7):416–422, 1949.

[76] N. F. Mott. On the transition to metallic conduction in semiconductors. *Canadian Journal of Physics*, 34(12A):1356–1368, 1956.

[77] N. F. Mott. Metal-Insulator Transition. *Reviews of Modern Physics*, 40(4), 1968.

[78] Sergei Baranovskii. *Charge Transport in Disordered Solids with Applications in Electronics*. John Wiley & Sons, Inc., 2006.

[79] I. S. Beloborodov, A. V. Lopatin, V. M. Vinokur, and Konstantin B. Efetov. Granular electronic systems. *Reviews of Modern Physics*, 79(2):469–518, 2007.

[80] Melvin Cutler and N. F. Mott. Obsevation of Anderson Localization in an Electron Gas. *Physical Review*, 181(3), 1969.

[81] Gabriel Lemarié. Glassy properties of Anderson localization: pinning, avalanches and chaos. *Physical Review Letters*, 122:1–6, 2019.

[82] Mordechai Segev, Yaron Silberberg, and Demetrios N. Christodoulides. Anderson localization of light. *Nature Photonics*, 7(3):197–204, 2013.

[83] P. W. Anderson. Absence of diffusion in certain random lattices. *Physical Review*, 109(5):1492–1505, 1958.

[84] Paul Drude. Zur Elektronentheorie der Metalle. *Annalen der Physik.*, 306(3):566–613, 1900.

[85] Elihu Abrahams, P. W. Anderson, D. C. Licciardello, and T. V. Ramakrishnan. Scaling Theory of Localization: Absence of Quantum Diffusion in Two Dimensions. *Physical Review Letters*, 42(10), 1979.

[86] Brian Skinner, Tianran Chen, and Boris I. Shklovskii. Theory of hopping conduction in arrays of doped semiconductor nanocrystals. *Physical Review B*, 85(20):1–13, 2012.

[87] Allen Miller and Elihu Abrahams. Impurity conduction at low concentrations. *Physical Review*, 120(3):745–755, 1960.

[88] N. F. Mott. Conduction in non-crystalline materials. *Philosophy Magazine*, 19(160):835–852, 1969.

[89] A. L. Efros and Boris I. Shklovskii. Coulomb gap and low temperature conductivity of disordered systems. *Journal of Physics C: Solid State Physics*, 8(4), 1975.

[90] Mahdi Samadi Khoshkhoo, et al. Tunable Charge Transport in Hybrid Superlattices of Indium Tin Oxide Nanocrystals and Metal Phthalocyanines—Toward Sensing Applications. *Advanced Materials Interfaces*, 5(9):1–12, 2018.

[91] Moon Sung Kang, Ayaskanta Sahu, David J. Norris, and C. Daniel Frisbie. Size- and temperature-dependent charge transport in PbSe nanocrystal thin films. *Nano Letters*, 11(9):3887–3892, 2011.

[92] Arjan J. Houtepen, Daan Kockmann, and Daniel Vanmaekelbergh. Reappraisal of variable-range hopping in quantum-dot solids. *Nano Letters*, 8(10):3516–3520, 2008.

[93] Ting Chen, Brian Skinner, Wei Xie, Boris I. Shklovskii, and Uwe R. Kortshagen. Carrier transport in films of alkyl-ligand-terminated silicon nanocrystals. *Journal of Physical Chemistry C*, 118(34):19580–19588, 2014.

[94] Dong Yu, Congjun Wang, Brian L. Wehrenberg, and Philippe Guyot-Sionnest. Variable range hopping conduction in semiconductor nanocrystal solids. *Physical Review Letters*, 92(21):1–4, 2004.

[95] Jong Soo Lee, Maksym V. Kovalenko, Jing Huang, Dae Sung Chung, and Dmitri V. Talapin. Band-like transport, high electron mobility and high photoconductivity in all-inorganic nanocrystal arrays. *Nature Nanotechnology*, 6(6):348–352, 2011.

[96] Ruili Wang, et al. Colloidal quantum dot ligand engineering for high performance solar cells. *Energy and Environmental Science*, 9(4):1130–1143, 2016.

[97] Yao Liu, et al. Dependence of carrier mobility on nanocrystal size and ligand length in pbse nanocrystal solids. *Nano Letters*, 10(5):1960–1969, 2010.

[98] Cherie R. Kagan and Christopher B. Murray. Charge transport in strongly coupled quantum dot solids. *Nature Nanotechnology*, 10(12):1013–1026, 2015.

[99] Han Fu, K. V. Reich, and Boris I. Shklovskii. Hopping conductivity and insulator-metal transition in films of touching semiconductor nanocrystals. *Physical Review B*, 93(12):1–12, 2016.

[100] Ting Chen, et al. Metal-insulator transition in films of doped semiconductor nanocrystals. *Nature materials*, 15(November):1–6, 2015.

[101] Elijah Thimsen, et al. High electron mobility in thin films formed via supersonic impact deposition of nanocrystals synthesized in nonthermal plasmas. *Nature Communications*, 5:5822, 2014.

[102] Soong Ju Oh, et al. Designing high-performance PbS and PbSe nanocrystal electronic devices through stepwise, post-synthesis, colloidal atomic layer deposition. *Nano Letters*, 14(3):1559–1566, 2014.

[103] Deanna Lanigan and Elijah Thimsen. Contact Radius and the Insulator-Metal Transition in Films Comprised of Touching Semiconductor Nanocrystals. *ACS Nano*, 10(7):6744–6752, 2016.

[104] Benjamin E. Treml, et al. Successive Ionic Layer Absorption and Reaction for Postassembly Control over Inorganic Interdot Bonds in Long-Range Ordered Nanocrystal Films. *ACS Applied Materials and Interfaces*, 9(15):13500–13507, 2017.

[105] Qinyi Chen, Jeffrey R. Guest, and Elijah Thimsen. Visualizing Current Flow at the Mesoscale in Disordered Assemblies of Touching Semiconductor Nanocrystals. *Journal of Physical Chemistry C*, 121(29):15619–15629, 2017.

[106] Corey M. Staller, et al. Tuning Nanocrystal Surface Depletion by Controlling Dopant Distribution as a Route Toward Enhanced Film Conductivity. *Nano Letters*, 18(5):2870–2878, 2018.

[107] Kevin Whitham, et al. Charge transport and localization in atomically coherent quantum dot solids. *Nature Materials*, 15(5):557–563, 2016.

[108] Byung Hyo Kim, et al. High Mobility in Nanocrystal-Based Transparent Conducting Oxide Thin Films. *ACS Nano*, 12(4):3200–3208, 2018.

[109] Xinzheng Lan, et al. Quantum dot solids showing state-resolved band-like transport. *Nature Materials*, 19:323–329, 2020.

[110] Menglu Chen, Guohua Shen, and Philippe Guyot-Sionnest. State-Resolved Mobility of 1 cm2/(Vs) with HgSe Quantum Dot Films. *Journal of Physical Chemistry Letters*, pages 2303–2307, 2020.

[111] Konstantin V. Reich. Conductivity of Quantum Dots Array. *Physics–Uspekhi*, 63, 2020.

[112] Hans A. Bethe. Theory of diffraction by small holes. *Physical Review*, 66(7-8):163–182, 1944.

[113] N. F. Mott. The minimum metallic conductivity. *International Reviews in Physical Chemistry*, 4(1):1–18, 1985.

[114] Francesco Paglia, et al. Photonic Sintering of Copper through the Controlled Reduction of Printed CuO Nanocrystals. *ACS Applied Materials and Interfaces*, 7(45):25473–25478, 2015.

[115] T. Gebel, et al. Flash lamp annealing with millisecond pulses for ultra-shallow boron profiles in silicon. *Nuclear Instruments and Methods in Physics Research, Section B: Beam Interactions with Materials and Atoms*, 186(1-4):287–291, 2002.

[116] Bryce A. Williams, et al. Intense pulsed light annealing of copper zinc tin sulfide nanocrystal coatings. *Journal of Vacuum Science & Technology A: Vacuum, Surfaces, and Films*, 34(5):051204, 2016.

[117] Lars Rebohle, Slawomir Prucnal, and Denise Reichel. *Flash Lamp Annealing*, volume 288. Springer Series in Materials Science, 2019.

[118] Donald A. Melnick. Zinc oxide photoconduction, an oxygen adsorption process. *The Journal of Chemical Physics*, 26(5):1136–1146, 1957.

[119] Jeffrey Lindemuth and Shin-Ichiro Mizuta. Hall measurements on low-mobility materials and high resistivity materials. *Thin Film Solar Technology III*, 8110(5):81100I, 2011.

[120] Rueben J. Mendelsberg, Guillermo Garcia, and Delia J. Milliron. Extracting reliable electronic properties from transmission spectra of indium tin oxide thin films and nanocrystal films by careful application of the Drude theory. *Journal of Applied Physics*, 111(6), 2012.

[121] Otfried Madelung. *Semiconductors: Data Handbook 3rd edition.* Springer, 2004.

[122] Alina M. Schimpf, Carolyn E. Gunthardt, Jeffrey D. Rinehart, James M. Mayer, and Daniel R. Gamelin. Controlling carrier densities in photochemically reduced colloidal ZnO nanocrystals: Size dependence and role of the hole quencher. *Journal of the American Chemical Society*, 135(44):16569–16577, 2013.

[123] Ji Young Noh, Hanchul Kim, Yong Sung Kim, and C. H. Park. Electron doping limit in Al-doped ZnO by donor-acceptor interactions. *Journal of Applied Physics*, 113(15), 2013.

[124] K. Ellmer. Resistivity of polycrystalline zinc oxide films: Current status and physical limit. *Journal of Physics D: Applied Physics*, 34(21):3097–3108, 2001.

[125] Leo J. van der Pauw. A Method of Measuring the Resistivity and Hall Coefficient on Lamellae of Arbitrary Shape. *Philips Technical Review*, 13:1–9, 1958.

[126] Benjamin L. Greenberg, et al. ZnO Nanocrystal Networks Near the Insulator-Metal Transition: Tuning Contact Radius and Electron Density with Intense Pulsed Light. *Nano Letters*, 17(8):4634–4642, 2017.

[127] A G Zabrodskii and K N Zinov 'eva. Low-temperature conductivity and metal-insulator transition in compensate n-Ge. *Journal of Experimental and Theoretical Physics*, 86(February):727–742, 1984.

[128] B.L Al'thuler and A.G. Aronov. Scaling theory of Anderson's transition for interacting electrons. *JETP Letters*, 37:410–413, 1983.

[129] I. Shlimak, M. Kaveh, R. Ussyshkin, V. Ginodman, and L. Resnick. Determination of the critical conductivity exponent for the metal-insulator transition at nonzero temperatures: Universality of the transition. *Physical Review Letters*, 77(6):1103–1106, 1996.

[130] A. S. Roy, A. F. Th. Hoekstra, T. F. Rosenbaum, and R. Griessen. Quantum Fluctuations and the Closing of the Coulomb Gap in a Correlated Insulator. *Physical Review Letters*, 89(27):276402, 2002.

[131] A. Husmann, et al. Dynamical Signature of the Mott-Hubbard Transition in Ni (S , Se) $ _2 $. *Science*, 274(5294):1874–1876, 1996.

[132] Boris Shapiro and Elihu Abrahams. Scaling for the frequency-dependent conductivity in disordered electronic systems. *Physical Review B*, 24(8):4889–4891, 1981.

[133] Tsuneyoshi Nakayama, Kousuke Yakubo, and Raymond L. Orbach. Dynamical properties of fractal networks: Scaling, numerical simulations, and physical realizations. *Reviews of Modern Physics*, 66(2):381–443, 1994.

[134] Michael Schreiber and Heiko Grussbach. Dimensionality dependence of the metal-insulator transition in the Anderson model of localization. *Physical Review Letters*, 76(10):1687–1690, 1996.

[135] Yu Shi and Changde Gong. Critical dimensionalitites of phase transitions on fractals. *Physical Review E*, 49(1):99–103, 1994.

[136] Elliott W. Montroll and Michael F. Shlesinger. Maximum entropy formalism, fractals, scaling phenomena, and 1/f noise: A tale of tails. *Journal of Statistical Physics*, 32(2):209–230, 1983.

[137] Guifu Zou, et al. Fe3O4 Nanocrystals with Novel Fractal. *Journal of Physical Chemistry B*, 109(4):12356–18360, 2005.

[138] Y. Ujiie, N. Yumoto, T. Morimoto, N. Aoki, and Y. Ochiai. Fractal behaviour in graphene open quantum dot. *Journal of Physics: Conference Series*, 109(1):1–5, 2008.

[139] Fernanda Peyronel, David A. Pink, and Alejandro G. Marangoni. Triglyceride nanocrystal aggregation into polycrystalline colloidal networks: Ultra-small angle X-ray scattering, models and computer simulation. *Current Opinion in Colloid and Interface Science*, 19(5):459–470, 2014.

[140] V. S. Abramov. Quantum dots in a fractal multilayer system. *Bulletin of the Russian Academy of Sciences: Physics*, 81(5):579–586, 2017.

[141] Biao Jin, Zhaoming Liu, Ruikang Tang, and Chuanhong Jin. Quantitative investigation of the formation and growth of palladium fractal nanocrystals by liquid-cell transmission electron microscopy. *Chemical Communications*, 55(56):8186–8189, 2019.

[142] M. C. Maliepaard, M. Pepper, R. Newbury, and G. Hill. Length Scales at the Metal-Insulator Transition in Compensated GaAs. *Physical Review Letters*, 61(3):369–372, 1988.

[143] Nihar R. Pradhan, et al. Metal to Insulator Quantum-Phase Transition in Few-Layered ReS2. *Nano Letters*, 15(12):8377–8384, 2015.

[144] G. A. Thomas, M. Paalanen, and T. F. Rosenbaum. Measurements of conductivity near the metal-insulator critical point. *Physical Review B*, 27(6):3897–3900, 1983.

[145] A. L. Efros and Boris I. Shklovskii. Critical Behaviour of Conductivity and Dielectric Constant near the Metal-Non-Metal Transition Threshold. *Phys. Stat. Sol. b*, 76:475–485, 1976.

[146] Brian T Benton, Benjamin L. Greenberg, Eray S. Aydil, Uwe R. Kortshagen, and S A Campbell. Variable range hopping conduction in ZnO nanocrystal thin films. *Nanotechnology*, 29:1–8, 2018.

[147] Omid Zandi, et al. Impacts of surface depletion on the plasmonic properties of doped semiconductor nanocrystals. *Nature Materials*, 17(8):710–717, 2018.

[148] U. Zum Felde, M. Haase, and H. Weller. Electrochromism of highly doped nanocrystalline SnO2:Sb. *Journal of Physical Chemistry B*, 104(40):9388–9395, 2000.

[149] A. J. Sievers. Extinction sum rule and optical moment for an ellipsoidal particle of arbitrary size. *Optics Communications*, 109(1-2):71–74, 1994.

[150] Maxim Yu Kharitonov and Konstantin B. Efetov. Hall resistivity of granular metals. *Physical Review Letters*, 99(5):1–4, 2007.

[151] N/A. Exploring the Milky Way. *National Aeronautics and Space Administration*, 2012.

[152] T. W. Crowther, et al. Mapping tree density at a global scale. *Nature*, 525(7568):201–205, 2015.

[153] Eva Bianconi, et al. An estimation of the number of cells in the human body. *Annals of Human Biology*, 40(6):463–471, 2013.

[154] Benjamin L. Greenberg, et al. Metal-Insulator Transition in a Semiconductor Nanocrystal Network. *Science Advances*, 5:1–8, 2019.

[155] Arthur R.C. McCray, Benjamin H. Savitzky, Kevin Whitham, Tobias Hanrath, and Lena F. Kourkoutis. Orientational Disorder in Epitaxially Connected Quantum Dot Solids. *ACS Nano*, 13(10):11460–11468, 2019.

[156] Michelle A. Smeaton, Daniel M. Balazs, Tobias Hanrath, and Lena F. Kourkoutis. Quantifying Atomic-Scale Quantum Dot Superlattice Behavior Upon in situ Heating . *Microscopy and Microanalysis*, 25(S2):1538–1539, 2019.

[157] Kevin Whitham and Tobias Hanrath. Formation of Epitaxially Connected Quantum Dot Solids: Nucleation and Coherent Phase Transition. *Journal of Physical Chemistry Letters*, 8(12):2623–2628, 2017.

[158] Yun Liu, Nolan Peard, and Jeffrey C. Grossman. Bandlike Transport in PbS Quantum Dot Superlattices with Quantum Confinement. *Journal of Physical Chemistry Letters*, 10(13):3756–3762, 2019.

[159] Benjamin H. Savitzky, et al. Propagation of Structural Disorder in Epitaxially Connected Quantum Dot Solids from Atomic to Micron Scale. *Nano Letters*, 16(9):5714–5718, 2016.

[160] Yu Wang, et al. In situ TEM observation of neck formation during oriented attachment of PbSe nanocrystals. *Nano Research*, 12(10):2549–2553, 2019.

[161] Yu Wang, et al. Dynamic deformability of individual PbSe nanocrystals during superlattice phase transitions. *Science Advances*, 5(6), 2019.

[162] S. V. Kravchenko and Myriam P Sarachik. Metal–insulator transition in two-dimensional electron systems. *Reports on Progress in Physics*, 67:1, 2004.

[163] Elihu Abrahams, Sergey V Kravchenko, and Myriam P Sarachik. Colloquium: Metallic behavior and related phenomena in two dimensions. *Reviews of Modern Physics*, 73(2):251–266, 2001.

[164] Alex Abelson, et al. Collective topo-epitaxy in the self-assembly of a 3D quantum dot superlattice. *Nature Materials*, 2019.

[165] Michael A. Boles, Michael Engel, and Dmitri V. Talapin. Self-assembly of colloidal nanocrystals: From intricate structures to functional materials. *Chemical Reviews*, 116(18):11220–11289, 2016.

[166] Elihu Abrahams and G. Kotliar. The Metal-Insulator Transition in Correlated Disordered Systems. *Science*, 274(5294):1853–1854, 1996.

[167] Boris Korzh, et al. Demonstration of sub-3 ps temporal resolution with a superconducting nanowire single-photon detector. *Nature Photonics*, pages 1–6, 2020.

[168] Victor I. Klimov and Duncan W. McBranch. Femtosecond 1P-to-1S electron relaxation in strongly confined semiconductor nanocrystals. *Physical Review Letters*, 80(18):4028–4031, 1998.

[169] Volker Kuntermann, Carla Cimpean, Georg Brehm, Guido Sauer, and Carola Kryschi. Femtosecond transient absorption spectroscopy of silanized silicon quantum dots. *Physical Review B*, 77(11):1–8, 2008.

[170] Rohan Singh, Wenyong Liu, Jaehoon Lim, and Victor I. Klimov. Hot-electron dynamics in quantum dots manipulated by spin-exchange Auger interactions. *Nature Nanotechnology*, 2019.

[171] S. A. Empedocles, David J. Norris, and Moungi G. Bawendi. Photoluminescence spectroscopy of single CdSe nanocrystallite quantum dots. *Physical Review Letters*, 77(18):3873–3876, 1996.

[172] M. Nirmal, et al. Fluorescence intermittency in single cadmium selenide nanocrystals. *Nature*, 383(October):802–804, 1996.

[173] Jianhai Zhou, Meiyi Zhu, Renyang Meng, Haiyan Qin, and Xiaogang Peng. Ideal CdSe/CdS Core/Shell Nanocrystals Enabled by Entropic Ligands and Their Core Size-, Shell Thickness-, and Ligand-Dependent Photoluminescence Properties. *Journal of the American Chemical Society*, 139(46):16556–16567, 2017.

[174] Wan Ki Bae, et al. Controlled alloying of the core-shell interface in CdSe/CdS quantum dots for suppression of auger recombination. *ACS Nano*, 7(4):3411–3419, 2013.

[175] Dongzhi Yang, Qifan Chen, and Shukun Xu. Synthesis of CdSe/CdS with a simple non-TOP-based route. *Journal of Luminescence*, 126(2):853–858, 2007.

[176] Encai Hao, et al. Synthesis and Optical Properties of CdSe and CdSe / CdS. *Chemistry of Materials*, 11:3096–3102, 1999.

[177] Bhola N. Pal, et al. 'Giant' CdSe/CdS core/shell nanocrystal quantum dots as efficient electroluminescent materials: Strong influence of shell thickness on light-emitting diode performance. *Nano Letters*, 12(1):331–336, 2012.

[178] Anton V. Malko, et al. Pump-intensity- and shell-thickness-dependent evolution of photoluminescence blinking in individual core/shell CdSe/CdS nanocrystals. *Nano Letters*, 11(12):5213–5218, 2011.

[179] Young-Shin Park, et al. Near-unity quantum yields of biexciton emission from CdSe/CdS nanocrystals measured using single-particle spectroscopy. *Physical Review Letters*, 106(18):6–9, 2011.

[180] Valerio Pinchetti, et al. Effect of Core/Shell Interface on Carrier Dynamics and Optical Gain Properties of Dual-Color Emitting CdSe/CdS Nanocrystals. *ACS Nano*, 10:17, 2016.

[181] Christophe Galland, et al. Lifetime blinking in nonblinking nanocrystal quantum dots. *Nature Communications*, 3(May), 2012.

[182] Moungi G. Bawendi, M. L. Steigerwalkd, and L. E. Brus. The Quantum Mechanics Of Larger Semiconductor Clusters ("Quantum Dots". *Annual Review of Physical Chemistry*, 41(1):477–496, 1990.

[183] Ke Gong, James E. Martin, Lauren E. Shea-Rohwer, Ping Lu, and David F. Kelley. Radiative lifetimes of zincblende CdSe/CdS quantum dots. *Journal of Physical Chemistry C*, 119(4):2231–2238, 2015.

[184] Narine Moses Badlyan, Amelie Biermann, Tangi Aubert, Zeger Hens, and Janina Maultzsch. Thermal expansion of colloidal CdSe/CdS core/shell quantum dots. *Physical Review B*, 99(19):195425, 2019.

[185] Jeongkyun Roh, Young-shin Park, Jaehoon Lim, and Victor I. Klimov. Optically pumped colloidal-quantum-dot lasing in LED-like devices with an integrated optical cavity. *Nature Communications*, 11(271), 2020.

[186] Young-Shin Park, Jaehoon Lim, and Victor I. Klimov. Asymmetrically strained quantum dots with non-fluctuating single-dot emission spectra and subthermal room-temperature linewidths. *Nature Materials*, page 1, 2019.

[187] Megan K. Dunlap, et al. Super-resolution photoluminescence lifetime and intensity mapping of interacting CdSe / CdS quantum dots Super-resolution photoluminescence lifetime and intensity mapping of interacting CdSe / CdS quantum dots. *Applied Physics Letters*, 116, 2020.

[188] Yashaswi Nandan and Mohan Singh Mehata. Wavefunction Engineering of Type-I/Type-II Excitons of CdSe/CdS Core-Shell Quantum Dots. *Scientific Reports*, 9(1):1–11, 2019.

[189] M. Cardona, et al. Electronic, vibrational, and thermodynamic properties of metacinnabar β-HgS, HgSe, and HgTe. *Physical Review B*, 80(19):1–14, 2009.

[190] A. Svane, et al. Quasiparticle band structures of β-HgS, HgSe, and HgTe. *Physical Review B*, 84(20):1–6, 2011.

[191] A. Mews, Alexander Eychmüller, M. Giersig, D. Schooss, and Horst Weller. Preparation, characterization, and photophysics of the quantum dot quantum well system cadmium sulfide/mercury sulfide/cadmium sulfide. *The Journal of Physical Chemistry*, 98(3):934–941, 1994.

[192] D. Schooss, A. Mews, Alexander Eychmüller, and Horst Weller. Quantum-dot quantum well CdS/HgS/CdS: Theory and experiment. *Physical Review B*, 49(24):17072–17078, 1994.

[193] Alf Mews and Alexander Eychmüller. Quantum wells within quantum dots, a CdS/HgS nanoheterostructure with global and local confinement. *Berichte der Bunsengesellschaft/Physical Chemistry Chemical Physics*, 102(10):1343–1357, 1998.

[194] Markus Braun, Clemens Burda, and Mostafa A. El-Sayed. Variation of the thickness and number of wells in the CdS/HgS/CdS quantum dot quantum well system. *Journal of Physical Chemistry A*, 105(23):5548–5551, 2001.

[195] F. Comas and Nelson Studart. Electron-phonon interaction in quantum-dot/quantum-well semiconductor heterostructures. *Physical Review B*, 69(23):1–8, 2004.

[196] D. Dorfs, H. Henschel, J. Kolny, and Alexander Eychmüller. Multilayered nanoheterostructures: Theory and experiment. *Journal of Physical Chemistry B*, 108(5):1578–1583, 2004.

[197] Dirk Dorfs and Alexander Eychmüller. A Series of Double Well Semiconductor Quantum Dots. *Nano Letters*, 1(11):663–665, 2001.

[198] F. Benhaddou, I. Zorkani, and A. Jorio. The confinement effect in spherical inhomogeneous quantum dots and stability of excitons. *AIP Advances*, 7(6), 2017.

[199] Arthur H. Nethercot. Prediction of Fermi energies and photoelectric thresholds based on electronegativity concepts. *Physical Review Letters*, 33(18):1088–1091, 1974.

[200] M. Royo, J. Planelles, and M. Pi. Effective mass and dielectric constant mismatch effects in spherical multishell quantum dots. *Physical Review B*, 75(3):1–4, 2007.

[201] Andrei Piryatinski, Sergei A. Ivanov, Sergei Tretiak, and Victor I. Klimov. Effect of Quantum and Dielectric Confinement on the Exciton-Exciton Interaction Energy in Type II Core/Shell Semiconductor Nanocrystals. *Nano letters*, 7(1):108, 2006.

[202] Qianglu Lin, et al. Design and synthesis of heterostructured quantum dots with dual emission in the visible and infrared. *ACS Nano*, 9(1):539–547, 2015.

[203] Sandrine Ithurria and Dmitri V. Talapin. Colloidal Atomic Layer Deposition (c-ALD) using self-limiting reactions at nanocrystal surface coupled to phase transfer between polar and nonpolar media. *Journal of the American Chemical Society*, 134(45):18585–18590, 2012.

[204] J Jack Li, et al. Large-Scale Synthesis of Nearly Monodisperse CdSe/CdS Core/Shell Nanocrystals Using Air-Stable Reagents via Successive Ion Layer Adsorption and Reaction. *Journal of the American Chemical Society*, 125:12567–12575, 2003.

[205] Vladimir Sayevich, et al. Hybrid N-Butylamine-Based Ligands for Switching the Colloidal Solubility and Regimentation of Inorganic-Capped Nanocrystals. *ACS Nano*, 11(2):1559–1571, 2017.

[206] Jacek Jasieniak, Lisa Smith, Joel Van Embden, Paul Mulvaney, and Marco Califano. Re-examination of the size-dependent absorption properties of CdSe quantum dots. *Journal of Physical Chemistry C*, 113(45):19468–19474, 2009.

[207] Richard L. Sandberg, et al. Multiexciton dynamics in infrared-emitting colloidal nanostructures probed by a superconducting nanowire single-photon detector. *ACS Nano*, 6(11):9532–9540, 2012.

[208] C. H. Henry and K Nassau. Lifetimes of Bound Exitons in CdS. *Physical Review B*, 1:1628, 1970.

[209] P. D.J. Calcott, K. J. Nash, L. T. Canham, M. J. Kane, and D. Brumhead. Spectroscopic identification of the luminescence mechanism of highly porous silicon. *Journal of Luminescence*, 57(1-6):257–269, 1993.

[210] Alexander L. Efros and M Rosen. The Electronic Structure of Semiconductor Nanocrystals. *Annual Reviews of Materials Science*, 30:475–521, 2000.

[211] Peter C. Sercel, A. Shabaev, and Alexander L. Efros. Photoluminescence Enhancement through Symmetry Breaking Induced by Defects in Nanocrystals. *Nano Letters*, 17(8):4820–4830, 2017.

[212] Peter C. Sercel and Alexander L. Efros. Band-Edge Exciton in CdSe and Other II-VI and III-V Compound Semiconductor Nanocrystals - Revisited. *Nano Letters*, 18(7):4061–4068, 2018.

[213] Evan O. Kane. Band structure of indium antimonide. *Journal of Physics and Chemistry of Solids*, 1(4):249–261, 1957.

[214] W. Jaskólski and Garnett W. Bryant. Multiband theory of quantum-dot quantum wells: Dim excitons, bright excitons, and charge separation in heteronanostructures. *Physical Review B*, 57(8):R4237–R4240, 1998.

[215] Brian L. Wehrenberg, Congjun Wang, and Philippe Guyot-Sionnest. Interband and intraband optical studies of PbSe colloidal quantum dots. *Journal of Physical Chemistry B*, 106(41):10634–10640, 2002.

[216] István Robel, Ryan Gresback, Uwe R. Kortshagen, Richard D. Schaller, and Victor I. Klimov. Universal size-dependent trend in auger recombination in direct-gap and indirect-gap semiconductor nanocrystals. *Physical Review Letters*, 102(17):1–4, 2009.

[217] Nikolay S. Makarov, et al. Spectral and Dynamical Properties of Single Excitons, Biexcitons, and Trions in Cesium-Lead-Halide Perovskite Quantum Dots. *Nano Letters*, 2016.

[218] Victor I. Klimov, A A Mikhailovsky, D W Mcbranch, C A Leatherdale, and Moungi G. Bawendi. Quantization of Multiparticle Auger Rates in Semiconductor Quantum Dots. *Science*, 287, 2000.

[219] Victor I. Klimov. Multicarrier Interactions in Semiconductor Nanocrystals in Relation to the Phenomena of Auger Recombination and Carrier Multiplication. *Annu. Rev. Condens. Matter Phys*, 5:285–316, 2014.

[220] Kaifeng Wu, Jaehoon Lim, and Victor I. Klimov. Superposition Principle in Auger Recombination of Charged and Neutral Multicarrier States in Semiconductor Quantum Dots. *ACS Nano*, 11(8):8437–8447, 2017.

[221] John A. Mcguire, Jin Joo, Jeffrey M. Pietryga, Richard D. Schaller, and Victor I. Klimov. New aspects of carrier multiplication in semiconductor nanocrystals. *Accounts of Chemical Research*, 41(12):1810–1819, 2008.

[222] Victor I. Klimov. Spectral and Dynamical Properties of Multiexcitons in Semiconductor Nanocrystals. *Annual Review of Physical Chemistry*, 58(1):635–673, 2007.

[223] John P. Philbin and Eran Rabani. Electron-hole correlations govern Auger recombination in nanostructures. *Nano Letters*, 2018.

[224] G. Lucovsky. On the Photoionization of Deep Impurity Centers In Semiconductors. *Solid State Communications*, 88(11):879–882, 1993.

[225] Lazaro A. Padilha, et al. Spectral dependence of nanocrystal photoionization probability: The role of hot-carrier transfer. *ACS Nano*, 5(6):5045–5055, 2011.

[226] John A. McGuire, et al. Spectroscopic signatures of photocharging due to hot-carrier transfer in solutions of semiconductor nanocrystals under low-intensity ultraviolet excitation. *ACS Nano*, 4(10):6087–6097, 2010.

[227] Menglu Chen and Philippe Guyot-Sionnest. Reversible Electrochemistry of Mercury Chalcogenide Colloidal Quantum Dot Films. *ACS Nano*, 11(4):4165–4173, 2017.

[228] Markus Braun, Stephan Link, Clemens Burda, and Mostafa A. El-Sayed. Transfer times of electrons and holes across the interface in CdS/HgS/CdS quantum dot quantum well nanoparticles. *Chemical Physics Letters*, 361(5-6):446–452, 2002.

[229] W.K. Wooters and W.H. Zurek. A single quantum cannot be cloned. *Nature*, 299(November):381–386, 1982.

[230] Charles H. Bennett and Gilles Brassard. Quantum cryptography: Public key distribution and coin tossing. *Proceedings of IEEE International Conference on Computers, Systems and Signal Processing*, 175:8, 1984.

[231] Alexander L. Efros and David J. Nesbitt. Origin and control of blinking in quantum dots. *Nature Nanotechnology*, 11(8):661–671, 2016.

[232] Gautham Nair, Jing Zhao, and Moungi G. Bawendi. Biexciton quantum yield of single semiconductor nanocrystals from photon statistics. *Nano Letters*, 11(3):1136–1140, 2011.

[233] Young-Shin Park, Wan Ki Bae, Lazaro A. Padilha, Jeffrey M. Pietryga, and Victor I. Klimov. Effect of the core/shell interface on auger recombination evaluated by single-quantum-dot spectroscopy. *Nano Letters*, 14(2):396–402, 2014.

[234] Hendrik Utzat, et al. Coherent single-photon emission from colloidal lead halide perovskite quantum dots. *Science*, 363(March):1068–1072, 2019.

[235] K. T. Shimizu, et al. Blinking statistics in single semiconductor nanocrystal quantum dots. *Physical Review B*, 63(20):1–5, 2001.

[236] Freddy T. Rabouw, Felipe V. Antolinez, Raphael Brechbühler, and David J. Norris. Microsecond Blinking Events in the Fluorescence of Colloidal Quantum Dots Revealed by Correlation Analysis on Preselected Photons. *The Journal of Physical Chemistry Letters*, 10(13):3732–3738, 2019.

[237] Javier Vela, et al. Effect of shell thickness and composition on blinking suppression and the blinking mechanism in 'giant' CdSe/CdS nanocrystal quantum dots. *Journal of Biophotonics*, 3(10-11):706–717, 2010.

[238] Ou Chen, et al. Compact high-quality CdSe-CdS core-shell nanocrystals with narrow emission linewidths and suppressed blinking. *Nature Materials*, 12(5):445–451, 2013.

[239] Daniel E. Gómez, Joel Van Embden, and Paul Mulvaney. Spectral diffusion of single semiconductor nanocrystals: The influence of the dielectric environment. *Applied Physics Letters*, 88(15):1–8, 2006.

[240] Young-Shin Park, Shaojun Guo, Nikolay S. Makarov, and Victor I. Klimov. Room Temperature Single-Photon Emission from Individual Perovskite Quantum Dots. *ACS Nano*, 9(10):10386–10393, 2015.

[241] Agata M. Brańczyk. Hong-Ou-Mandel Interference. *Arxiv*, 11(80):1–17, 2017.

[242] Charles Santori, David Fattal, Jelena Vučković, Glenn S. Solomon, and Yoshi-hisa Yamamoto. Indistinguishable photons from a single-photon device. *Nature*, 419(6907):594–597, 2002.

Appendix A

List of Acronyms

Care has been taken in this thesis to clearly define all acronyms but despite this confusion may occur, particularly for a reader unfamiliar with the materials or experiments in question. This appendix contains a table of all acronyms used in this thesis.

Table A.1: List of Acronyms

Acronym	Meaning
Al_2O_3	Aluminum Oxide OR Alumina
ALD	Atomic layer deposition
APD	Amplified photodetector OR Avalanche photodiode
BX	Biexciton
c-ALD	Colloidal atomic layer deposition
CdS	Cadmium Sulfide
CdSe	Cadmium Selenide
CW	Continuous wave
DEZ	Diethylzinc
DOS	Density of states
EDX	Energy-dispersive x-ray
EMA	Effective mass approximation
ES	Efros-Shklovskii
	Continued on next page

Table A.1 – continued from previous page

Acronym	Meaning
FLID	Fluorescence lifetime-intensity distribution
FTIR	Fourier transform infrared spectroscopy
FWHM	Full-width at half maximum
HBT	Hanbury-Brown and Twiss
HgS	Mercury Sulfide
IPL	Intense pulsed light
LSC	Luminescent solar concentrator
LSPR	Localized surface plasmon resonance
M	Mott
MEG	Multiple exciton generation
MIT	Metal-insulator transition
ML	Monolayer
NC	Nanocrystal
NIR	Near-infrared
nnh	Nearest neighbor hopping
PL	Photoluminescence
PPMS	Physical properties measurement system
QCP	Quantum critical point
QD	Quantum dot
QKD	Quantum key distribution
QY	Quantum yield
RF	Radiofrequency
Si	Silicon
SiH_4	Silane
SILAR	Successive ion layer adsorption and reaction.
SPE	Single photon emitter
SPS	Single photon counting
STEM	Scanning-tunneling electron microscopy
TA	Transient absorption

Table A.1 – continued from previous page

Acronym	Meaning
TEM	Transmission electron microscopy
TRPL	Time-resolved photoluminescence
VRH	Variable range hopping
w	Wurtzite
X	Exciton
$X^{+,-}$	Trion
XRD	X-ray diffraction
zb	Zinc-blende
ZnO	Zinc Oxide

Appendix B

Note of Unlimited Release

Chapters III-V of this thesis consist of research performed at Los Alamos National Laboratory, a Department of Energy National Laboratory managed by Triad National Security, LLC. The research contained in this thesis is approved for unlimited release with no restrictions by the Review and Approval System for Scientific and Technical Information under Los Alamos Unlimited Release number LA-UR-20-22985.